

STATISTICAL AND CONFORMATIONAL ANALYSIS OF STRUCTURAL TRANSITIONS IN  
FINITE SYSTEMS

by

KAI QI

(Under the Direction of Michael Bachmann)

ABSTRACT

The increased interest in understanding the thermodynamic activity in finite systems such as nanotechnological and biological systems has initiated numerous studies in interdisciplinary research. The properties and functions of these systems are inevitably connected to their geometric structures. However, due to finite-size and surface effects, conventional canonical statistical analysis fails to locate unique structural transition points for such systems. By considering integrated autocorrelation times of energetic and structural quantities, generalizing microcanonical inflection-point analysis, and introducing conformational analysis methods, we aim at developing more systematic and general approaches to the study of systems of finite size. To elucidate the power of these methods, we investigate coarse-grained lattice and off-lattice homopolymers by means of Monte Carlo importance sampling methods such as Metropolis, parallel tempering, and a parallel version of multicanonical sampling.

INDEX WORDS: Canonical Analysis, Autocorrelation Time, Microcanonical Inflection-Point Analysis, Monte Carlo Simulations, Metropolis, Parallel Tempering, Multicanonical Sampling, Flexible Polymer, Lattice Polymer, Structural Transitions, Finite Systems, Finite-Size Effects

STATISTICAL AND CONFORMATIONAL ANALYSIS OF STRUCTURAL TRANSITIONS IN  
FINITE SYSTEMS

by

KAI QI

B.A., Nanjing University, 2010

A Dissertation Submitted to the Graduate Faculty  
of The University of Georgia in Partial Fulfillment  
of the

Requirements for the Degree

DOCTOR OF PHILOSOPHY

ATHENS, GEORGIA

2016

©2016

Kai Qi

All Rights Reserved

STATISTICAL AND CONFORMATIONAL ANALYSIS OF STRUCTURAL TRANSITIONS IN  
FINITE SYSTEMS

by

KAI QI

Approved:

Major Professor: Michael Bachmann

Committee: David P. Landau  
Heinz-Bernd Schüttler  
Shan-Ho Tsai

Electronic Version Approved:

Suzanne Barbour  
Dean of the Graduate School  
The University of Georgia  
May 2016

# Acknowledgments

First of all, I would like to acknowledge Prof. Michael Bachmann for his selfless dedication and supervision of my work during the past four years. He is very knowledgeable on physics and quite approachable whenever you have questions. His strategy of supervising students, which I greatly benefited from, is to encourage one to have his own ideas and guide one to become an independent researcher gradually. I really appreciate his advice and help during my Ph.D. study and preparation of postdoc applications. Two other people I would like to thank are Prof. David P. Landau and Prof. M. Howard Lee, who both provided me with very helpful suggestions on planning my future career. I was so fortunate to take their graduate level classes on computer simulations and statistical physics from which I have learned the necessary background knowledge for my Ph.D. research. Thirdly, I would like to thank Dr. Jonathan Gross who was the “go-to-person” whenever I had scientific and technical problems during the first year of my Ph.D.. Moreover, I would like to thank Mike Caplinger and Jeff Deroshia for the management of my desktop and Shan-Ho Tsai for letting me use the powerful clusters in the Georgia Advanced Computing Resource Center. Last but not least, I am deeply grateful to my family for their support and encouragement during this difficult but joyful period of my life. In particular, I want to give my most sincere gratitude to my beloved ex-girlfriend, who accompanied me for about three years. I cherish the memories that we shared and plan to move on to continue enjoying the good of life. This thesis is for her. May she rest in peace.

# Contents

<b>1</b>	<b>Introduction</b>	<b>1</b>
<b>2</b>	<b>Statistical analysis methods</b>	<b>5</b>
2.1	Canonical analysis . . . . .	5
2.2	Autocorrelation time . . . . .	13
2.3	Microcanonical inflection-point analysis . . . . .	21
<b>3</b>	<b>Simulation and data smoothing methods</b>	<b>31</b>
3.1	Markov chains and the master equation . . . . .	31
3.2	Canonical Metropolis sampling . . . . .	33
3.3	Parallel tempering . . . . .	35
3.4	Multiple-histogram reweighting . . . . .	37
3.5	Multicanonical sampling . . . . .	38
3.6	Displacement update . . . . .	41
3.7	Chain-growth algorithm . . . . .	42
3.8	Multicanonical chain-growth algorithm . . . . .	45
3.9	Bézier smoothing . . . . .	48
<b>4</b>	<b>Flexible polymer</b>	<b>51</b>
4.1	Introduction . . . . .	51

4.2	Model and simulation method . . . . .	52
4.3	Results . . . . .	55
4.4	Conclusions . . . . .	66
<b>5</b>	<b>Lattice polymer adsorption</b>	<b>68</b>
5.1	Introduction . . . . .	68
5.2	Model and simulation method . . . . .	69
5.3	Results . . . . .	71
5.4	Conclusions . . . . .	80
<b>6</b>	<b>Flexible polymer with controlled bonds</b>	<b>81</b>
6.1	Introduction . . . . .	81
6.2	Model and simulation methods . . . . .	82
6.3	Results for a 15-mer . . . . .	86
6.4	Results for a 55-mer . . . . .	93
6.5	Conclusions . . . . .	104
<b>7</b>	<b>Summary and outlook</b>	<b>106</b>
	<b>Bibliography</b>	<b>111</b>

# List of Figures

2.1	Schematic temperature dependencies of entropy and heat capacity. (a, b) and (c, d) are the dependencies for the system undergoing first- and second-order phase transitions, respectively. . . . .	6
2.2	(a, b) Heat capacity $C_V$ and susceptibility $\chi$ indicate the same critical temperature $T \approx 2.269$ for the Ising model on the square lattice with infinite size. However, for the $10 \times 10$ square lattice, these two fluctuation quantities have peaks at different values of $T$ as shown in (c) and (d). . . . .	11
2.3	Heat capacity $C_V$ and thermal fluctuation of square of radius of gyration $d\langle R_{\text{gyr}}^2 \rangle/dT$ of a 30-mer flexible polymer. Collapse transition, which is a pseudophase transition, identified by utilizing the peak at $T = 1.4$ in $d\langle R_{\text{gyr}}^2 \rangle/dT$ only appears as a wide shoulder in $C_V$ . . . . .	11
2.4	Autocorrelation functions generated from the simulation of a flexible polymer model, which will be discussed in Chapter 4, with Metropolis sampling in (a) linear and (b) logarithmic scales. . . . .	15
2.5	Integrated autocorrelation times estimated by (a) the integration of autocorrelation functions and (b) binning analysis. . . . .	16
2.6	A typical time series of quantity $O$ which is divided into $K$ binning blocks. $\overline{O}_1^B, \overline{O}_2^B$ , and $\overline{O}_K^B$ represent the binning block averages of bin 1, 2, and $K$ , respectively. . . . .	17

2.7	(a) is a sketch of microcanonical entropy $S(E)$ in the condition of no pseudophase transition. Its first- to fourth-order derivatives over energy $E$ are shown in (b) to (e), respectively. For simplicity, X-axis (energy $E$ ) and Y-axis ( $S(E)$ or its derivatives) are not plotted in the graphs. Black solid lines represent zero lines of $S(E)$ or its derivatives. . . . .	21
2.8	(a) A first-order independent pseudophase transition can be identified from the backbending region of $\beta(E)$ and the positive peak in $\gamma(E)$ . (b, c, d) For independent pseudophase transitions of second, third, or fourth order, least sensitive inflection points in $\beta(E)$ , $\gamma(E)$ , and $\delta(E)$ together with the corresponding negative peaks or a positive valley in $\gamma(E)$ , $\delta(E)$ , and $\epsilon(E)$ are employed to locate pseudophase transition energies. For simplicity, X-axis (energy $E$ ) and Y-axis (derivatives of microcanonical entropy $S(E)$ ) are not plotted in the graphs. Black solid lines represent zero lines of the derivatives of $S(E)$ . . . . .	23
2.9	(a, b, c) Graphical proofs of dependent pseudophase transitions of second, third, and fourth orders. The transition energies can be identified by employing the least sensitive inflection points and their corresponding positive valleys or a negative peak. For simplicity, X-axis (energy $E$ ) and Y-axis (derivatives of microcanonical entropy $S(E)$ ) are not plotted in the graphs. Black solid lines represent zero lines of the derivatives of $S(E)$ . Same points in different curves in each subgraph are marked by the same signs. . . . .	27
2.10	Plots (a, b, c) demonstrate the functions of the most sensitive inflection points. For simplicity, X-axis (energy $E$ ) and Y-axis (derivatives of microcanonical entropy $S(E)$ ) are not plotted in the graphs. Black solid lines represent zero lines of the derivatives of $S(E)$ . Least and most sensitive inflection points are marked as purple solid disks and gray triangles, respectively. . . . .	29

3.1	Sketches of Monte Carlo updates (end and corner flips, crankshaft moves, and pivot rotations) used for updating polymers on a square lattice. . . . .	42
4.1	A sample conformation of the 30-mer flexible polymer. Bonded monomers are interacted through FENE potential $V_{\text{FENE}}$ [148–150]. For the non-bonded monomers, the truncated, shifted Lennard-Jones interaction $V_{\text{LJ}}^{\text{mod}}$ is introduced and utilized in this simulation. . . . .	53
4.2	FENE and truncated, shifted Lennard-Jones potentials. . . . .	54
4.3	Thermodynamic quantities for a flexible polymer with 30 monomers. (a) Mean energy $\langle E \rangle$ and number of contacts $\langle N_c \rangle$ ; (b) heat capacity $C_V$ and thermal fluctuation of the number of contacts $d\langle N_c \rangle/dT$ ; (c) square end-to-end distance $\langle R_{\text{ee}}^2 \rangle$ and square radius of gyration $\langle R_{\text{gyr}}^2 \rangle$ ; (d) thermal fluctuations of the square end-to-end distance $d\langle R_{\text{ee}}^2 \rangle/dT$ and the square radius of gyration $d\langle R_{\text{gyr}}^2 \rangle/dT$ . Error bars are smaller than the symbol size. . . . .	56
4.4	Sample conformations of the 30-mer flexible polymer for the “gas”, “liquid”, and “solid” pseudophases. . . . .	57
4.5	(a), (b), and (c) Autocorrelation functions of $E$ , $R_{\text{ee}}^2$ , $R_{\text{gyr}}^2$ , and $N_c$ at temperatures below, near, and above the collapse transition temperature, respectively, for $L = 30$ . For each quantity, the estimated integrated autocorrelation time converges to a constant as shown in (d), (e), and (f). The corresponding binning analysis results also show good convergence and are plotted in (g), (h), and (i). Dashed lines represent the fitted curves. Values of the fitted autocorrelation times the curves converge to are listed in Table 4.1. . . . .	58
4.6	Temperature dependence of integrated autocorrelation times (a) estimated with the binning method; (b) obtained by the integration of autocorrelation functions for the 30-mer. . . . .	61

4.7	(a), (b), and (c) are parts of the time series of $R_{\text{gyr}}^2$ , $E$ , and $N_c$ at $T = 5$ in equilibrium for the 30-mer. . . . .	61
4.8	Same as Fig. 4.6, but for the 55-mer. . . . .	63
4.9	(a) Integrated autocorrelation times of the energy $\tilde{\tau}_{E,\text{bin}}$ at different acceptance rates $P_{\text{accp}}$ for various temperatures near the collapse transition of the 30-mer; (b) modified autocorrelation times of energy versus acceptance rates; (c) acceptance rates at fixed maximum displacement $d = 0.3r_0$ for different temperatures; (d) integrated autocorrelation times at fixed acceptance rate $P_{\text{accp}}^a = 0.2$ as a function of temperature for the 30-mer. . . . .	64
5.1	A sample conformation of the grafted simple-cubic (sc) lattice homopolymer of length 503 (left). A sketch of this model illustrating the number of nearest-neighbor, but nonadjacent monomer-monomer contacts $n_m$ and number of nearest-neighbor monomer-substrate contacts $n_s$ (right). . . . .	70
5.2	Examples of the application of the microcanonical inflection-point analysis method to a grafted lattice polymer model. (a) First- and second-order pseudophase transitions occur at $E \approx -830$ and $-767$ for $s = 0.83$ . (b) A third-order pseudophase transition can be identified at $E \approx -613$ for $s = 0.50$ . Signals in (c) indicate the existence of a fourth-order pseudophase transition appearing at $E \approx -590$ for $s = 1.30$ . . . . .	72
5.3	Microcanonical pseudophase diagram for the homogeneous lattice polymer grafted to an adhesive surface. . . . .	73
5.4	Examples of typical conformations in the different structural pseudophases for homogeneous lattice polymer grafted to an adhesive surface. (see Fig. 5.3) . . . . .	75

5.5	(a), (b), and (c) are microcanonical pseudophase diagrams for bin size $dE = 0.80, 5.00,$ and $11.0,$ respectively. Note that some of the differences between these pseudophase diagrams and Fig. 5.3 are due to the different plotting scheme. . . . .	78
5.6	Microcanonical pseudophase diagram with the information of the origins of different pseudophase transition lines. . . . .	79
6.1	A sample conformation of the 55-mer flexible polymer model with modified bonded potential. . . . .	83
6.2	Potentials between bonded monomers, modeled by a FENE potential and Lennard-Jones interaction for different values of the parameter $\eta \in [0, 1]$ that controls the width and asymmetry of the bonded potential. . . . .	84
6.3	(a) Heat capacity $C_V,$ (b) microcanonical inverse temperature $\beta(E),$ and (c,d) its first and second derivatives $\gamma(E)$ and $\delta(E),$ respectively. . . . .	87
6.4	(a) Microcanonical pseudophase diagram parameterized by energy and the potential width and asymmetry parameter $\eta.$ Here, G, L, and S stand for “gas”, “liquid”, and “solid” structural phases, respectively. The $S_{ic-core}$ pseudophase consists mostly of incomplete icosahedral structures. $S_{ic}$ and $S_{bi}$ incorporate compact icosahedral and bihexagonal structures, respectively. (b) Enlarged section detailing the low energy region for $\eta < 0.15.$ The solid-solid pseudophase transition line is extended by a dashed empirical line constructed based on the data provided by structural analysis. . . . .	89

6.5	(a,b,c,d) Intensity plots of the $Q_6$ order parameter for a 15-mer with $\eta = 0.00, 0.05, 0.10, 1.0$ . The shading indicates the probability of detecting a configuration with a given value of the order parameter, red being the maximum probability and black being the lowest. The freezing and the solid-solid pseudophase transitions are indicated by solid and dashed horizontal lines respectively. For $\eta \leq 0.1$ , the polymer has two distinct solid pseudophases. In addition to the icosahedral pseudophase ( $Q_6 \approx 0.65$ ) the polymer is found in the bihexagonal pseudophase at low energies ( $Q_6 \approx 0.41$ ). . . . .	92
6.6	Two distinct low-energy structures of the elastic 15-mer. (a) Compact structure with a stable icosahedral core and two monomers displaced onto the incomplete second layer. (b) The bihexagon is the preferred ground-state geometry for $\eta \leq 0.1$ . . . . .	93
6.7	(a) Heat capacity $C_V$ ; (b) and (c) thermal fluctuation of the squared radius of gyration $d\langle R_{\text{gyr}}^2 \rangle/dT$ of a flexible polymer $L = 55$ for different values of $\eta$ . Note the different scales in (c). . . . .	94
6.8	(a) Microcanonical entropy $S(E)$ for an array of $\eta$ values; (b) microcanonical inverse temperature $\beta(E)$ ; (c) $\gamma(E)$ ; (d) $\delta(E)$ . . . . .	96

6.9	(a) Microcanonical pseudophase diagram. Here, $G$ , $L$ , and $S$ represent “gas”, “liquid”, and “solid” pseudophase, respectively. (b) Low-temperature and small- $\eta$ value region, emphasizing the different solid pseudophases. In $S_{\text{bi-core}}$ structures with bihexagonal cores and liquid-like shells are dominant. $S_{\text{ic-core}}$ represents structures with well-formed icosahedral cores but incomplete surface layer. In the $S_{\text{ic}}$ and $S_{\text{bi}}$ pseudophases, icosahedral and bihexagonal core structures with complete shells dominate. In $S_{\text{mix}}$ icosahedral and bihexagonal core structures coexist. The “solid” subphases are separated by gray empirical transition bands. Dashed lines represent lines of pseudophase transitions higher than second order. . . . .	97
6.10	Polymer core structures: (left) icosahedral (ic-core); (right) bihexagonal (bi-core); both found in a 55-mer at low energies in the range $0 < \eta < 0.025$ of the bond potential parameter that controls width and asymmetry. . . . .	99
6.11	(a, b, c, d) Intensity plots of the $Q_6$ order parameter corresponding to $\eta = 0.005, 0.010, 0.020, 0.050$ , respectively. The probability of finding polymer structures with a particular value of $Q_6$ is represented by shading, with black being zero probability and red corresponding to the maximum probability of 1.100	100
6.12	Typical structures of “solid” subphases. The figures in the same row are different representatives of the same conformation. Icosahedral and bihexagonal cores are plotted in blue and red respectively. Gray beads represent surface monomers. The structures in the third column shows the explicit cores. The surface monomers are represented by a wireframe. . . . .	101
6.13	The bond-length variance $\sigma_{BL}^2$ of the 55-mer as a function of energy for different values of the model parameter $\eta$ . . . . .	102

# List of Tables

4.1	Autocorrelation times of $E$ , $R_{\text{ee}}^2$ , $R_{\text{gyr}}^2$ , and $N_c$ estimated by integration of autocorrelation functions and by using the binning method at three temperatures below, near, and above the collapse transition. . . . .	58
-----	---	----

# Chapter 1

## Introduction

Cooperativity referring to the collective changes of a given system leads to the transformations among the macrostates that describe the macroscopic properties and states of the system and are specified by sets of external parameters such as temperature and pressure. Macrostates sharing similar thermodynamic properties are classified as being in the same phase. The corresponding transition is referred to as phase transition, which is one of the most fascinating phenomena in nature and has initiated many research for several decades directed toward studying the physical mechanisms guiding the cooperative changes of the system. In fact, phase transitions such as melting of ice, ferromagnetic, and superfluid transitions occur in the thermodynamic limit, i.e., for infinitely large systems. However, the rapid growth of interest in nanotechnological and biological systems makes it necessary to investigate the cooperative behaviors in finite-size systems. Among them, proteins, which are prominent representatives of finite polymers, are of most concern due to their irreplaceable role in maintaining the functionality of our bodies such as controlling transport processes and enzymatic catalyzation of chemical reactions. The biological functions and processes of proteins are inevitably connected to their geometric structures, i.e., the functional structures, which are the specific three dimensional conformations of certain proteins and determine

the functions of these proteins such as forming the ion channels and stabilizing the cell backbones, are usually in folded states. The structural transitions between the folded and unfolded states present strong similarities as the phase transitions, which makes it possible to extend the terminology defined in the thermodynamic limit to such finite systems. The structural transitions are usually denoted as pseudophase transitions and the corresponding phases are called pseudophases. But to what extent the analysis methods for the infinitely large systems are still valid in studying systems with finite size needs to be verified.

The statistical analysis of the structural behavior under thermal conditions is the only possibility to identify macrostates that are stable in parameter space and form conformational phases in a distinct region of that space. Canonical statistical analysis based on discontinuities in thermodynamic quantities such as entropy, the specific heat, or order-parameter fluctuations has long been employed with much success to identify and classify thermodynamic phase transitions. However, discontinuities or divergences are not present if the system is finite, in which case ambiguities in locating transition points also occur. Because of their chemical composition and biological function, proteins are the most prominent examples of macromolecules that cannot be “scaled up”. However, in most of the applications, polymers are finite and in many cases sufficiently small as to render finite-size and surface effects essential for its overall thermodynamic behavior. When canonical analysis is applied to such systems, the detailed information about the structural transitions reflecting the finite-size effects is lost. One possible scheme that can identify the structural transitions and regain the information about finite-size effects is by studying the partition function zeros [1–6]. But due to its intricacy, this method is difficult to implement. Therefore, the unique identification of conditions for enhanced thermal activity is a challenge to modern statistical physics for systems of mesoscopic scales.

Thanks to the fast development in computer technology, vast computational resources are available nowadays and thus enables the accurate study of fundamental statistical quan-

tities by using computer simulations. One such quantity is density of states, which opens a completely new way for the study of structural transitions by utilizing the currently most promising approach, microcanonical analysis [7,8]. Initially, first-order-like transitions, which are structural transitions in finite systems possessing the features of first-order phase transitions in thermodynamic limit, were analyzed by means of Maxwell’s construction [7–17]. In this construction, the backbending region in the transition regime of the energetic temperature curve is replaced by an entirely flat segment. However, the Maxwell construction only applies to single structural transitions of first order and is less feasible for the analysis of first-order-like transitions accompanied by subphase transitions, which are subtle structural transition signals usually embedded in the backbending regions of the first-order-like transitions. Furthermore, higher order structural transitions that do not exhibit the backbending feature cannot be analyzed by Maxwell construction. By extending the “flatness” idea of Maxwell construction to a more general principle, the principle of minimal sensitivity [18,19], the systematic extension of the microcanonical statistical analysis by classifying inflection points in the microcanonical temperature [20] has turned out to be a promising approach towards a unique investigation of structural transitions in mesoscopic systems. However, the initial theorem only provides ways to identify first- and second-order pseudophase transitions, which may constrain the application of this approach to systems with finite size where higher-order pseudophase transitions are dominant due to finite-size effects.

In this thesis, we are aiming to introduce several novel statistical and conformational analysis approaches that can be applied to study the structural transitions of finite-size systems. The structure of the thesis is as follows. In Chapter 2, statistical analysis methods including the conventional canonical analysis and the novel approaches, i.e., autocorrelation times [21, 22] and generalized microcanonical inflection-point analysis [23], are discussed. The Monte Carlo and data smoothing methods are explained in Chapter 3. To test the availability of the autocorrelation time approach in identifying structural transitions, we

apply this method to study a simple coarse-grained flexible polymer model in Chapter 4. The generalized microcanonical inflection-point analysis is further applied to investigate the lattice polymer adsorption [24] in Chapter 5 and a flexible polymer with controlled bonds [25,26] in Chapter 6. Several suitable order parameters new to the polymer study are introduced in Chapter 6 as well. My thesis is summarized in Chapter 7.

# Chapter 2

## Statistical analysis methods

### 2.1 Canonical analysis

For a given system under certain external conditions, the set of dominating microstates constitute the macrostate of the system. This macrostate generally describes the major properties shared by all the corresponding microstates. If these macrostates exhibit significant similarities when the external parameter varies over a certain range, they are assigned to the same phase. However, if a small variation of the parameter substantially changes the properties of the macrostates, a phase transition may occur.

The conventional method of identifying and distinguishing phase transitions is based on Ehrenfest's classification. This approach classifies the phase transitions by locating discontinuities or divergences in the derivatives of thermodynamic potentials. For example, for a system in the canonical ensemble in which temperature, volume, and number of particles are fixed, the natural thermodynamic potential is the Helmholtz free energy  $F(T, V, N)$ .

If a discontinuity is observed in the first derivative of free energy, i.e., the entropy

$$\left(\frac{\partial F}{\partial T}\right)_{N,V} = -S(T, V, N), \quad (2.1)$$

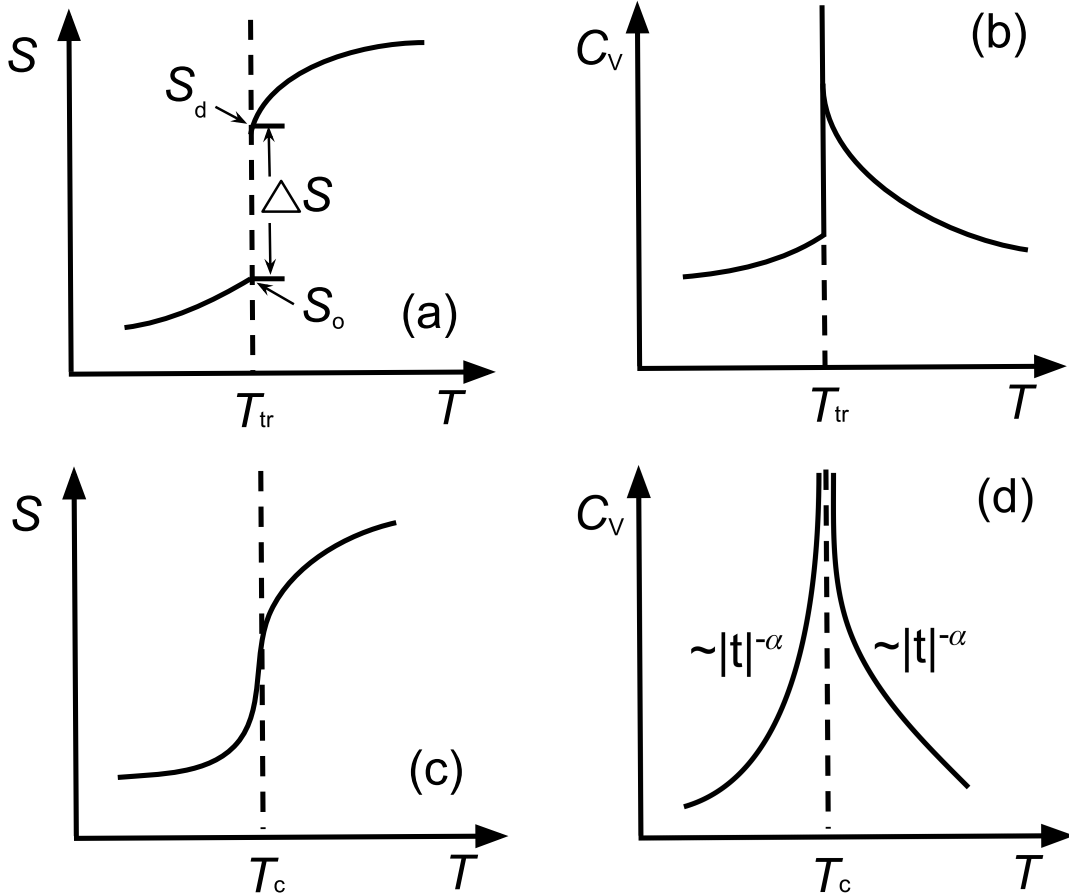


Figure 2.1: Schematic temperature dependencies of entropy and heat capacity. (a, b) and (c, d) are the dependencies for the system undergoing first- and second-order phase transitions, respectively.

the corresponding transition is considered to be of first order. A sketch of the entropy for a system undergoing a first-order phase transition is plotted in Fig. 2.1(a). The characteristic of a first-order phase transition is the coexistence of the ordered and disordered phases  $S_o$  and  $S_d$  which are separated by the latent heat

$$\Delta Q_{\text{lat}} = T_{\text{tr}} \Delta S = T_{\text{tr}} (S_d - S_o) \quad (2.2)$$

at the transition temperature. Because of the discontinuity in the entropy, the corresponding heat capacities,

$$\left(\frac{\partial^2 F}{\partial T^2}\right)_{N,V} = -\left(\frac{\partial S}{\partial T}\right)_{N,V} = -\frac{1}{T}C_V(T), \quad (2.3)$$

on two sides of  $T_{\text{tr}}$  vary accordingly. Fig. 2.1(b) shows one kind of scenario. From the thermodynamic point of view, the heat capacity quantifies the capacity of heat storage by the system. In the canonical ensemble, the heat capacity defined in Eq. 2.3 represents the amount of heat exchange  $TdS$  while temperature varies. Equivalently, in statistical physics, the heat capacity, which corresponds to the fluctuations of energy, is given by

$$\begin{aligned} C_V(T) &= \frac{d\langle E \rangle}{dT} \\ &= \frac{d}{dT} \int \mathcal{D}X E(\mathbf{X}) p_{\text{can}}(\mathbf{X}, T) \\ &= \frac{d}{dT} \left( \frac{\int \mathcal{D}X E(\mathbf{X}) e^{-E(\mathbf{X})/k_B T}}{\int \mathcal{D}X e^{-E(\mathbf{X})/k_B T}} \right) \\ &= \frac{1}{k_B T^2} \left[ \frac{\int \mathcal{D}X E^2(\mathbf{X}) e^{-E(\mathbf{X})/k_B T}}{\int \mathcal{D}X e^{-E(\mathbf{X})/k_B T}} - \left( \frac{\int \mathcal{D}X E(\mathbf{X}) e^{-E(\mathbf{X})/k_B T}}{\int \mathcal{D}X e^{-E(\mathbf{X})/k_B T}} \right)^2 \right] \\ &= \frac{1}{k_B T^2} (\langle E^2 \rangle - \langle E \rangle^2) \end{aligned} \quad (2.4)$$

where  $k_B$  is the Boltzmann constant,  $E$  is the energy of the system,  $p_{\text{can}}(\mathbf{X}, T)$  represents the probability of a conformation with  $N$  particles  $\mathbf{X} = (\mathbf{x}_1, \mathbf{x}_2, \dots, \mathbf{x}_N)$  in the canonical ensemble at temperature  $T$ , and  $\mathcal{D}X$  is the integral measure for the infinitesimal scan of the  $3N$ -dimensional conformation space and defined via [7]

$$\int \mathcal{D}X = \frac{1}{N!(\sqrt{2\pi\hbar})^{3N}} \prod_{i=1}^N \int d^3x_i. \quad (2.5)$$

If the entropy is continuous, as plotted in Fig. 2.1(c), but a divergence occurs in the heat capacity as shown in Fig. 2.1(d), the relevant phase transition is of second order and the transition temperature can be identified from the position where  $C_V$  diverges. The latent

heat  $\Delta Q_{\text{lat}} = 0$  for the second-order phase transition implies that there is no coexistence of two phases and the transition is continuous. Second-order phase transitions and the corresponding transition temperatures are also named as critical transitions and temperatures  $T_c$ . Defining the dimensionless parameter  $t = (T_c - T)/T_c$ , the divergence near the critical temperature of the heat capacity curve follows the power law  $C_V \sim |t|^{-\alpha}$ , described in Fig. 2.1(d) [7,27]. Here,  $\alpha$  is the critical exponent associated with the heat capacity. Besides  $C_V$ , order parameters  $O$  with the property that  $O = 0$  for  $T \geq T_c$  and  $\neq 0$  for  $T < T_c$  can also be utilized to locate critical temperatures. Power law behavior,  $O \sim t^\beta$  for  $T < T_c$  ( $t > 0$ ), with the corresponding critical exponent  $\beta$  can also be observed near the critical temperature when the external field is zero. The representative order parameters are the mean value of the spontaneous magnetization  $\langle M \rangle$  in a magnetic system and the density difference  $|\rho - \rho_c|$  in a gas-liquid system [7,27]. How the order parameters respond to the change of external fields (magnetic field  $H$  for magnetic system and pressure  $P$  for gas-liquid system) is described by the corresponding response quantities (susceptibility  $\chi = (\partial \langle M \rangle / \partial H)_T$  and isothermal compressibility  $\kappa_T = \rho^{-1}(\partial \rho / \partial P)_T$ , respectively), which are related to the fluctuations of the order parameters. The relationship between the response quantities and the fluctuations of order parameters can be illustrated in the two dimensional square-lattice Ising model, which is the simplest mathematical model of ferromagnetic systems. In this model, the magnetic dipole moments of atomic spins in the ferromagnetic systems are represented by the two state spins  $\sigma = \pm 1$ . The energy of the system with  $N_s$  spins is given by

$$\begin{aligned}
 E &= -J \sum_{\langle ij \rangle}^{N_s} \sigma_i \sigma_j - H \sum_{i=1}^{N_s} \sigma_i \\
 &= -J \sum_{\langle ij \rangle}^{N_s} \sigma_i \sigma_j - HM,
 \end{aligned} \tag{2.6}$$

where  $J > 0$  is an interaction energy,  $\langle ij \rangle$  indicates that the summation is over nearest

neighbors, and the spontaneous magnetization  $M = \sum_{i=1}^{N_s} \sigma_i$  has been used in the calculation. The susceptibility can thus be derived as

$$\begin{aligned}
\chi &= \left( \frac{d\langle M \rangle}{dH} \right)_T \\
&= \frac{d}{dH} \sum_{\mu} M(\mu) p_{\text{can}}(\mu, T) \\
&= \frac{d}{dH} \left( \frac{\sum_{\mu} M(\mu) e^{-E(\mu)/k_B T}}{\sum_{\mu} e^{-E(\mu)/k_B T}} \right) \\
&= \frac{1}{k_B T} \left[ \frac{\sum_{\mu} M^2(\mu) e^{-E(\mu)/k_B T}}{\sum_{\mu} e^{-E(\mu)/k_B T}} - \left( \frac{\sum_{\mu} M(\mu) e^{-E(\mu)/k_B T}}{\sum_{\mu} e^{-E(\mu)/k_B T}} \right)^2 \right] \\
&= \frac{1}{k_B T} (\langle M^2 \rangle - \langle M \rangle^2), \tag{2.7}
\end{aligned}$$

where  $\mu$  represent configurations of the Ising model on the square lattice. The response quantities (fluctuations of order parameters) also exhibit power law behavior,  $\chi/\kappa_T \sim |t|^{-\gamma}$ , with  $\gamma$  being the associated critical exponent near the critical temperature when the external field is zero [7, 27]. The fluctuation Eq. 2.4 can be generalized and the thermal fluctuations of standard order parameters such as mean values of radius of gyration  $R_{\text{gyr}}$  and end-to-end distance  $R_{\text{ee}}$ , which are utilized to describe the compactness of polymer structures, can be defined as

$$\begin{aligned}
\frac{d\langle O \rangle}{dT} &= \frac{d}{dT} \int \mathcal{D}X O(\mathbf{X}) p_{\text{can}}(\mathbf{X}, T) \\
&= \frac{d}{dT} \left( \frac{\int \mathcal{D}X O(\mathbf{X}) e^{-E(\mathbf{X})/k_B T}}{\int \mathcal{D}X e^{-E(\mathbf{X})/k_B T}} \right) \\
&= \frac{1}{k_B T^2} \left( \frac{\int \mathcal{D}X O(\mathbf{X}) E(\mathbf{X}) e^{-E(\mathbf{X})/k_B T}}{\int \mathcal{D}X e^{-E(\mathbf{X})/k_B T}} - \frac{\int \mathcal{D}X O(\mathbf{X}) e^{-E(\mathbf{X})/k_B T}}{\int \mathcal{D}X e^{-E(\mathbf{X})/k_B T}} \right. \\
&\quad \left. \times \frac{\int \mathcal{D}X E(\mathbf{X}) e^{-E(\mathbf{X})/k_B T}}{\int \mathcal{D}X e^{-E(\mathbf{X})/k_B T}} \right) \\
&= \frac{1}{k_B T^2} (\langle OE \rangle - \langle O \rangle \langle E \rangle), \tag{2.8}
\end{aligned}$$

These are the response quantities with respect to the temperature as an external field and usually exhibit extremal values at transition temperatures. By considering the divergences and extremal values of the fluctuation quantities, phase transition temperatures can be located in the thermodynamic limit. Another quantity which also diverges near the critical temperature is the correlation length  $\xi$  which has the power law behavior,  $\xi \sim |t|^{-\nu}$ , with the critical exponent  $\nu$  [7, 28, 29].

The power law behavior and critical exponent reveal one of the most special and striking properties of second order phase transitions: universality. Critical exponents of a system are usually independent of the parameters contained in the system, such as the interaction strength  $J$  and the lattice type in the Ising model. Instead, they are affected by the systems' gross properties, such as the dimensionality of the lattice  $d$  and the number of the dimensions of the order parameters. This yields the appearance of the universality class in which different systems share the same critical exponents. By utilizing this universal property, the investigation of the critical behavior of a complex system could be simplified to the study of a relatively simple system which falls into the same universality class [30].

However, these fundamental concepts only apply to the systems in the thermodynamic limit, i.e., system sizes are infinite. When applied to finite-size systems, these properties can no longer be retained. First of all, the power law relations will become invalid in finite-size systems. Fig. 2.2 shows the heat capacity and susceptibility of Ising models on the square lattice with infinite and finite lattice sizes. Note that the susceptibility for the infinite lattice refers to Eq. 2.7 and  $\chi \propto [\langle M^2 \rangle - \langle |M| \rangle^2]$  has been employed for the  $10 \times 10$  lattice in order to keep  $\langle |M| \rangle \neq 0$  at  $T < T_{\text{tr}}$  in the simulation. The divergences of the fluctuation quantities near the critical temperature in the thermodynamic limit become rounded peaks on the  $10 \times 10$  square lattice. This phenomenon indicates that the power law behavior cannot be used to asymptotically describe the critical behavior of the fluctuation quantities in finite-size systems. In addition, finite-size effects can also cause ambiguities in the estimation of

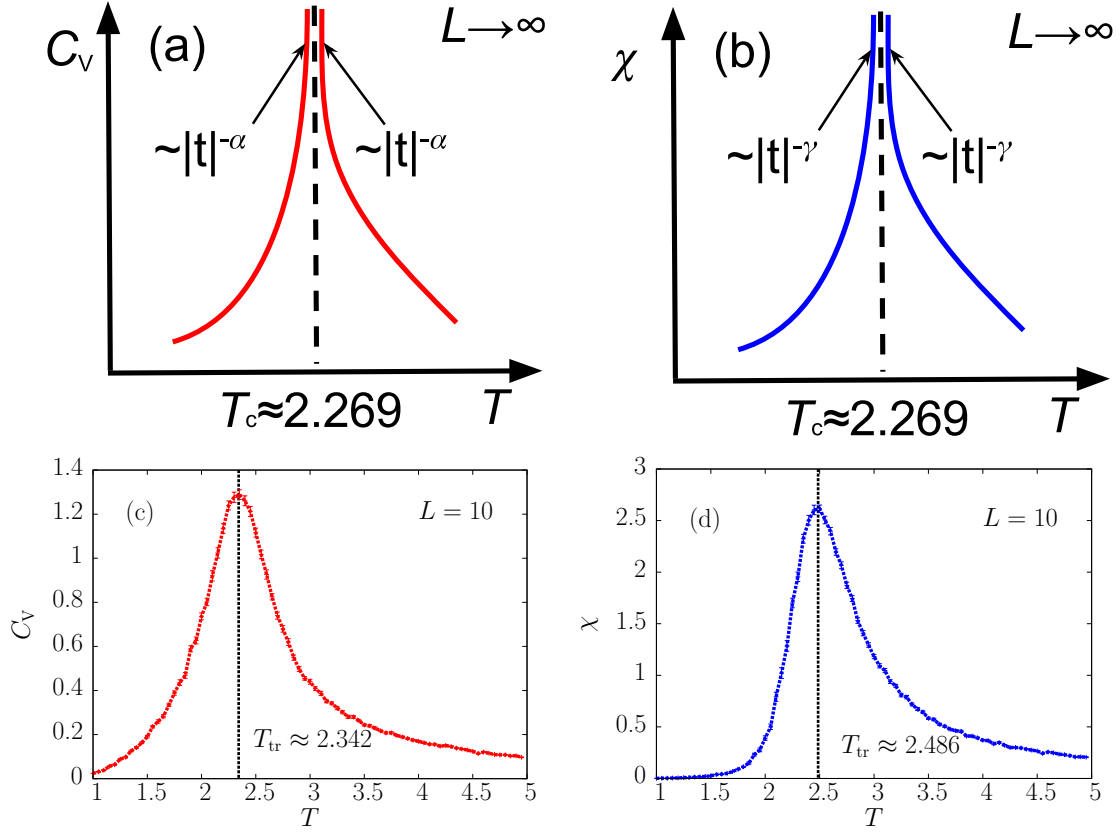


Figure 2.2: (a, b) Heat capacity  $C_V$  and susceptibility  $\chi$  indicate the same critical temperature  $T \approx 2.269$  for the Ising model on the square lattice with infinite size. However, for the  $10 \times 10$  square lattice, these two fluctuation quantities have peaks at different values of  $T$  as shown in (c) and (d).

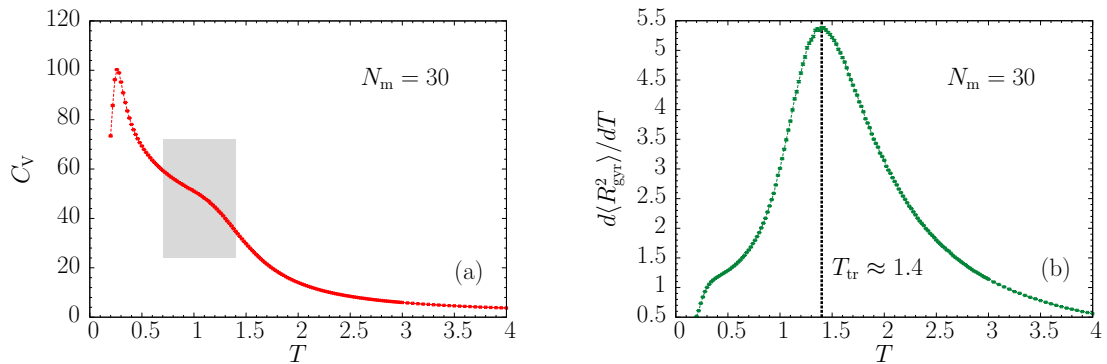


Figure 2.3: Heat capacity  $C_V$  and thermal fluctuation of square of radius of gyration  $d\langle R_{\text{gyr}}^2 \rangle/dT$  of a 30-mer flexible polymer. Collapse transition, which is a pseudophase transition, identified by utilizing the peak at  $T = 1.4$  in  $d\langle R_{\text{gyr}}^2 \rangle/dT$  only appears as a wide shoulder in  $C_V$ .

transition temperatures. For example, in the Ising model with infinite system size, critical transition temperatures estimated by heat capacity and susceptibility will lead to the same value  $T \approx 2.269$ . But simulation results of a  $10 \times 10$  square lattice exhibit two different values of pseudophase transition temperatures, i.e.,  $T \approx 2.342$  in  $C_V$  and 2.486 in  $\chi$ . Thus, the estimated “transition” temperature is claimed as lying in the interval  $[2.342, 2.486]$  denoted as the transition band. Therefore, when applying canonical analysis to study finite-size systems, instead of getting unique pseudophase transition temperatures, one can only obtain transition bands constructed by utilizing the temperatures estimated from various fluctuation quantities. Furthermore, it is difficult to judge the orders of the “transitions” from the measured quantities in the finite systems. Because the internal energies are continuous and the fluctuation quantities exhibit rounded peaks at the pseudophase transition temperatures in both first- and second-order “transitions”. Last but not least, when applied to study finite-size systems, canonical quantities may not be able to display pronounced signals which are crucial in identifying and locating pseudophase transitions. Fig. 2.3 shows the simulation results of heat capacity  $C_V$  and square of radius of gyration  $d\langle R_{\text{gyr}}^2 \rangle/dT$  curves of a 30-mer flexible polymer, which is a coarse-grained model for polymers such as proteins and will be discussed in Chapter 4. In  $d\langle R_{\text{gyr}}^2 \rangle/dT$ , a pronounced peak indicating the collapse transition can be identified at  $T \approx 1.4$ . But  $C_V$  only presents a wide shoulder at the same temperature, which makes locating the transition temperature difficult. Therefore, canonical analysis is not always the optimal option in the study of finite-size systems. Note that the properties of the systems in the thermodynamic limit, such as critical exponents and transition temperatures, can be obtained from the data of finite systems by utilizing finite-size scaling. However, the rapid growth of interest in understanding the thermodynamic activity in finite systems such as biological systems manifests the necessity of finding other alternative or more systematic and robust analysis methods. One of the alternative approaches to locate “transition” temperatures is to employ autocorrelation times.

## 2.2 Autocorrelation time

Suppose a time series with a large number of data from an importance sampling Monte Carlo simulation such as the simulation with Metropolis algorithm and single monomer displacement update (I will discuss the algorithm and update in Chap. 3) has been generated, the expectation value of any quantity  $O$ , i.e.,  $\langle O \rangle$ , can be estimated by calculating the arithmetic mean over the Markov chain,

$$\bar{O} = \frac{1}{N} \sum_{j=1}^N O_j, \quad (2.9)$$

where  $O_j$  is the value of  $O$  in the  $j$ th measurement and  $N$  is the number of total measurements. Here,  $\bar{O}$  is a random variable which fluctuates around its expectation value  $\langle \bar{O} \rangle$  when the system is in equilibrium. Since each measurement  $O_j$  in the time series is also a random variable with the same expectation value  $\langle O_j \rangle = \langle O \rangle$ , it can be deduced that the expectation value of  $\bar{O}$  is the same as the expectation value of the individual measurement

$$\langle \bar{O} \rangle = \left\langle \frac{1}{N} \sum_{j=1}^N O_j \right\rangle = \frac{1}{N} \sum_{j=1}^N \langle O_j \rangle = \frac{1}{N} \sum_{j=1}^N \langle O \rangle = \langle O \rangle. \quad (2.10)$$

In Metropolis simulations, the individual measurements will not be independent. Thus, by introducing the normalized autocorrelation function ( $A(0) = 1$ ),

$$A(k) = \frac{\langle O_l O_{l+k} \rangle - \langle O_l \rangle^2}{\sigma_O^2}, \quad (2.11)$$

where  $l$  can be any integer in the range  $[1, N - k]$  and  $\sigma_O^2 = \langle O_l^2 \rangle - \langle O_l \rangle^2 = \langle O^2 \rangle - \langle O \rangle^2$ , the corresponding variance of  $\bar{O}$  is calculated as [31, 32]

$$\sigma_{\bar{O}}^2 = \langle \bar{O}^2 \rangle - \langle \bar{O} \rangle^2$$

$$\begin{aligned}
&= \frac{1}{N^2} \sum_{i,j=1}^N \langle O_i O_j \rangle - \frac{1}{N^2} \sum_{i,j=1}^N \langle O_i \rangle \langle O_j \rangle \\
&= \frac{1}{N^2} \sum_{i=1}^N (\langle O_i^2 \rangle - \langle O_i \rangle^2) + \frac{1}{N^2} \sum_{i \neq j}^N (\langle O_i O_j \rangle - \langle O_i \rangle \langle O_j \rangle) \\
&= \frac{1}{N} \left[ \sigma_O^2 + \frac{2}{N} \sum_{i=1}^N \sum_{j=i+1}^N (\langle O_i O_j \rangle - \langle O_i \rangle \langle O_j \rangle) \right] \\
&= \frac{1}{N} \left[ \sigma_O^2 + \frac{2}{N} \sum_{k=1}^N (\langle O_l O_{l+k} \rangle - \langle O_l \rangle \langle O_{l+k} \rangle) (N - k) \right] \\
&= \frac{1}{N} \left[ \sigma_O^2 + 2 \sum_{k=1}^N (\langle O_l O_{l+k} \rangle - \langle O_l \rangle \langle O_{l+k} \rangle) \left(1 - \frac{k}{N}\right) \right] \\
&= \frac{2\sigma_O^2}{N} \left[ \frac{1}{2} + \sum_{k=1}^N \left( \frac{\langle O_l O_{l+k} \rangle - \langle O_l \rangle \langle O_{l+k} \rangle}{\langle O_l^2 \rangle - \langle O_l \rangle^2} \right) \left(1 - \frac{k}{N}\right) \right] \\
&= \frac{2\sigma_O^2}{N} \left[ \frac{1}{2} + \sum_{k=1}^N A(k) \left(1 - \frac{k}{N}\right) \right], \tag{2.12}
\end{aligned}$$

where time translation invariance has been used. Fig. 2.4(a) shows an example of an autocorrelation function which decays from 1 to 0 as time displacement increases. For large time separation  $k$ , the autocorrelation function decays exponentially (Fig. 2.4(b)),

$$A(k) \longrightarrow e^{-k/\tau_{O,\text{exp}}}, \tag{2.13}$$

where  $\tau_{O,\text{exp}}$  is the exponential autocorrelation time of  $O$ . Because of large statistical fluctuations in the tail of  $A(k)$ , the accurate estimation of  $\tau_{O,\text{exp}}$  is often difficult. By introducing the integrated autocorrelation time,

$$\tau'_{O,\text{int}} = \frac{1}{2} + \sum_{k=1}^N A(k) \left(1 - \frac{k}{N}\right), \tag{2.14}$$

Eq. 2.12 becomes

$$\epsilon_O^2 \equiv \sigma_O^2 = \frac{2\sigma_O^2}{N} \tau'_{O,\text{int}} = \frac{\sigma_O^2}{N_{\text{eff}}} \tag{2.15}$$

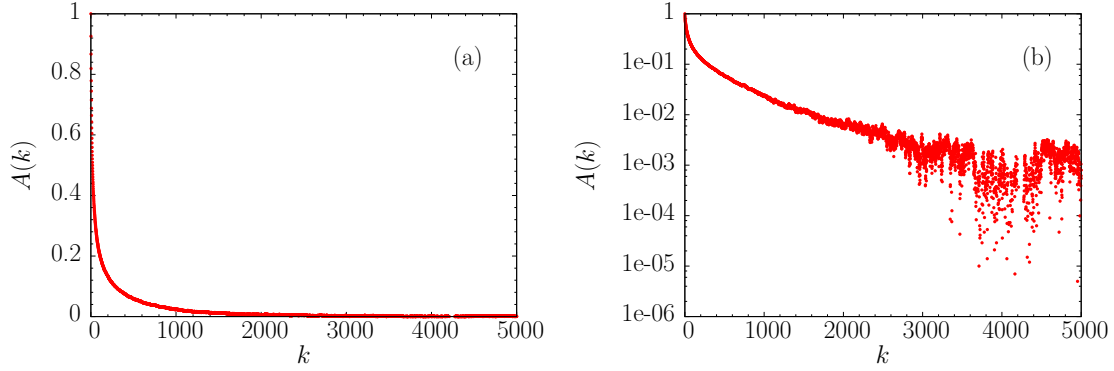


Figure 2.4: Autocorrelation functions generated from the simulation of a flexible polymer model, which will be discussed in Chapter 4, with Metropolis sampling in (a) linear and (b) logarithmic scales.

with the effective statistics  $N_{\text{eff}} = N/2\tau'_{O,\text{int}}$ . According to Eq. 2.13, in any meaningful simulation with  $N \gg \tau_{O,\text{exp}}$ , we can safely neglect the correction term in the parentheses in Eq. 2.14. This leads to the frequently employed definition of the integrated autocorrelation time,

$$\tau_{O,\text{int}} = \frac{1}{2} + \sum_{k=1}^N A(k). \quad (2.16)$$

The estimation of the integrated autocorrelation time requires the replacement of the expectation value in  $A(k)$  by mean values, e.g.,  $\langle O_l O_{l+k} \rangle$  and  $\langle O_l \rangle$  by  $\overline{O_l O_{l+k}}$  and  $\overline{O_l}$ . Therefore, it is useful to introduce the following estimator

$$\tilde{\tau}_{O,\text{int}}(k_{\text{max}}) = \frac{1}{2} + \sum_{k=1}^{k_{\text{max}}} \tilde{A}(k) \quad (2.17)$$

where  $\tilde{A}(k)$  is the estimator of  $A(k)$ . Since  $\tilde{A}(k)$  usually decays to zero as  $k$  increases,  $\tilde{\tau}_{O,\text{int}}$  will finally converge to a constant. Because of the statistical noise of  $\tilde{A}(k)$  for large  $k$ ,  $\tilde{\tau}_{O,\text{int}}$  is obtained by averaging  $\tilde{A}(k)$  over several independent runs. An example of measuring the integrated autocorrelation time with integration of autocorrelation functions method is

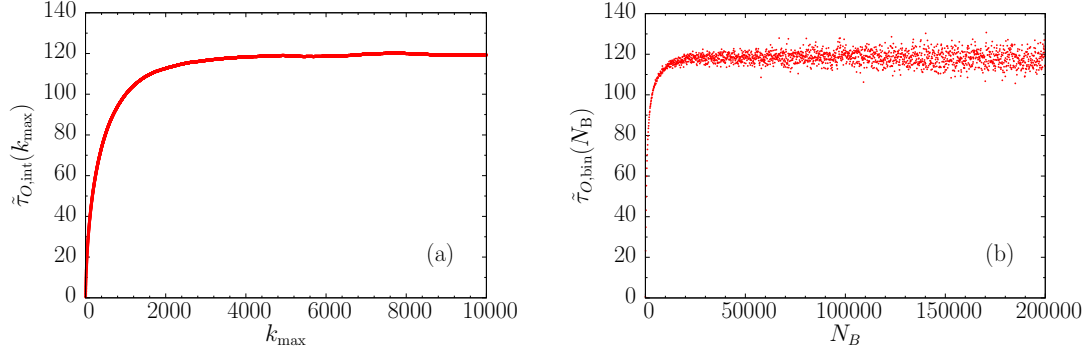


Figure 2.5: Integrated autocorrelation times estimated by (a) the integration of autocorrelation functions and (b) binning analysis.

demonstrated in Fig. 2.5(a). The estimator in this case converges to  $\tilde{\tau}_{O,\text{int}} \approx 120$  (the unit is 30 MCS, i.e., 30 Monte Carlo steps) which corresponds to the estimated value of integrated autocorrelation time.

The standard estimator for the variance of  $O$  is

$$\tilde{\sigma}_O^2 = \overline{O^2} - \overline{O}^2 = \overline{(O - \overline{O})^2} = \frac{1}{N} \sum_{i=1}^N (O_i - \overline{O})^2, \quad (2.18)$$

and its expected value is

$$\begin{aligned} \langle \tilde{\sigma}_O^2 \rangle &= \langle \overline{O^2} - \overline{O}^2 \rangle \\ &= \langle \overline{O^2} \rangle - \langle \overline{O} \rangle^2 - (\langle \overline{O^2} \rangle - \langle \overline{O} \rangle^2) \\ &= \frac{1}{N} \sum_{i=1}^N \langle O_i^2 \rangle - \frac{1}{N^2} \sum_{i,j=1}^N \langle O_i \rangle \langle O_j \rangle - \frac{\sigma_O^2}{N_{\text{eff}}} \\ &= \langle O^2 \rangle - \langle O \rangle^2 - \frac{\sigma_O^2}{N_{\text{eff}}} \\ &= \sigma_O^2 \left( 1 - \frac{1}{N_{\text{eff}}} \right), \end{aligned} \quad (2.19)$$

with  $\sigma_O^2 = \langle O^2 \rangle - \langle O \rangle^2$ . It is obvious that this form systematically underestimates the true

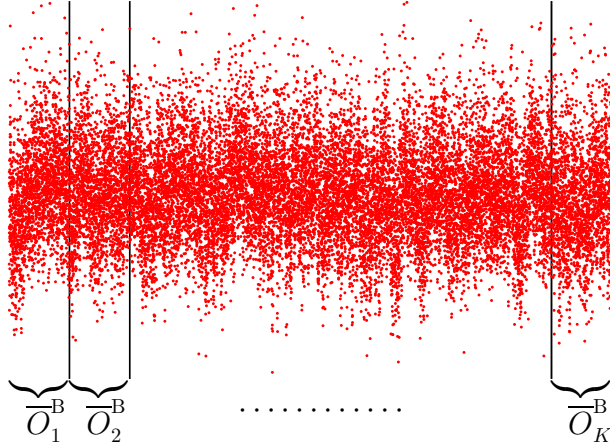


Figure 2.6: A typical time series of quantity  $O$  which is divided into  $K$  binning blocks.  $\overline{O}_1^B$ ,  $\overline{O}_2^B$ , and  $\overline{O}_K^B$  represent the binning block averages of bin 1, 2, and  $K$ , respectively.

value by a term of the order of  $\tau_{O,\text{int}}/N$ . The  $2\tau_{O,\text{int}}/N$  correction is the systematic error due to the finiteness of the time series, and it is called bias. Even in the case in which all the data are uncorrelated ( $\tau_{O,\text{int}} = 1/2$ ), the estimator is still biased,  $\langle \tilde{\sigma}_O^2 \rangle = \sigma_O^2 (1 - 1/N)$ . Thus, it is reasonable to define the bias-corrected estimator

$$\tilde{\sigma}_{O,c}^2 \equiv \frac{N_{\text{eff}}}{N_{\text{eff}} - 1} \tilde{\sigma}_O^2 = \frac{1}{N - 2\tau_{O,\text{int}}} \sum_{i=1}^N (O_i - \overline{O})^2, \quad (2.20)$$

which satisfies  $\langle \tilde{\sigma}_{O,c}^2 \rangle = \sigma_O^2$ . Thus, the bias-corrected estimator for the squared error of the mean value becomes

$$\epsilon_{\overline{O}}^2 = \frac{\tilde{\sigma}_{O,c}^2}{N_{\text{eff}}} = \frac{1}{N(N_{\text{eff}} - 1)} \sum_{i=1}^N (O_i - \overline{O})^2. \quad (2.21)$$

For uncorrelated data, the error formula simplifies to

$$\epsilon_{\overline{O}}^2 = \frac{\tilde{\sigma}_{O,c}^2}{N} = \frac{1}{N(N - 1)} \sum_{i=1}^N (O_i - \overline{O})^2. \quad (2.22)$$

Integrated autocorrelation times can also be estimated by using the so-called binning method

[33]. Assuming that the time series consists of  $N$  correlated measurements  $O_i$ , this time series can be divided into  $K$  bins, which should be large enough so that the correlation of the data in each bin decays sufficiently ( $N_B \gg \tau_{O,\text{int}}$ ). In this way, a set of  $K$  uncorrelated data subsets is generated, each of which contains  $N_B$  data points such that  $N = N_B K$ . The binning block average  $\overline{O}_k^B$  (Fig. 2.6) of the  $k$ -th block is calculated as

$$\overline{O}_k^B = \frac{1}{N_B} \sum_{i=1}^{N_B} O_{(k-1)N_B+i}, \quad k = 1, \dots, K, \quad (2.23)$$

and

$$\overline{O} = \frac{1}{K} \sum_{k=1}^K \overline{O}_k^B, \quad (2.24)$$

coincides with the average (2.9). Since each bin average represents an independent measurement, the variance of the binning block averages  $\sigma_{\overline{O}_k^B}^2$  can be estimated from Eq. 2.20,

$$\tilde{\sigma}_{\overline{O}_k^B, c}^2 = \frac{1}{K-1} \sum_{k=1}^K (\overline{O}_k^B - \overline{O})^2, \quad (2.25)$$

and the statistical error of the mean value  $\epsilon_{\overline{O}}^2 \equiv \sigma_{\overline{O}}^2 = \sigma_{\overline{O}_k^B}^2 / K$  is given by

$$\epsilon_{\overline{O}}^2 = \frac{\tilde{\sigma}_{\overline{O}_k^B, c}^2}{K} = \frac{1}{K(K-1)} \sum_{k=1}^K (\overline{O}_k^B - \overline{O})^2. \quad (2.26)$$

By comparing this expression with Eq. 2.15 and considering Eqs. 2.14 and 2.16, we see that  $\sigma_{\overline{O}_k^B}^2 / K = 2\tau_{O,\text{int}}\sigma_O^2 / N$ . Hence, the autocorrelation time can also be estimated by means of the binning variance as

$$\tilde{\tau}_{O,\text{bin}} = \frac{1}{2} N_B \frac{\tilde{\sigma}_{\overline{O}_k^B, c}^2}{\sigma_O^2}. \quad (2.27)$$

Since the bin averages are supposed to be uncorrelated, we utilize the standard estimator (2.18) for the variance of the individual measurements  $\sigma_O^2$  ( $N \gg 2\tau_{O,\text{int}}$ ). This method is more convenient than the integration method (2.17) since a precise estimate of the autocor-

relation function is not needed. For uncorrelated data and  $N_B = 1$ ,  $\tilde{\sigma}_{O_B,c}^2 = \tilde{\sigma}_O^2$  for  $N \gg 1$ . Consequently  $\tilde{\tau}_{O,\text{bin}} = \tau_{O,\text{int}} = 1/2$ . In the correlated case, too small bin sizes will underestimate the autocorrelation time. Given a time series consisting of  $N$  measurements, the estimator  $\tilde{\sigma}_O^2$  remains unchanged if  $N_B$  is modified. Increasing  $N_B$  reduces the number of bins  $K$  which leads to the decrease of the variance  $\tilde{\sigma}_{O_B,c}^2$ . However, the decrease rate is not the same as  $N_B$  is increased. Thus, the right hand side of (2.27) will converge to a constant value identical to  $\tau_{O,\text{int}}$ . Therefore, one typically plots the right hand side of Eq. 2.27 for various values of  $N_B$  and estimates  $\tau_{O,\text{int}}$  by reading the value the curve converges to [7, 32]. Fig. 2.5(b) shows an example of using binning analysis to estimate integrated autocorrelation time. The estimated value is also about  $\tilde{\tau}_{O,\text{bin}} \approx 120$  (the unit is 30 MCS) which is the same as the one estimated by employing integration of autocorrelation functions method in Fig. 2.5(a).

In the past, most studies analyzing the properties of the autocorrelation times have focused on spin models. The second-order phase transition between ferromagnetism and paramagnetism is characterized by a divergent spatial correlation length  $\xi$  at the transition point  $T_c$ . In the thermodynamic limit (i.e., infinite system size), the divergent behavior is given by  $\xi \sim t^{-\nu}$ , where  $t \equiv |1 - T/T_c|$  and  $\nu$  is a critical exponent [28–30, 32, 34]. If an importance sampling Monte Carlo method is employed [34–36], the number of configurational updates that is needed to decorrelate the information about the history of macroscopic system states is measured by the autocorrelation time  $\tau$ . It is described by the power law  $\tau \propto \xi^z \propto t^{-\nu z}$ , where  $z$  denotes the dynamic critical exponent, which depends on the employed algorithm [30, 32, 34]. However, in a system of finite size, the correlation length can never really diverge. This is because the largest possible cluster has the volume  $L^{d_f}$ , where  $L$  is the system size and  $d_f$  is the fractal dimensionality. Thus, the divergence of the correlation length as well as the autocorrelation time are “cut off” at the boundary, i.e.,  $\xi < L$  or  $\xi \sim L$ . Consequently,  $\tau \sim L^z$  at temperatures sufficiently close to the critical point [30, 32, 34].

For local updates, such as single spin flips, and by using the Metropolis algorithm [37], the autocorrelation time becomes very large near the critical temperature because the dynamic critical exponent is in this case  $z \approx 2$  [30,38,39]. This effect is usually called critical slowing down, but it can be reduced significantly if non-local updates, such as in Swendsen-Wang, Wolff, and multigrid algorithms [30,36,40–45], are employed. Metropolis simulations with local updates yield for the Ising model  $z \approx 2.1665$  in 2D and  $z \approx 2.02$  in 3D [30,38,39]. For non-local updates, numerical estimates yield a  $z$  value less than unity [30,40,42,43,46].

Since most phase transitions in nature are of first order [47–50], it is also useful to discuss autocorrelation properties near first-order phase transitions. In a finite system, the characteristic feature of a first-order pseudophase transition is the double-peaked energy distribution with an entropic suppression regime between the two peaks. The dip is caused by the entropic contribution to the Boltzmann factor  $\propto \exp(-2\sigma L^{d-1})$ , where  $\sigma$  is the (reduced) interface tension and  $L^{d-1}$  is the projected area of the interfaces. Thus, the dynamics in a canonical ensemble will suffer from the “supercritical slowing down”, in which the tremendous average residence time the system spends in a pure phase is described by the autocorrelation time  $\tau \propto \exp(2\sigma L^{d-1})$  [32,51]. Since this slowing down is related to the shape of the energetic probability distribution itself, it is impossible to reduce the autocorrelation time by using cluster or multigrid algorithms. The simulation in a generalized ensemble, such as multicanonical ensemble [52–57], where the slowing down can be reduced to a powerlike behavior with  $\tau \propto L^{d\alpha}$  ( $\alpha \approx 1$ ) [52], can overcome this difficulty.

Based on slowing down and supercritical slowing down, we can utilize the extremal values in the autocorrelation time vs. temperature curves as indicators to locate transition temperatures. This is an alternative approach which can be employed when canonical quantities fail to exhibit pronounced signals. However, due to the algorithm dependencies of autocorrelation times and finite-size effects, this method is also not stable. Certain algorithms or update methods may lead to the disappearance of slowing down. Therefore, it is necessary

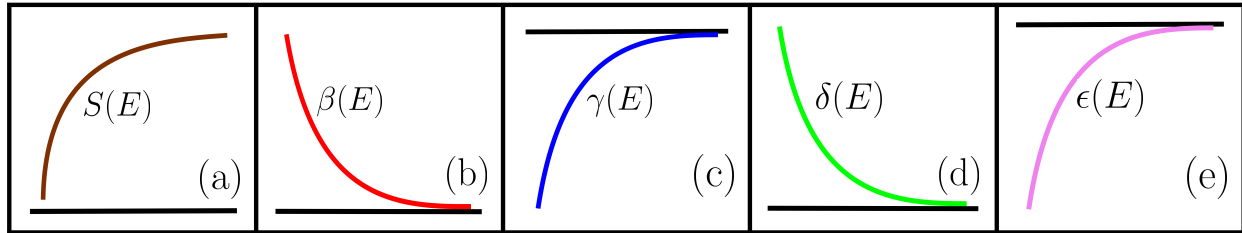


Figure 2.7: (a) is a sketch of microcanonical entropy  $S(E)$  in the condition of no pseudophase transition. Its first- to fourth-order derivatives over energy  $E$  are shown in (b) to (e), respectively. For simplicity, X-axis (energy  $E$ ) and Y-axis ( $S(E)$  or its derivatives) are not plotted in the graphs. Black solid lines represent zero lines of  $S(E)$  or its derivatives.

to employ other systematic and robust methods which can clearly distinguish the sensitive transition signals in finite-size systems.

## 2.3 Microcanonical inflection-point analysis

One of the currently most promising approaches is microcanonical inflection-point analysis [20], which is based on the principle of minimal sensitivity (PMS). The principle of minimal sensitivity was first proposed by Stevenson in order to solve the ambiguity caused by the conventional perturbation theory which gives different results in different renormalization schemes (RS) [18,19]. It asserts that if one only knows the first few terms of a physical quantity's perturbation expansion in some RS and the information that an approximation depends on unphysical parameters of which the true result is independent, then the parameter values should be chosen so as to minimize the sensitivity of the approximant to small variations in those parameters. The PMS has been widely applied and implemented [58–68]. By extending this idea into the microcanonical inflection-point analysis, first- and higher-order pseudophase transitions in finite size systems can be identified uniquely and systematically.

In this approach, the microcanonical entropy given by  $S(E) = k_B \ln g(E)$ , where  $g(E)$

is the conformational density of states, contains the complete information about the pseudophase behavior of a system and it is usually a monotonically increasing concave function in the physically important region as shown in Fig. 2.7(a). The changes of the behavior are signaled by alterations of the curvature of  $S(E)$  and exhibited in the inverse microcanonical temperature defined as

$$\beta(E) \equiv \frac{dS(E)}{dE}. \quad (2.28)$$

The corresponding microcanonical temperature is  $T(E) = \beta^{-1}(E)$ . The  $\beta(E)$  curve is a monotonically decreasing convex function if no pseudophase transition exists (Fig. 2.7(b)). In the canonical ensemble, due to the large correlations within the system at the transition temperature, the expectation value of the system energy  $\langle E \rangle$  will undergo a dramatic increase. In microcanonical analysis, this idea can be extended and the pseudophase transition should occur in energy space where the inverse temperature  $\beta(E)$  behaves least sensitively as energy increases. In the situation where least sensitivity is not observed in  $\beta(E)$ , higher-order derivatives of entropy could be investigated instead. If no pseudophase transition occurs, the derivatives of  $S(E)$  are either monotonically increasing concave or monotonically decreasing convex functions (Fig. 2.7). A change in monotonicity will cause an inflection point at which the curve is least sensitive to the change of the energy, i.e., the increasing/decreasing speed of the derivative curve is the slowest at this point. Such an inflection point is called a least sensitive inflection point. The corresponding pseudophase transition should occur at the least sensitive part of the higher-order derivative curve. This criterion serves as a generalized PMS condition in microcanonical inflection-point analysis and can be employed to identify pseudophase transitions in finite systems hierarchically.

In this scheme, a pseudophase transition between two pseudophases is defined to be of first order if a backbending region is found in  $\beta(E)$  curve and the transition energy  $E_{\text{tr}}$  is located at the inflection point, the corresponding derivative of which is a positive peak

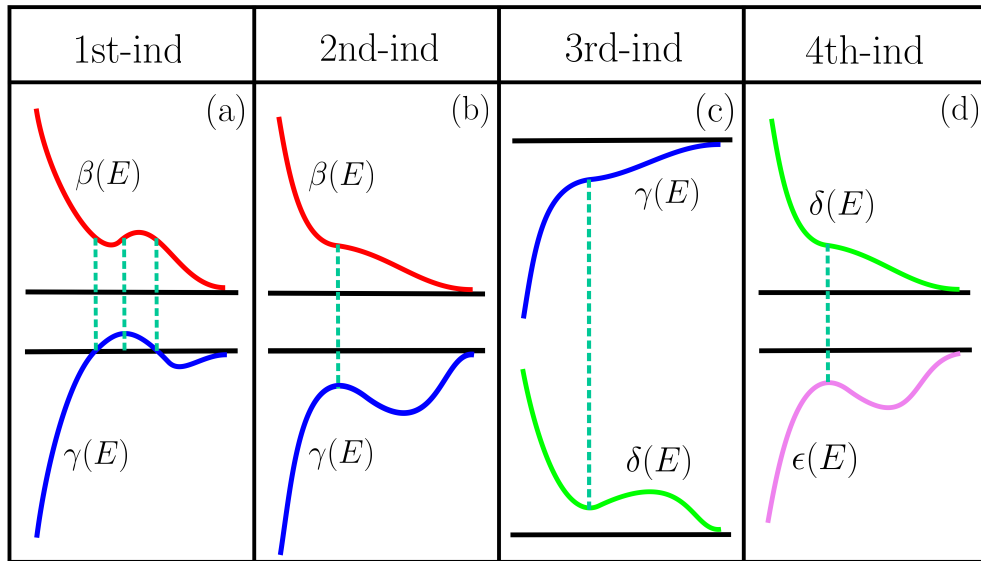


Figure 2.8: (a) A first-order independent pseudophase transition can be identified from the backbending region of  $\beta(E)$  and the positive peak in  $\gamma(E)$ . (b, c, d) For independent pseudophase transitions of second, third, or fourth order, least sensitive inflection points in  $\beta(E)$ ,  $\gamma(E)$ , and  $\delta(E)$  together with the corresponding negative peaks or a positive valley in  $\gamma(E)$ ,  $\delta(E)$ , and  $\epsilon(E)$  are employed to locate pseudophase transition energies. For simplicity, X-axis (energy  $E$ ) and Y-axis (derivatives of microcanonical entropy  $S(E)$ ) are not plotted in the graphs. Black solid lines represent zero lines of the derivatives of  $S(E)$ .

appearing in

$$\gamma(E_{\text{tr}}) = \left. \frac{d^2 S}{dE^2} \right|_{E=E_{\text{tr}}} > 0. \quad (2.29)$$

Since the backbending region can directly form in the monotonically decreasing convex function of  $\beta(E)$  in which no pseudophase transition appears, the occurrence of the corresponding transition is usually independent of the existence of others. For the purpose of simplicity, we denote the independent pseudophase transitions identified by utilizing microcanonical inflection-point analysis as pseudophase transitions in this thesis. The scenario of first-order independent pseudophase transition is plotted as a sketch in Fig. 2.8(a). As being discussed in the Maxwell construction [7–17], the overall energetic width  $\Delta Q$  of the undercooling, backbending, and overheating regions is identical to the latent heat and positive for the first-order pseudophase transition. It is worth noting that the backbending region becomes a flat curve in the thermodynamic limit, which indicates that  $\beta(E)$  is least sensitive to the change of the energy  $E$  in this flat region. For a second-order pseudophase transition, the transition occurs at the inflection point where  $\beta(E)$  is least sensitive to the decreasing trend. The corresponding derivatives around the inflection point show a negative peak, i.e.,

$$\gamma(E_{\text{tr}}) < 0, \quad (2.30)$$

in Fig. 2.8(b). Obviously, no latent heat exists in the pseudophase transition of second order [7, 20, 69, 70]. Like the first-order independent pseudophase transition, the appearance of pseudophase transitions of other than second order is not a necessity for the occurrence of the second-order independent pseudophase transition.

In the cases where no first- or second-order pseudophase transition signal is found, the PMS condition can be extended to the  $\gamma(E)$  curve. Since  $\gamma(E)$  is an increasing concave function in the case of no pseudophase transition (Fig 2.7(c)), an inflection point at which the  $\gamma(E)$  curve behaves least sensitively to the increase is assigned as a third-order pseudophase

transition signal. The derivatives of  $\gamma(E)$  around  $E = E_{\text{tr}}$  for the third-order pseudophase transition will form a positive valley, i.e.,

$$\delta(E_{\text{tr}}) = \left. \frac{d^3 S(E)}{dE^3} \right|_{E=E_{\text{tr}}} > 0, \quad (2.31)$$

as shown in Fig. 2.8(c). This valley can also be utilized to locate the third-order pseudophase transition.

If a lower-order pseudophase transition can not be found, one may assume that the system undergoes a fourth-order pseudophase transition. In the condition of no transition,  $\delta(E)$  is a monotonically decreasing convex function as plotted in Fig. 2.7(d). The sign of a fourth-order pseudophase transition is the least sensitive inflection point in the  $\delta(E)$  curve, i.e., the inflection point at which the  $\delta(E)$  curve decreases most slowly locally. One can also use the negative peak in the  $\epsilon(E)$  curve, i.e.,

$$\epsilon(E_{\text{tr}}) = \left. \frac{d^4 S(E)}{dE^4} \right|_{E=E_{\text{tr}}} < 0, \quad (2.32)$$

as another indicator for the fourth-order pseudophase transition (Fig. 2.8(d)). Note that  $\epsilon(E)$  is a monotonically increasing concave function as shown in Fig. 2.7(e) if no pseudophase transition happens.

The PMS criterion can be extended to the higher order derivatives of  $S(E)$  if no lower than fourth-order pseudophase transition is found. This can be done by analyzing the inflection point of  $\epsilon(E)$ . In summary, the  $2k$ th-order independent pseudophase transition ( $k$  is a positive integer) can be recognized from the least sensitive inflection point in the  $(2k - 1)$ th derivative of  $S(E)$  and the negative peak in the  $2k$ th derivative of  $S(E)$ , i.e.,

$$\left. \frac{d^{2k} S(E)}{dE^{2k}} \right|_{E=E_{\text{tr}}} < 0. \quad (2.33)$$

The  $(2k + 1)$ th-order independent pseudophase transition ( $k$  is still a positive integer) can be distinguished from the least sensitive inflection point in the  $2k$ th derivative of  $S(E)$  and the positive valley in the  $(2k + 1)$ th derivative of  $S(E)$ , i.e.,

$$\left. \frac{d^{(2k+1)}S(E)}{dE^{(2k+1)}} \right|_{E=E_{tr}} > 0 \quad (2.34)$$

[23]. Note that the first-order independent pseudophase transition can only be distinguished from the backbending behavior in  $\beta(E)$  and the positive peak in  $\gamma(E)$ . This is different from the other odd-order independent pseudophase transitions. Since phase transitions in most very large systems (these systems can be regarded as in the thermodynamic limit) are of first- or second-order, pseudophase transitions of higher than second order occurring in finite-size systems may disappear in the thermodynamic limit. However, in nanotechnological and biological systems, where the surface effects probably are very important in determining the structural transitions, higher-order pseudophase transitions may not just appear as side-effects of the first/second-order pseudophase transitions but become the essential signals revealing the structural changes of these finite systems.

Another type of least sensitive inflection point can also be distinguished in the derivatives of microcanonical entropies. The occurrences of the transitions corresponding to these inflection points depend on the existences of lower-order independent pseudophase transitions, i.e., a dependent pseudophase transition of any order can only appear with the pre-existence of a lower-order independent pseudophase transition. For example, a second-order dependent pseudophase transition in Fig. 2.9(a) happens at the least sensitive inflection point where  $\beta(E)$  increases most slowly in a certain region. Since  $\beta(E)$  is a monotonically decreasing convex function in the case of no pseudophase transition, this locally increasing part can only occur in the backbending region of  $\beta(E)$  which indicates the appearance of a first-order independent pseudophase transition. The transition energy can be uniquely located by using

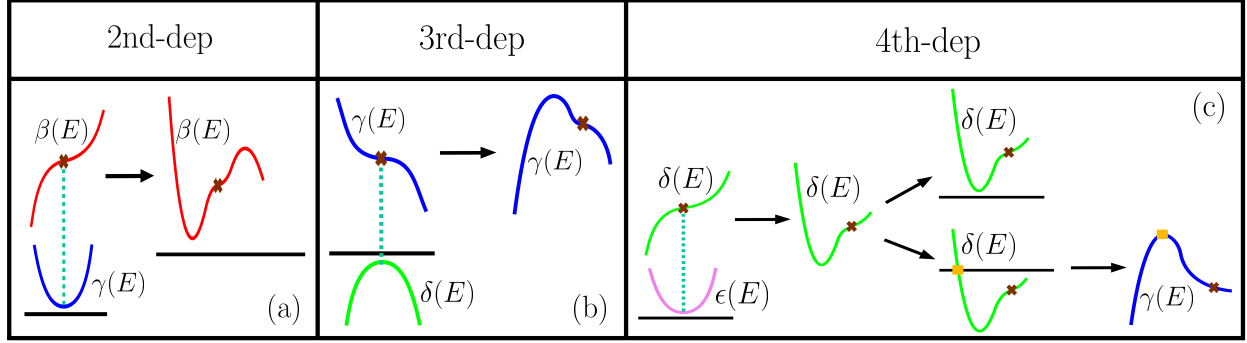


Figure 2.9: (a, b, c) Graphical proofs of dependent pseudophase transitions of second, third, and fourth orders. The transition energies can be identified by employing the least sensitive inflection points and their corresponding positive valleys or a negative peak. For simplicity, X-axis (energy  $E$ ) and Y-axis (derivatives of microcanonical entropy  $S(E)$ ) are not plotted in the graphs. Black solid lines represent zero lines of the derivatives of  $S(E)$ . Same points in different curves in each subgraph are marked by the same signs.

the least sensitive inflection point in  $\beta(E)$  and its corresponding positive valley in  $\gamma(E)$ .

For a third-order dependent pseudophase transition in Fig. 2.9(b), the corresponding least sensitive inflection point usually appears in the certain region where  $\gamma(E)$  decreases. Since  $\gamma(E)$  is a monotonically increasing concave function if there is no pseudophase transition, the occurrence of the decreasing part leads to the formation of a peak in  $\gamma(E)$ , which is an identifier for a first- or second-order independent pseudophase transition. To locate the transition energy, the least sensitive inflection point and the corresponding negative peak in  $\delta(E)$  can be utilized.

Fig. 2.9(c) exhibits the relationship between a fourth-order dependent pseudophase transition and its corresponding lower-order independent pseudophase transitions. The monotonically decreasing property of the  $\delta(E)$  curve in the no “transition” case restrict the occurrence of the least sensitive inflection point in the locally increasing part of  $\delta(E)$ . This inflection point can only appear on the right branch of a valley. If the valley is positive, an independent pseudophase transition of third order can be identified. In the latter case, a  $\delta(E) = 0$  point

on the left branch of the valley can be distinguished if the valley is negative. This zero point indicates the formation of a peak in the  $\gamma(E)$  curve which further reveals the occurrence of either a first- or second-order independent pseudophase transition. The positive valley in the  $\epsilon(E)$  curve is also an indicator for the fourth-order dependent pseudophase transition.

By extending this graphical proof to higher-order pseudophase transitions, we are able to conclude that a dependent pseudophase transition of any order is allowed to happen only with the existence of a lower-order independent pseudophase transition. The energy of a  $2l$ th-order dependent pseudophase transition where  $l$  is a positive integer can be identified from the least sensitive inflection point of  $(2l - 1)$ th derivative of  $S(E)$  and the positive valley in  $2l$ th derivative of  $S(E)$ , i.e.,

$$\left. \frac{d^{2l} S(E)}{dE^{2l}} \right|_{E=E_{\text{tr}}} > 0. \quad (2.35)$$

In addition, for a  $(2l + 1)$ th-order dependent pseudophase transition ( $l$  is a positive integer), the transition energy can be located by employing the least sensitive inflection point in the  $2l$ th derivative of  $S(E)$  and the negative peak in the  $(2l + 1)$ th derivative of  $S(E)$ , i.e.,

$$\left. \frac{d^{(2l+1)} S(E)}{dE^{(2l+1)}} \right|_{E=E_{\text{tr}}} < 0 \quad (2.36)$$

[23]. It is worth noting that the appearance of an independent pseudophase transition does not necessarily imply the occurrence of any lower-order dependent pseudophase transition. Because of the systematic dependencies, dependent pseudophase transitions may represent the precursors of the independent pseudophase transitions and enable an entirely new view on the onset of pseudophase transitions.

Besides the least sensitive inflection points, the inflection points at which the derivatives of microcanonical entropy behave most sensitively can also be observed, i.e., the increasing/decreasing speeds of the derivative curves are the fastest at this point. Such inflection

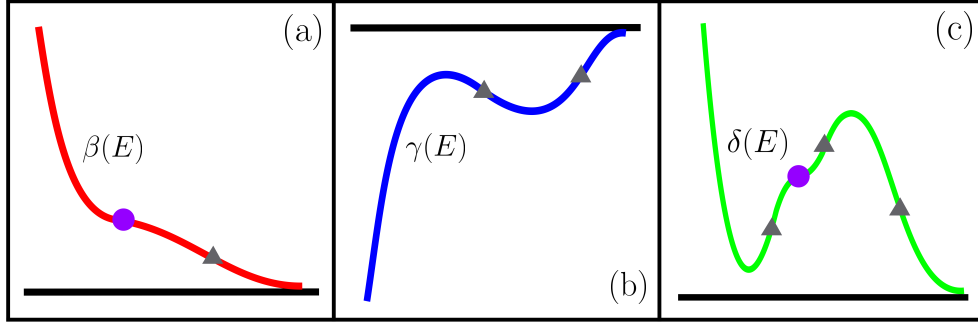


Figure 2.10: Plots (a, b, c) demonstrate the functions of the most sensitive inflection points. For simplicity, X-axis (energy  $E$ ) and Y-axis (derivatives of microcanonical entropy  $S(E)$ ) are not plotted in the graphs. Black solid lines represent zero lines of the derivatives of  $S(E)$ . Least and most sensitive inflection points are marked as purple solid disks and gray triangles, respectively.

points are called most sensitive inflection points. To understand their functions, the physical properties of pseudophase transitions need to be discussed. Pseudophase transitions which are indicated by the least sensitive inflection points and peaks/valleys in the derivatives of microcanonical entropy usually break the general monotonic, convex, and concave properties of the derivative curves. To recover and maintain these general properties, most sensitive inflection points need to be included. For example, in Fig. 2.10(a), a least sensitive inflection point indicating a second-order independent pseudophase transition occurs at low energy in the  $\beta(E)$  curve. Thus,  $\beta(E)$  changes from a convex function to a concave one after this point. In order to recover the convexity, a most sensitive inflection point appears in the higher energy region. In Fig. 2.10(b), the increasing feature of the  $\gamma(E)$  curve is broken by a negative peak which indicates the occurrence of a second-order independent pseudophase transition. To compensate for this effect, a valley connected by a most sensitive inflection point needs to be formed. This inflection point is in charge of changing the concave peak to a convex valley. In order to recover the concavity of  $\gamma(E)$ , another most sensitive inflection point occurs after the valley. The influence of the appearances of dependent pseudophase

transitions on the convexity and concavity of the derivatives of microcanonical entropy is illustrated in Fig. 2.10(c). In this plot, the backbending is observed in the  $\delta(E)$  curve. If there is no dependent pseudophase transition, similar as in Fig. 2.10(b), a most sensitive inflection point will occur in order to change the convex property of the valley so that a concave peak which recovers the decreasing property of  $\delta(E)$  is capable of being formed. Such an inflection point is one of the two most sensitive inflection points within the backbending region. But if a fourth-order dependent pseudophase transition indicated by a least sensitive inflection point emerges in the backbending region, another most sensitive inflection point accompanying this transition point needs to appear to cancel out the effect of the least sensitive inflection point on altering the local convex and concave properties of  $\delta(E)$ . In order to keep  $\delta(E)$  converging to zero in the large energy region, the third most sensitive inflection point occurs on the right side of the peak to make  $\delta(E)$  regain the convex and decreasing properties [23].

Although the discussions above are for the systems with finite size, the scheme of identifying pseudophase transitions in finite systems with microcanonical inflection-point analysis can be extended to the infinite large systems. In these systems, the backbending region in  $\beta(E)$  become flat and the least sensitive inflection points for both the independent and dependent phase transitions become saddle points. The corresponding peaks and valleys reach 0 at the transition energies.

The microcanonical inflection-point analysis is, therefore, a parallel analysis method to the canonical analysis and the autocorrelation time approach. But the ambiguity of locating pseudophase transition temperatures caused by utilizing different order parameters in canonical analysis and autocorrelation times in studying finite-size systems can be avoided in this novel scheme. Analogous to the Ehrenfest scheme in thermodynamics, microcanonical inflection-point analysis can be applied to any kind of system to distinguish and classify the transitions systematically and hierarchically.

# Chapter 3

## Simulation and data smoothing methods

### 3.1 Markov chains and the master equation

Monte Carlo simulations [7, 34] rely on repeated random sampling to obtain random states of a certain distribution which can be further utilized to calculate ensemble averages of quantities. In simulations, Markov process, which is a stochastic process of generating the random states, are usually utilized. The corresponding sequence of the generated states is called a Markov chain. In this mechanism, a new state  $\mathbf{X}_\nu$  of a given system is generated from a previous state  $\mathbf{X}_\mu$  according to the transition probability  $\omega(\mathbf{X}_\mu \rightarrow \mathbf{X}_\nu)$  which is independent of all the states the system has been in with the exception of the previous state  $\mathbf{X}_\mu$ . Such a process is driven by

$$\frac{dp(\mathbf{X}_\mu, t)}{dt} = \sum_{\nu} \omega(\mathbf{X}_\nu \rightarrow \mathbf{X}_\mu)p(\mathbf{X}_\nu, t) - \omega(\mathbf{X}_\mu \rightarrow \mathbf{X}_\nu)p(\mathbf{X}_\mu, t), \quad (3.1)$$

where  $p(\mathbf{X}_\mu, t)$  is the probability of the state  $\mathbf{X}_\mu$  at time  $t$  [34]. Due to particle conservation, the transition probabilities should satisfy the normalization condition  $\sum_\mu \omega(\mathbf{X}_\nu \rightarrow \mathbf{X}_\mu) = 1$ . When the system reaches equilibrium,  $dp(\mathbf{X}_\mu, t)/dt = 0$  which yields the stationary states probabilities  $p(\mathbf{X}_\mu)$  and the balance condition

$$\sum_\nu \omega(\mathbf{X}_\nu \rightarrow \mathbf{X}_\mu) p(\mathbf{X}_\nu) = \sum_\nu \omega(\mathbf{X}_\mu \rightarrow \mathbf{X}_\nu) p(\mathbf{X}_\mu). \quad (3.2)$$

However, balance condition alone allows solutions in which the state probabilities  $p(\mathbf{X}_\mu)$  dynamically change on cycles and the desired probability distribution can not be reached [7, 30]. To eliminate the limit circles, a stronger condition called detailed balance

$$\omega(\mathbf{X}_\nu \rightarrow \mathbf{X}_\mu) p(\mathbf{X}_\nu) = \omega(\mathbf{X}_\mu \rightarrow \mathbf{X}_\nu) p(\mathbf{X}_\mu). \quad (3.3)$$

is needed. Simulational algorithms satisfying this condition can generate a Markov chain of an aimed distribution if appropriate transition probabilities are chosen. To do this, the transition probability  $\omega(\mathbf{X}_\mu \rightarrow \mathbf{X}_\nu)$  can be written as

$$\omega(\mathbf{X}_\mu \rightarrow \mathbf{X}_\nu) = s(\mathbf{X}_\mu \rightarrow \mathbf{X}_\nu) a(\mathbf{X}_\mu \rightarrow \mathbf{X}_\nu) \quad (3.4)$$

where  $s(\mathbf{X}_\mu \rightarrow \mathbf{X}_\nu)$  is the selection probability, which determines the probability of choosing the update from state  $\mathbf{X}_\mu$  to state  $\mathbf{X}_\nu$ , and  $a(\mathbf{X}_\mu \rightarrow \mathbf{X}_\nu)$  is the acceptance probability which controls the chance of accepting the suggested update. Thus, Eq. 3.3 can be written as

$$\frac{a(\mathbf{X}_\mu \rightarrow \mathbf{X}_\nu)}{a(\mathbf{X}_\nu \rightarrow \mathbf{X}_\mu)} = \frac{s(\mathbf{X}_\nu \rightarrow \mathbf{X}_\mu) p(\mathbf{X}_\nu)}{s(\mathbf{X}_\mu \rightarrow \mathbf{X}_\nu) p(\mathbf{X}_\mu)}. \quad (3.5)$$

For the purpose of maximizing the acceptance probabilities, the larger one of the two is usually set to be 1 so that

$$a(\mathbf{X}_\mu \rightarrow \mathbf{X}_\nu) = \min \left( 1, \frac{s(\mathbf{X}_\nu \rightarrow \mathbf{X}_\mu) p(\mathbf{X}_\nu)}{s(\mathbf{X}_\mu \rightarrow \mathbf{X}_\nu) p(\mathbf{X}_\mu)} \right). \quad (3.6)$$

In most of the Monte Carlo simulations, updates for which the selection probabilities  $s(\mathbf{X}_\nu \rightarrow \mathbf{X}_\mu) = s(\mathbf{X}_\mu \rightarrow \mathbf{X}_\nu)$  are usually chosen. The representatives of such updates are single spin flips in the Ising model and space displacements of monomers in polymers. To improve the sampling efficiency, Monte Carlo updates where the selection probabilities are unequal are also introduced [71]. In addition, Monte Carlo updates should also satisfy ergodicity which requires the probability of reaching any state of the system from any other state in a finite number of updates to be non-zero. Based on the ergodic theory, the time average of a quantity  $O$  over an infinitely long time series is equal to its ensemble average, i.e.,

$$\bar{O} = \lim_{N \rightarrow \infty} \sum_{i=1}^N O_i \equiv \langle O \rangle = \int \mathcal{D}\mathbf{X} O(\mathbf{X}) p(\mathbf{X}) \quad (3.7)$$

where  $\mathcal{D}\mathbf{X}$  is the integral measure for the infinitesimal scan of the conformation space and  $p(\mathbf{X})$  represents the probability of a conformation  $\mathbf{X}$  [7]. This relation is the foundation for Monte Carlo simulations. However, only finitely long time series is allowed in simulations. Eq. 3.7 can not rigorously be satisfied. By averaging the finitely long time series of a quantity generated from the Markov process, the statistical ensemble average of a system can be estimated by  $\bar{O} \approx \langle O \rangle$ .

## 3.2 Canonical Metropolis sampling

The standard Monte Carlo simulation method is the Metropolis importance sampling [37] which works in the canonical ensemble and is capable of generating the Boltzmann distribu-

tion which is Gaussian-like and has very small probabilities in the tails. The contribution of the tails to the calculation of ensemble averages is usually negligible. Thus, an efficient sampling should spend most of the efforts on sampling the highly probable region to obtain the relevant information. Metropolis sampling is such an prominent algorithm.

In this method, the target probability of a microstate is identical to the Boltzmann distribution  $p(\mathbf{X}) \sim e^{-\beta E(\mathbf{X})}$  at a given temperature  $T$  ( $\beta = 1/k_{\text{B}}T$ ). The acceptance probabilities of Eq. 3.6 thus become

$$a(\mathbf{X}_\mu \rightarrow \mathbf{X}_\nu) = \min\left(1, e^{-\beta\Delta E}\right) \quad (3.8)$$

where  $\Delta E = E(\mathbf{X}_\nu) - E(\mathbf{X}_\mu)$  and selection probabilities are chosen to be equal. Microstate  $\mathbf{X}_\nu$  is generated through an update such as a single spin flip in the Ising model and a space displacement of a monomer in a polymer. The update will be automatically accepted if  $\Delta E < 0$ . But if the energy of state  $\mathbf{X}_\nu$  is larger, the update will be accepted with the probability  $e^{-\beta\Delta E}$ . Technically, one needs to generate a random number  $r \in [0, 1)$  and only accept the update if  $r < e^{-\beta\Delta E}$ .

The advantage of Metropolis sampling is that it can generate a true physical distribution, namely, a Boltzmann distribution. It can efficiently sample the conformation space at temperatures much higher than the transition temperatures. However, in the simulation at a very low temperature, the sampling might get trapped in a local minimum with the consequence of a large autocorrelation time. In addition, since the Boltzmann distribution at a first-order pseudophase transition temperature in a finite system is bimodal, i.e., two peaks separated by the entropically suppressed energetic region are observed, the simulation might easily get trapped in either one of the two peaks leading to insufficient sampling in the region around the other peak.

### 3.3 Parallel tempering

As discussed before, the Metropolis algorithm is not able to sample the low temperature and phase transition regions efficiently where most of the interesting physics such as ground state structures and pseudophase behavior changes occur. Algorithms that overcome these limitations are developed. Among those methods, parallel tempering [73–76], which is also known as replica-exchange Monte Carlo, is the simplest and popular one. To begin with,  $I$  non-interacting systems in the canonical ensembles with different temperatures  $\beta_1 < \beta_2 < \dots < \beta_I$  are distributed into  $I$  replicas. These systems thus form a generalized ensemble with the joint probability distribution

$$p(\mathbf{X}_1, \mathbf{X}_2, \dots, \mathbf{X}_I) = \frac{e^{-\beta_1 E(\mathbf{X}_1)}}{Z(\beta_1)} \frac{e^{-\beta_2 E(\mathbf{X}_2)}}{Z(\beta_2)} \dots \frac{e^{-\beta_I E(\mathbf{X}_I)}}{Z(\beta_I)} \quad (3.9)$$

where  $Z(\beta_1), Z(\beta_2), \dots, Z(\beta_I)$  are the partition functions of corresponding temperatures [7]. Two combined ways are employed to update the system. The first method involves the local update in one replica of the generalized ensemble. For example, in the Ising model, only a single randomly chosen spin in one replica is allowed to flip. If  $i$ th replica is suggested to do the update, since the selection probability  $s(\mathbf{X}_i \rightarrow \mathbf{X}'_i) = s(\mathbf{X}'_i \rightarrow \mathbf{X}_i)$ , the acceptance probability of Eq. 3.6 thus becomes

$$a(\mathbf{X}_i \leftrightarrow \mathbf{X}'_i) = \min\left(1, e^{-\beta_i \Delta E_i}\right) \quad (3.10)$$

where  $\Delta E_i = E(\mathbf{X}'_i) - E(\mathbf{X}_i)$ . Here, we abbreviate the writing by omitting the terms that don't change. This is just the Metropolis algorithm for replica  $i$ . Another type of update involves swaps of conformations between two chosen replicas. With the choice of identical selection probabilities from both directions, the acceptance probabilities of the swap updates

for replica  $i$  and  $i + 1$  are derived as

$$\begin{aligned}
a(\mathbf{X}_i, \mathbf{X}_{i+1} \leftrightarrow \mathbf{X}_{i+1}, \mathbf{X}_i) &= \min \left( 1, \frac{e^{-\beta_i E(\mathbf{X}_{i+1})} e^{-\beta_{i+1} E(\mathbf{X}_i)}}{e^{-\beta_i E(\mathbf{X}_i)} e^{-\beta_{i+1} E(\mathbf{X}_{i+1})}} \right) \\
&= \min \left( 1, e^{(\beta_{i+1} - \beta_i)(E(\mathbf{X}_{i+1}) - E(\mathbf{X}_i))} \right) \\
&= \min \left( 1, e^{\Delta\beta\Delta E} \right). \tag{3.11}
\end{aligned}$$

In real simulations, since all the replicas are non-interacting, Metropolis runs in each replica can proceed simultaneously. Swap updates can be conducted after hundreds Monte Carlo (MC) sweeps (one MC sweep is equal to the number of system size MC steps). Similar to Metropolis runs, swap updates among multiple replicas can also be carried out simultaneously, due to the exclusive feature of the updates. However, to improve the acceptance rates of conformation exchanges, it is not optimal to choose the swapping replica pairs randomly. This is because the acceptance probabilities in Eq. 3.11 decay exponentially with the increase of  $\Delta\beta\Delta E > 0$ . In simulations, neighboring replicas are often chosen to swap. The temperatures of the neighboring replicas should be close enough to guarantee enough overlap between their corresponding histograms so that high acceptance rates can be achieved.

The paralleling nature of parallel tempering makes its implementation onto multicore processors very convenient [72]. By simulating the same systems at different temperatures simultaneously, parallel tempering can dramatically enhance the computing efficiency. Besides, through conformation exchanges, parallel tempering allows each replica to be heated up and cooled down throughout the whole temperature region so that the autocorrelation times can be decreased [72]. In addition, swap updates can also help configurations that are trapped in metastable states at low temperatures to escape [72]. However, due to the narrow histograms of energy  $h(E)$ , which counts the number of times a certain energy  $E$  has been reached in a simulation, at very low temperatures, very high density of temperatures is required in order to keep reasonable acceptance rates for swap updates. Furthermore, confor-

mation exchanges between two neighboring replicas can be greatly suppressed in first-order transition where a finite gap exists in the energy space. This gap increases the energy difference between the ordered- and disordered-conformations and thus decreases the acceptance probabilities of swap updates. For these reasons, the implementation of parallel tempering to the studies of systems at low temperatures and near first-order transitions becomes crucial [7].

### 3.4 Multiple-histogram reweighting

For the study of phase transitions by utilizing microcanonical inflection-point analysis, the key is to achieve a good estimation of density of states  $g(E)$ . Since  $g(E)$  is directly related to the Boltzmann distribution, the intuitive way is to measure the histogram  $h(E)$  during the simulation and estimate the density of states as

$$\bar{g}(E) = h(E, \beta) e^{-\beta E}. \quad (3.12)$$

However, in the canonical ensemble, accurate data can only be obtained in a certain energy region at a given temperature. The consequence is that the estimate of the density of states can only be valid in the region that the histogram covers. Therefore, a sophisticated algorithm needs to be employed in order to combine the estimates of the density of states which are obtained at different temperatures and overlap in energy. One of such approaches is the “weighted histogram analysis method” (WHAM) [77, 78]. In this method, the combined estimate of density of states is

$$\hat{g}(E) = \frac{\sum_{i=1}^I h_i(E)}{\sum_{i=1}^I M_i \hat{Z}_i^{-1} e^{-\beta_i E}} \quad (3.13)$$

and the corresponding estimate of the partition function of  $i$ th thread is

$$\hat{Z}_i = \sum_E \hat{g}(E) e^{-\beta_i E}. \quad (3.14)$$

Here,  $M_i$  is the length of the time series at temperature  $T_i = 1/k_B\beta_i$ . These two estimates can be solved iteratively. The procedure is as follows. The initial estimate of  $\hat{Z}_i^{(0)}$  is first guessed which can be used to estimate  $\hat{g}^{(1)}(E)$  by utilizing the histogram  $h_i(E)$ . The results can be inserted into Eq. 3.14 to calculate  $\hat{Z}_i^{(1)}$ . This process needs to be repeated until both of the estimates converge to constant values [7].

### 3.5 Multicanonical sampling

The shortcomings of parallel tempering at low temperatures and near first-order transitions implies the necessity of finding another generalized ensemble which can increase the sampling of the tails of the Boltzmann distribution and improve the sampling rates of the lowest-energy conformations and of the entropically suppressed region in the first-order transitions [7]. A prominent algorithm is called multicanonical sampling [52, 79, 80] which can obtain the statistics of all temperatures in a single run [81]. The strategy of multicanonical sampling is to multiply a weight function  $W_{\text{muca}}(E, T)$  to the Boltzmann distribution  $p_{\text{can}}(E, T) \sim g(E)e^{-\beta E}$  so that a flat distribution  $p_{\text{muca}}(E, T) \sim g(E)e^{-\beta E}W_{\text{muca}}(E, T) \approx \text{const.}$  can be achieved. In this generalized ensemble, the acceptance probability of an update is

$$\begin{aligned} a(X_\mu \rightarrow X_\nu) &= \min \left( 1, \frac{p_{\text{muca}}(X_\nu, T)}{p_{\text{muca}}(X_\mu, T)} \right) \\ &= \min \left( 1, \frac{W_{\text{muca}}(E(X_\nu), T) e^{-\beta E(X_\nu)}}{W_{\text{muca}}(E(X_\mu), T) e^{-\beta E(X_\mu)}} \right) \\ &= \min \left( 1, \frac{W_{\text{muca}}(E(X_\nu), T)}{W_{\text{muca}}(E(X_\mu), T)} e^{\beta(E(X_\mu) - E(X_\nu))} \right). \end{aligned} \quad (3.15)$$

Here, the equal selection probabilities have been employed. However, the weight functions usually can not be known before simulations. Otherwise, the density of states can be directly calculated from them. Therefore, one can usually start the simulation with an initial guess for the weight functions and employ the standard recursion [7, 79, 80, 82] or its error-weighted version [7, 79, 80] to iteratively estimate the weight functions until they converge to constant values. The initial weight functions can be set to any arbitrary values which only affect the convergence speed but not the final results. To improve the speed, initial runs with the Metropolis method are often utilized to roughly estimate the density of states which is further used to generate the initial weight functions. In the error-weighted recursion process, the  $(n+1)$ th weight functions  $W_{\text{muca}}^{(n+1)}(E, T)$  can be calculated from the  $n$ th weight functions  $W_{\text{muca}}^{(n)}(E, T)$  and histograms  $h_{\text{muca}}^{(n)}(E)$

$$\frac{W_{\text{muca}}^{(n+1)}(E, T)}{W_{\text{muca}}^{(n+1)}(E - \Delta E, T)} = \frac{W_{\text{muca}}^{(n)}(E, T)}{W_{\text{muca}}^{(n)}(E - \Delta E, T)} \left( \frac{h_{\text{muca}}^{(n)}(E - \Delta E)}{h_{\text{muca}}^{(n)}(E)} \right)^{\alpha^{(n)}(E)} \quad (3.16)$$

[7, 79]. Here,  $\alpha^{(n)}$  is defined as

$$\alpha^{(n)}(E) = \frac{w_n(E)}{\sum_{i=0}^n w_i(E)} \quad (3.17)$$

where

$$w_j(E) = \frac{h_{\text{muca}}^{(j)}(E)h_{\text{muca}}^{(j)}(E - \Delta E)}{h_{\text{muca}}^{(j)}(E) + h_{\text{muca}}^{(j)}(E - \Delta E)}. \quad (3.18)$$

After the best estimates of weight functions are achieved, it is necessary to perform a long multicanonical production run to generate the multicanonical time series which can be utilized to estimate the canonical expectation values of quantities  $O$  at any temperature  $T'$  as

$$\bar{O}_{\text{can}}(T') = \frac{\sum_t O(X_t) W_{\text{muca}}^{-1}(E(X_t), T) e^{(\beta - \beta')E(X_t)}}{\sum_t W_{\text{muca}}^{-1}(E(X_t), T) e^{(\beta - \beta')E(X_t)}}. \quad (3.19)$$

For the calculation convenience, the temperature at which multicanonical sampling is performed is usually set to be infinity because it does not have any meaning in the multicanonical ensemble [7]. Thus, weight functions can be abbreviated as  $W_{\text{muca}}(E) \sim g(E)^{-1}$ . Equation 3.15, 3.16, and 3.19 become

$$a(X_\mu \rightarrow X_\nu) = \min \left( 1, \frac{W_{\text{muca}}(E(X_\nu))}{W_{\text{muca}}(E(X_\mu))} \right), \quad (3.20)$$

$$\frac{W_{\text{muca}}^{(n+1)}(E)}{W_{\text{muca}}^{(n+1)}(E - \Delta E)} = \frac{W_{\text{muca}}^{(n)}(E)}{W_{\text{muca}}^{(n)}(E - \Delta E)} \left( \frac{h_{\text{muca}}^{(n)}(E - \Delta E)}{h_{\text{muca}}^{(n)}(E)} \right)^{\alpha^{(n)}(E)}, \quad (3.21)$$

and

$$\bar{O}_{\text{can}}(T') = \frac{\sum_t O(X_t) W_{\text{muca}}^{-1}(E(X_t)) e^{-\beta' E(X_t)}}{\sum_t W_{\text{muca}}^{-1}(E(X_t)) e^{-\beta' E(X_t)}}, \quad (3.22)$$

respectively. It is worth mentioning that multicanonical sampling can work with weights depending on any arbitrary order parameters  $W_{\text{muca}}(Q)$  and generate flat histograms in the order parameter  $Q$  space. In addition, another alternative method to directly obtain the estimate of density of states is to utilize Wang-Landau method [83] in which iterations of weight functions can be avoided.

Like parallel tempering, multicanonical sampling can also be parallelized in order to improve running efficiency. A commonly used simple parallelization scheme [84] is to first perform the standard multicanonical runs in  $I$  replicas independently with the same initial weight functions but different random seeds. After the  $k$ th iteration, since the weights are identical in each thread, the energy histograms obtained for each replica can simply be summed up:

$$H^k(E) = \sum_{i=1}^I H_i^k(E). \quad (3.23)$$

The total histograms are combined with the current weights to calculate the weights for the subsequent iteration by utilizing the error-weighted recursive scheme.

## 3.6 Displacement update

To increase the efficiency of the simulations, advanced sampling algorithms must be combined with sophisticated conformational updates. These updates must not only satisfy the ergodicity, i.e., any state can be reached from any other state with non-zero probability, but also need to obey detailed balance. One of the most commonly used updates in the study of off-lattice polymer systems, which is a coarse-grained model for polymers such as proteins in continuous space and will be discussed in Chapter 4 and 6, is the displacement update. In this update, one monomer is randomly chosen to shift its position within a small cubic box with edge length  $l$ . Technically, one needs to generate three uniformly distributed random numbers  $r_i \in [0, 1)$ . The displacement  $\vec{d}$  can be calculated as

$$d_i = 2 \times l \times r_i - l, \tag{3.24}$$

where  $d_i$  are the 3 Cartesian components of  $\vec{d}$ . The acceptance of the suggested update is determined by the acceptance probabilities (Eq. 3.6) of the Monte Carlo method used. The displacement update can be applied to all the atoms in a chain either sequentially or randomly. Once the whole chain is updated, it is said that a Monte Carlo sweep has been performed. In practice, it is not optimal to set the displacement box length to be a fixed value for all the temperatures because the acceptance probabilities vary with temperature. For example, for a system in the canonical ensemble at low temperature,  $l = 0.4$  will lead to a large energy difference when the displacement update is applied. Thus, most of the updates will be rejected. However, for a system at high temperature, this displacement will be too small to yield an efficient sampling in energy space. Both of the scenarios end up with the consequence of increased autocorrelation times. Therefore, the size of the box  $l$  should be adjusted for every temperature thread separately prior to the simulation in order to achieve a Metropolis acceptance rate of approximately 50%. In addition, the displacement

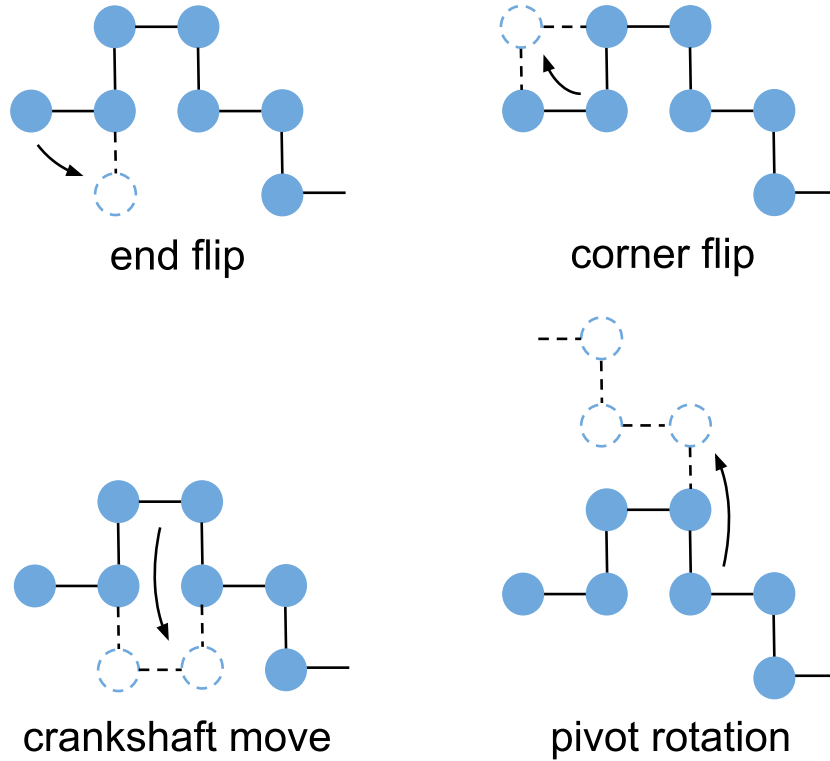


Figure 3.1: Sketches of Monte Carlo updates (end and corner flips, crankshaft moves, and pivot rotations) used for updating polymers on a square lattice.

update apparently satisfies ergodicity and detailed balance because each conformation can be eventually reached out from any other and the selection probabilities  $s(X_\mu \rightarrow X_\nu) = s(X_\nu \rightarrow X_\mu)$ .

### 3.7 Chain-growth algorithm

For the studies of lattice proteins and polymers, the standard Markov chain Monte Carlo methods as described in the previous Sec. 3.1 can be employed. In these methods, as shown in Fig. 3.1, the commonly used Monte Carlo updates include semilocal changes of bond orientations such as end and corner flips, crankshaft moves [85–88], and nonlocal transformations

such as pivot rotations [7, 81, 89]. However, the update of conformations becomes inefficient when standard Monte Carlo updates are employed to study regular lattice systems with small coordination numbers. This disadvantage becomes more critical when the polymer is in a dense conformation.

To compensate for this disadvantage, a completely different approach based on chain growth was introduced. In this approach, the  $l$ th monomer is randomly attached to one of the unoccupied nearest neighbors of the  $(l - 1)$ th monomer. The growth will be terminated if the whole polymer length  $N$  has been reached or all of the nearest neighboring sites of the  $(l - 1)$ th monomer has been occupied. However, this simple chain growth is very inefficient, because the number of discarded chains increases exponentially with the chain length [7]. By introducing the Rosenbluth chain growth method [90], the performance can be greatly improved. In this method, each growth is assigned a Rosenbluth weight which is the number of unoccupied nearest neighbors  $m_l$  of the  $(l - 1)$ th monomer. The total Rosenbluth weight of a chain of length  $n$  can be calculated as

$$W_n^R = \prod_{l=2}^n m_l. \quad (3.25)$$

To further improve the running efficiency, one needs to employ the Pruned-Enriched Rosenbluth Method (PERM) [91–93] in which the (a-thermal) Rosenbluth weight factor  $W_n^R$  is replaced by

$$W_n^{\text{PERM}} = \prod_{l=2}^n m_l e^{-\beta(E_l - E_{l-1})/k_B T}, \quad 2 \leq n \leq N \quad (E_1 = 0, W_1^{\text{PERM}} = 1) \quad (3.26)$$

where  $E_l$  is the energy of a partial chain of length  $l$ . In PERM, the population of the chains is controlled by introducing two empirical parameters  $W_n^>$  and  $W_n^<$ . If  $W_n^{\text{PERM}} > W_n^>$ , an identical chain is created and the weight is equally divided among them. For the case of  $W_n^{\text{PERM}} < W_n^>$ , a random number  $r \in [0, 1)$  is first generated and the growth is stopped if

$r < 1/2$ . The chain is preserved if  $r > 1/2$  and the weight is doubled in order to retain the overall weight of the sample. The enriching and pruning processes are not started if  $W_n^{\text{PERM}}$  lies between the two thresholds and the chain continues growing as in the regular Rosenbluth sampling. The enriching process can be improved by creating  $2 \leq k \leq m_n$  different copies in the so-called “new PERM” variants  $\text{nPERM}_{\text{is}}^{\text{ss}}$  [new PERM with simple/importance sampling (ss/is)] [7,94] so that the similar evolution caused by the identical copies can be eliminated. To determine the number of copies  $k$ , a predicted weight  $W_n^{\text{pred}}$  of length  $n$  is calculated and compared with the upper threshold:

$$k = \min \left\{ m_n, \text{int} \left( \frac{W_n^{\text{pred}}}{W_n^>} \right) \right\}. \quad (3.27)$$

The final weight of each of the  $k$  selected sites  $\alpha_j$  ( $j \in \{1, \dots, k\}$ ) where the chain continues to grow is

$$W_{n,\alpha_j}^{\text{nPERM}_{\text{is}}^{\text{ss}}} = W_{n-1}^{\text{nPERM}_{\text{is}}^{\text{ss}}} \frac{m_n}{k \binom{m_n}{k}} P_A e^{-\beta(E_n^{(\alpha_j)} - E_{n-1})}, \quad (3.28)$$

where

$$P_A = \frac{\sum_{\alpha \in A} \chi_{\alpha}^{\text{nPERM}_{\text{is}}^{\text{ss}}}}{\sum_A \sum_{\alpha \in A} \chi_{\alpha}^{\text{nPERM}_{\text{is}}^{\text{ss}}}} \quad (3.29)$$

is the probability of selecting a certain  $k$ -tuple  $A = \{\alpha_1, \dots, \alpha_k\}$  of different continuations with

$$\chi_{\alpha}^{\text{nPERM}_{\text{ss}}} = 1, \quad \chi_{\alpha}^{\text{nPERM}_{\text{is}}} = \left( m_n^{(\alpha)} + \frac{1}{2} \right) e^{-\beta(E_n^{(\alpha)} - E_{n-1})}, \quad (3.30)$$

$E_n^{(\alpha)}$  represents the energy of the polymer after placing the  $n$ th monomer at site  $\alpha \in [1, m_n]$ , and  $m_n^{(\alpha)}$  denotes the number of free neighbors to place the  $(n+1)$ th monomer after this choice. Since information about  $(n+1)$ th continuation is also contained in  $\chi_{\alpha}^{\text{nPERM}_{\text{is}}}$ , chains grow better when  $\chi_{\alpha}^{\text{nPERM}_{\text{is}}}$  are considered. Another improvement is that by utilizing the number of successfully created chains  $n$  and the current estimate of the partition sum, the thresholds can be dynamically adjusted [7]. To estimate the density of states for the whole

energy range, simulations running with the nPERM method at different temperatures needs to be conducted. The densities of states valid in certain energy ranges at each temperature need to be combined by means of multiple-histogram reweighting method [77, 78].

### 3.8 Multicanonical chain-growth algorithm

However, the statistical errors in each histogram is difficult to be tracked if nPERM is utilized. Another powerful approach in which density of states can be obtained in a single simulation is the multicanonical chain-growth method [95, 96]. In this method, an additional weight  $W_n^{\text{flat}}$  is introduced into the partition function

$$Z_n = \frac{1}{c_1} \sum_t W_n^{\text{nPERM}_{\text{is}}^{\text{ss}}}(\mathbf{X}_{n,t}) W_n^{\text{flat}}(E(\mathbf{X}_{n,t})) \left[ W_n^{\text{flat}}(E(\mathbf{X}_{n,t})) \right]^{-1} \quad (3.31)$$

in order to achieve a flat distribution in energy. Here,  $t$  counts the generated conformations with  $n$  monomers and  $c_1$  is the number of chain growth starts. For  $T \rightarrow \infty$ ,  $W_n^{\text{flat}}(E) \sim g_n^{-1}(E)$  and the partition function in Eq. 3.31 can be written as

$$\begin{aligned} Z_n &= \frac{1}{c_1} \sum_t g_n(E(\mathbf{X}_{n,t})) \left[ W_n^{\text{nPERM}_{\text{is}}^{\text{ss}}}(\mathbf{X}_{n,t}) W_n^{\text{flat}}(E(\mathbf{X}_{n,t})) \right] \\ &= \frac{1}{c_1} \sum_t g_n(E(\mathbf{X}_{n,t})) W_n(\mathbf{X}_{n,t}). \end{aligned} \quad (3.32)$$

When weights  $W_n$  are taken as the probabilities to generate chains of length  $n$ ,  $p_n \sim W_n$ , desired flat histograms  $H_n(E)$  which are further used to calculate the density of states

$$g_n(E) \sim \frac{H_n(E)}{W_n^{\text{flat}}(E)} \quad (3.33)$$

can be obtained [7]. The canonical distribution at temperature  $T$  is then calculated as

$$p_n^{\text{can},T}(E) \sim g_n(E)e^{(-E/k_B T)} \quad (3.34)$$

where  $k_B$  is the Boltzmann constant.

In simulations,  $W_n^{\text{flat}}(E)$ , which are usually not known in advance, can be estimated iteratively. In the zeroth iteration, a pure nPERM<sub>is</sub><sup>ss</sup> run is conducted with the initial guess of  $W_n^{\text{flat},(0)}(E) = 1$  and  $H_n^{(0)}(E) = 0$  for all chains  $2 \leq n \leq N$ . The accumulated histogram of all generated chains of length  $n$  after the zeroth iteration can be calculated as

$$H_n^{(0)}(E) = \sum_t W_{n,t}^{\text{nPERM}_{\text{is}}^{\text{ss}}} \delta_{E_t, E} \quad (3.35)$$

which can be further utilized to calculate the multicanonical weights for the 1st iteration

$$W_n^{\text{flat},(1)}(E) = \frac{W_n^{\text{flat},(0)}(E)}{H_n^{(0)}(E)} \quad \forall n, E. \quad (3.36)$$

With these weights, a flat histogram in the first iteration can be obtained.

The first and following iterations are multicanonical chain-growth runs. For the  $i$ th run, histograms will be first reset,  $H_n^{(i)}(E) = 0$ . The thresholds which can be determined dynamically in each iteration are first set to be  $W_n^> = \infty$  and  $W_n^< = 0$ . A predicted weight  $W_n^{\text{pred}}$  for adding the  $n$ th monomer is introduced as

$$W_n^{\text{pred}} = W_{n-1}^{\text{ss, is}} \sum_{\alpha=1}^{m_n} \chi_{\alpha}^{\text{ss, is, (i)}} \quad (3.37)$$

where the importances  $\chi_{\alpha}^{\text{ss, is, (i)}}$  are defined as

$$\chi_{\alpha}^{\text{ss, (i)}} = 1, \quad \chi_{\alpha}^{\text{is, (i)}} = \left( m_n^{(\alpha)} + \frac{1}{2} \right) \frac{W_n^{\text{flat}, (i)}(E_n^{(\alpha)})}{W_{n-1}^{\text{flat}, (i)}(E_{n-1})}. \quad (3.38)$$

$W_n^{\text{pred}}$  are employed to compare with the thresholds  $W_n^{<,>}$ . If  $W_n^{\text{pred}} > W_n^>$ ,  $k$  number of copies calculated with Eq. 3.27 can be generated. The final weight of each of the  $k$  selected sites  $\alpha_j$  ( $j \in \{1, \dots, k\}$ ) where the chain continues to grow is

$$W_{n,\alpha_j}^{\text{ss,is}} = W_{n-1}^{\text{ss,is}} \frac{m_n}{k \binom{m_n}{k}} P_A \frac{W_n^{\text{flat},(i)}(E_n^{(\alpha_j)})}{W_{n-1}^{\text{flat},(i)}(E_{n-1})}, \quad (3.39)$$

in which

$$P_A = \frac{\sum_{\alpha \in A} \chi_{\alpha}^{\text{ss,is},(i)}}{\sum_A \sum_{\alpha \in A} \chi_{\alpha}^{\text{ss,is},(i)}} \quad (3.40)$$

is the probability of selecting a certain  $k$ -tuple  $A = \{\alpha_1, \dots, \alpha_k\}$ . The strategy of choosing the  $k$  sites to place the  $n$ th monomer according to probabilities  $P_A$  is the following. After calculating the probabilities for all the tuples, we consider the  $P_A$  as partial intervals of certain length and arranged successively in the total interval  $[0, 1]$ . Afterwards, a random number  $r \in [0, 1)$  is generated. The final tuple which is chosen to continue the growth is the one whose corresponding partial interval contains  $r$ . For the simple sampling case,  $P_A = 1/\binom{m_n}{k}$ . If  $W_n^< \leq W_n^{\text{pred}} \leq W_n^>$ , one of the  $m_n$  sites is chosen to place the  $n$ th monomer and the corresponding weight can be calculated with Eq. 3.39 by setting  $k = 1$ . For the case in which  $W_n^{\text{pred}} < W_n^<$ , the growth of the chain is stopped with probability  $1/2$  and can be continued at the last branching point. If no branching points exist, a new tour needs to be started. But if the chain survives, a new site for the growth of the  $n$ th monomer is chosen based on probability  $P_A$  in Eq. 3.40 ( $k$  is set to be 1) and the corresponding weight calculated by using Eq. 3.39 is doubled. The threshold values are determined via

$$W_n^> = C_1 Z_n^{\text{flat}} \frac{C_n^2}{C_1^2}, \quad W_n^< = C_2 W_n^> \quad (3.41)$$

where  $C_1, C_2 \leq 1$  are constants and the estimated partition sum is

$$Z_n^{\text{flat}} = \frac{1}{c_1} \sum_t W_{n,t}^{\text{ss,is}}. \quad (3.42)$$

$Z_n^{\text{flat}}$  and  $c_1$  are set to zero when a new iteration starts. In each iteration, the histograms of energy  $E$  with chain length  $n$  are estimated by

$$H_n^{(i)}(E) = \sum_t W_{n,t}^{\text{ss,is}} \delta_{E_t,E}, \quad (3.43)$$

and the corresponding multicanonical weights for  $(i+1)$ th iteration are

$$W_n^{\text{flat,(i+1)}}(E) = \frac{W_n^{\text{flat,(i)}}(E)}{H_n^{(i)}(E)} \quad \forall n, E. \quad (3.44)$$

Once the desired flat histogram is achieved in the  $I$ th iteration, the final density of states can be estimated by [7]:

$$g_n^{(I)}(E) = \frac{H_n^{(I)}(E)}{W_n^{\text{flat,(I)}}(E)}, \quad 2 \leq n \leq N. \quad (3.45)$$

### 3.9 Bézier smoothing

Computational results obtained in simulations are usually discrete values. For example, to estimate microcanonical entropy  $S(E)$ , the energy space needs to be divided into separate energy bins. The density of states associated with each energy bin can be recursively calculated by utilizing multicanonical sampling with an error-weighted recursion scheme. However, to study the structural transitions of a system with microcanonical inflection-point analysis, an analytical form of  $S(E)$  is very helpful for calculating its derivatives. One powerful method that can be utilized to generate a smooth, continuous function for  $S(E)$  by using a few con-

control points is to employ Bézier curves [97,98] which are commonly used in computer graphics and product design.

Bézier smoothing works in the following way. Imagine  $n$  data points denoted as  $\mathbf{P}$  have been generated from a simulation. They can be used as control points to construct the Bézier curve through

$$\mathbf{B}(t) = \sum_{j=0}^n \mathcal{B}_j^{(n)}(t) \mathbf{P}_j \quad (3.46)$$

where  $t \in [0, 1]$  is the path parameter which allows one to traverse the smoothed curve,  $\mathbf{B}(t)$  represent the smoothed data points, and the expansion coefficients  $\mathcal{B}_j^{(n)}(t)$  are the Bernstein basis polynomials:

$$\mathcal{B}_j^{(n)}(t) = \binom{n}{j} (1-t)^{n-j} t^j. \quad (3.47)$$

Here, the superscript  $(n)$  in  $\mathcal{B}_j^{(n)}$  denotes the degree of construction level [7]. Note that the endpoints of  $\mathbf{B}$  coincide with  $\mathbf{P}_0$  and  $\mathbf{P}_n$  because  $\mathcal{B}_j^{(n)}(0) = \delta_{j0}$  and  $\mathcal{B}_j^{(n)}(1) = \delta_{jn}$ . For a fixed  $t$ , because of the similar forms and normalization property

$$\sum_{j=0}^n \mathcal{B}_j^{(n)}(t) = 1 \quad \forall t \in [0, 1], \quad (3.48)$$

the expansion coefficients  $\mathcal{B}_j^{(n)}(t)$  can be regarded as the binomial probability distribution.

In the microcanonical analysis, microcanonical entropy and its derivatives depend only on energy. Therefore, it will be convenient to write Eq. 3.46 in the two dimensional form. For control points  $y_j$  equally spaced in  $x$  space on the interval  $[x_0, x_n]$ ,  $x_j = x_0 + j(x_n - x_0)/n$ , the smoothed  $x$  can be written as

$$\begin{aligned} x(t) &= \sum_{j=0}^n \binom{n}{j} (1-t)^{n-j} t^j x_j \\ &= \sum_{j=0}^n \binom{n}{j} (1-t)^{n-j} t^j [x_0 + j(x_n - x_0)/n] \end{aligned}$$

$$\begin{aligned}
&= x_0 + (x_n - x_0) \sum_{j=0}^n \binom{n}{j} (1-t)^{n-j} t^j j/n \\
&= x_0 + (x_n - x_0) \sum_{j=1}^n \frac{(n-1)!}{(j-1)!(n-j)!} (1-t)^{n-j} t^j \\
&= x_0 + (x_n - x_0) \sum_{j=0}^{n-1} \frac{(n-1)!}{j!(n-1-j)!} (1-t)^{n-1-j} t^{j+1} \\
&= x_0 + t(x_n - x_0) \sum_{j=0}^{n-1} \binom{n-1}{j} (1-t)^{n-1-j} t^j \\
&= x_0 + t(x_n - x_0)
\end{aligned} \tag{3.49}$$

and the corresponding smoothed  $y$  becomes

$$y_{\text{bez}}(x) = \sum_{j=0}^n \binom{n}{j} \left( \frac{x_n - x}{x_n - x_0} \right)^{n-j} \left( \frac{x - x_0}{x_n - x_0} \right)^j y_j \tag{3.50}$$

where  $t = (x - x_0)/(x_n - x_0)$  has been utilized [7]. The power of Bézier smoothing is that it can uniquely map the noisy control data into a smoothly interpolating, analytic function. This property is particularly beneficial for the microcanonical inflection-point analysis in which microcanonical entropy and its derivatives usually need to be smoothed in order to identify the physical transition signals. To test the power of Bézier smoothing, an example is shown in Bachmann's book [7]. In that example, a smoothed curve is first constructed from the noise data which is generated by adding noise to the original data of a damped polynomial function mimicking the first-order-like transition. After comparing the smoothed curve with the original function, one can conclude that the smoothed curve greatly reproduces all qualitative large-scale features of the damped polynomial function with much smaller numerical error than the error of the noise data.

# Chapter 4

## Flexible polymer

### 4.1 Introduction

The necessity for a better understanding of general physical principles and mechanisms of structural transitions of polymers, such as folding, aggregation, and the adsorption at substrates has provoked numerous computational studies of polymer models [12, 13, 99–130]. Autocorrelation properties of such models govern the statistical accuracy of estimated expectation values of physical quantities but also help illustrate the dynamic behavior or the relaxation properties. Verdier and co-workers were among the first to investigate autocorrelations of a simple lattice polymer approach, in which the Brownian motion of the monomers is simulated by kinetic displacements of single monomers [131–134]. By using Monte Carlo methods, the autocorrelation functions and relaxation times of structural quantities were calculated in order to study dynamic properties of random-coil polymer chains such as the relaxation of asphericity in lattice model chains with and without excluded volume interaction [135, 136]. More recently, these studies were extended to continuous models, where autocorrelation properties of the center-of-mass velocity, Rouse coordinates, end-to-end distance, end-to-end vector, normal modes, and the radius of gyration for polymer melts [137–139],

and of dynamic quantities of a polymer immersed in a solution [140–146] were investigated. Integrated autocorrelation times are also employed to judge the efficiency of importance-sampling algorithms [147]. However, much less is known about how autocorrelation times and structural transitions of polymers depend on each other.

In this chapter, we will investigate autocorrelation properties of different quantities for elastic, flexible polymers, described by a simple coarse-grained model. The thermodynamic behavior of the system is simulated by local monomer displacement and Metropolis Monte Carlo sampling, resembling Brownian dynamics in a canonical ensemble. Brownian dynamics is used to describe the Brownian motion of particles suspended in a fluid, i.e., random motions of particles caused by the collision with the fast moving particles in the fluid. The goal is to identify structural transitions and transition temperatures for this model.

## 4.2 Model and simulation method

### 4.2.1 Model

For our study, we use a generic model of flexible, elastic polymer chains of length  $L = 30$  and  $55$  [7]. This is a coarse-grained model for the actual polymers such as proteins, DNA, and polystyrene. In this model, all the atoms in each monomer, which is the repeated subunit of polymers, are grouped together and represented by an effective interaction bead. The quantum interactions among all the atoms of the polymers, such as the hydrogen bond and the covalent bond between two bonded atoms, and the solvent effect, which is caused by the interactions between polymers and solvent molecules, are represented by effective interactions such as Lennard-Jones potential which will be described in the following. In order to improve the computational efficiency, all the monomers are treated as in the same type. Such a coarse-grained polymer is called a homopolymer. Although this model is simple, it is believed that the generic features of structural transitions contained in all types of actual polymers can

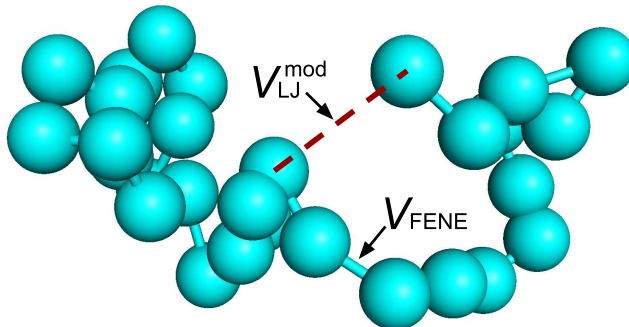


Figure 4.1: A sample conformation of the 30-mer flexible polymer. Bonded monomers are interacted through FENE potential  $V_{\text{FENE}}$  [148–150]. For the non-bonded monomers, the truncated, shifted Lennard-Jones interaction  $V_{\text{LJ}}^{\text{mod}}$  is introduced and utilized in this simulation.

be qualitatively understood through studying such a model [7]. A sample conformation of the coarse-grained flexible homopolymer of length 30 which is utilized in this simulation is shown in Fig. 4.1. The reason why we choose 30- and 55-mer is that the ground state of the 55-mer homopolymer, in which the Lennard-Jones interactions are included in the bond potentials, is a double-layers icosahedron and 30 is an intermediate number between 55 and the other magic number 13 for homopolymers. In the model that we use in this simulation, monomers adjacent in the linear chain are bonded by the anharmonic FENE (finitely extensible nonlinear elastic) potential [148–150]

$$V_{\text{FENE}}(r_{ii+1}) = -\frac{K}{2}R^2 \ln \left[ 1 - \left( \frac{r_{ii+1} - r_0}{R} \right)^2 \right]. \quad (4.1)$$

(Fig 4.2). We set  $r_0 = 1$ , which represents the distance where the FENE potential is minimum,  $R = 3/7$ , and  $K = 98/5$ . Non-bonded monomers interact via a truncated, shifted Lennard-Jones potential

$$V_{\text{LJ}}^{\text{mod}}(r_{ij}) = V_{\text{LJ}}(r_{ij}) - V_{\text{LJ}}(r_c), \quad (4.2)$$

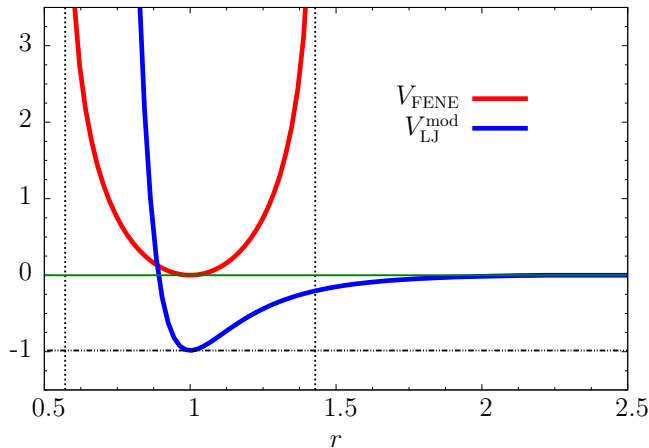


Figure 4.2: FENE and truncated, shifted Lennard-Jones potentials.

with

$$V_{\text{LJ}}(r_{ij}) = 4\epsilon \left[ \left( \frac{\sigma}{r_{ij}} \right)^{12} - \left( \frac{\sigma}{r_{ij}} \right)^6 \right], \quad (4.3)$$

where the energy scale  $\epsilon = 1$ , the length scale  $\sigma = r_0/2^{1/6}$ , and the cut-off radius  $r_c = 2.5\sigma$  (Fig. 4.2). For  $r_{ij} > r_c$ ,  $V_{\text{LJ}}^{\text{mod}}(r_{ij}) \equiv 0$ . The total energy of a conformation  $\zeta = (\vec{r}_1, \dots, \vec{r}_L)$  for a chain with  $L$  monomers reads

$$E(\zeta) = \sum_{i=1}^{L-2} \sum_{j=i+2}^L V_{\text{LJ}}^{\text{mod}}(r_{ij}) + \sum_{i=1}^{L-1} V_{\text{FENE}}(r_{ii+1}). \quad (4.4)$$

## 4.2.2 Simulation Method

In our simulations, we employed the Metropolis Monte Carlo method. In a single MC update, the conformation is changed by a random local displacement of a monomer. Once a monomer is randomly chosen, its position is changed within a small cubic box with edge lengths  $d = 0.3r_0$ . In our simulations, the probability of accepting such an update is given by the Metropolis criterion [37] as in Eq. 3.8. At each temperature, we performed about  $9 \times 10^9$

MCS after extensive equilibration. Shift register random number generator was employed to generate random numbers in this study.

## 4.3 Results

### 4.3.1 Autocorrelation times at constant displacement

For the interpretation of the autocorrelation times of energy, square end-to-end distance, square radius of gyration, and number of contacts, it is helpful to first investigate thermodynamic properties of these quantities. To identify structural transitions in complex systems, the most commonly considered observables are the energy  $E$  and its thermal fluctuation, the heat capacity  $C_V$ . For locating structural transitions in polymer systems, we also measured the squared radius of gyration,

$$R_{\text{gyr}}^2 = \frac{1}{L} \sum_{j=1}^L (\vec{r}_j - \vec{r}_{\text{c.m.}})^2 \quad (4.5)$$

where  $\vec{r}_j$  is the coordinate of monomer  $j$  and  $\vec{r}_{\text{c.m.}}$  is the center of mass given by  $\vec{r}_{\text{c.m.}} = \frac{1}{L} \sum_{j=1}^L \vec{r}_j$ , and the square end-to-end distance defined as

$$R_{\text{ee}}^2 = (\vec{r}_L - \vec{r}_1)^2. \quad (4.6)$$

The corresponding thermal response functions in the canonical ensemble  $d\langle R_{\text{gyr}}^2 \rangle / dT$  and  $d\langle R_{\text{ee}}^2 \rangle / dT$  are particularly helpful for the identification of structural transitions, if  $C_V$  fails to provide a pronounced signal. In addition, the number of contacts  $N_c$  has also been investigated. A contact between two non-bonded monomers is formed if their distance is in the interval  $r_{ij} \in [0.8, 1.2]$  for the 30-mer and  $r_{ij} \in [0.87, 1.13]$  for the 55-mer. The number of contacts is a simple discrete order parameter which is helpful in distinguishing pseudophases.

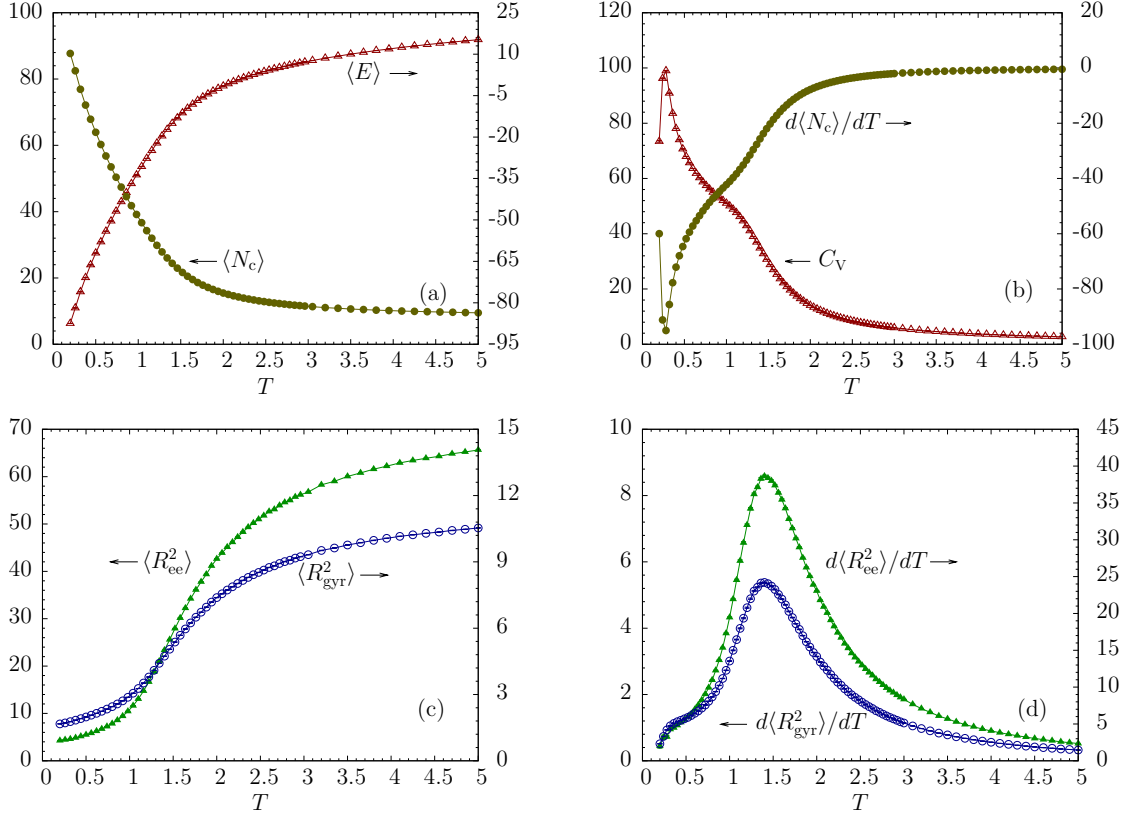


Figure 4.3: Thermodynamic quantities for a flexible polymer with 30 monomers. (a) Mean energy  $\langle E \rangle$  and number of contacts  $\langle N_c \rangle$ ; (b) heat capacity  $C_V$  and thermal fluctuation of the number of contacts  $d\langle N_c \rangle/dT$ ; (c) square end-to-end distance  $\langle R_{ee}^2 \rangle$  and square radius of gyration  $\langle R_{gyr}^2 \rangle$ ; (d) thermal fluctuations of the square end-to-end distance  $d\langle R_{ee}^2 \rangle/dT$  and the square radius of gyration  $d\langle R_{gyr}^2 \rangle/dT$ . Error bars are smaller than the symbol size.

This quantity has proven to be particularly useful in studies of lattice models [107, 108, 151]. In the continuous model used here, it is a robust parameter that does not depend on energetic model details.

We have plotted the mean values of energy and number of contacts in Fig. 4.3(a), as well as the heat capacity and thermal fluctuation of the number of contacts in Fig. 4.3(b). Square end-to-end distance and square radius of gyration curves are shown in Fig. 4.3(c) and their thermal fluctuations in Fig. 4.3(d). The two clear peaks at  $T \approx 1.4$  of the latter

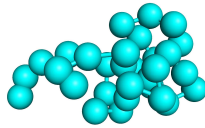
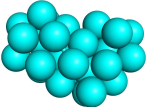
Phase	Conformation
Gas	
Liquid	
Solid	

Figure 4.4: Sample conformations of the 30-mer flexible polymer for the “gas”, “liquid”, and “solid” pseudophases.

represent the collapse transition ( $\theta$  transition) of the 30-mer. Note that the fluctuations of energy and contact number in Fig. 4.3(b) do not exhibit peaks at the transition point, i.e., the temperature that the  $\theta$  transition occurs, but only “shoulders”. As the temperature decreases, dissolved or random coils (gas pseudophase) collapse in a cooperative arrangement of the monomers, and compact globular conformations (liquid pseudophase) are favorably formed (Fig. 4.4). As the temperature decreases further, the polymer transfers from the globular pseudophase to the “solid” pseudophase which is characterized by locally crystalline or amorphous metastable structures (Fig. 4.4). A corresponding peak and valley which mark the liquid-solid (crystallization) or freezing transition of the 30-mer can be observed at  $T \approx 0.28$  in the heat capacity and  $d\langle N_c \rangle/dT$  curves, respectively, in Fig. 4.3(b). These results coincide qualitatively with those of a previous study, where a slightly different model was employed [20, 152]. Due to insufficient Metropolis sampling at low temperatures, we did not include data in the  $T < 0.2$  region.

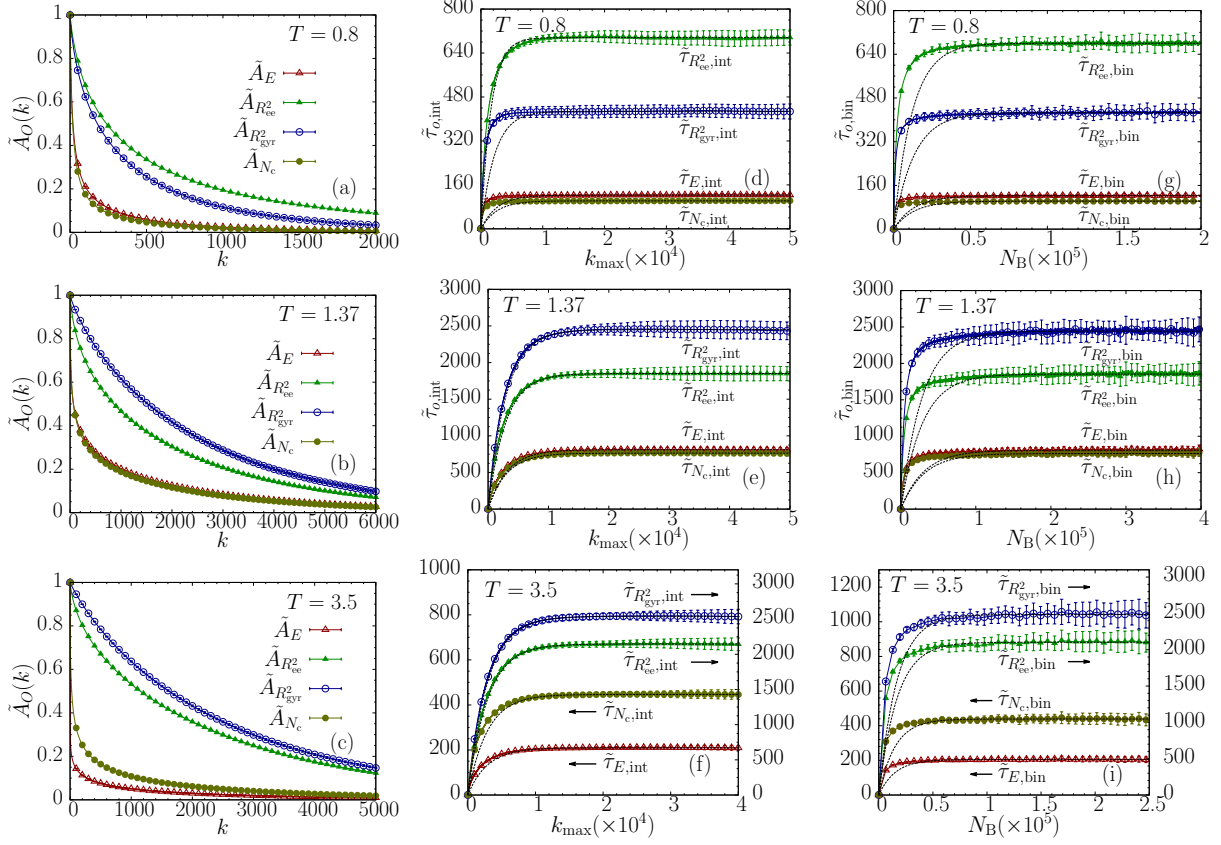


Figure 4.5: (a), (b), and (c) Autocorrelation functions of  $E$ ,  $R_{ee}^2$ ,  $R_{gyr}^2$ , and  $N_c$  at temperatures below, near, and above the collapse transition temperature, respectively, for  $L = 30$ . For each quantity, the estimated integrated autocorrelation time converges to a constant as shown in (d), (e), and (f). The corresponding binning analysis results also show good convergence and are plotted in (g), (h), and (i). Dashed lines represent the fitted curves. Values of the fitted autocorrelation times the curves converge to are listed in Table 4.1.

$T$	$\tilde{\tau}_{E,int}$	$\tilde{\tau}_{E,bin}$	$\tilde{\tau}_{N_c,int}$	$\tilde{\tau}_{N_c,bin}$
0.8	$122 \pm 7$	$122 \pm 13$	$101 \pm 7$	$102 \pm 13$
1.37	$810 \pm 45$	$808 \pm 94$	$763 \pm 39$	$763 \pm 93$
3.5	$209 \pm 13$	$205 \pm 25$	$446 \pm 27$	$438 \pm 52$

$T$	$\tilde{\tau}_{R_{ee}^2,int}$	$\tilde{\tau}_{R_{ee}^2,bin}$	$\tilde{\tau}_{R_{gyr}^2,int}$	$\tilde{\tau}_{R_{gyr}^2,bin}$
0.8	$696 \pm 33$	$680 \pm 75$	$427 \pm 28$	$426 \pm 50$
1.37	$1851 \pm 103$	$1853 \pm 201$	$2450 \pm 138$	$2443 \pm 272$
3.5	$2145 \pm 106$	$2103 \pm 228$	$2539 \pm 121$	$2485 \pm 268$

Table 4.1: Autocorrelation times of  $E$ ,  $R_{ee}^2$ ,  $R_{gyr}^2$ , and  $N_c$  estimated by integration of autocorrelation functions and by using the binning method at three temperatures below, near, and above the collapse transition.

We performed the integration of the autocorrelation (Eq. 2.17) and the binning analysis (Eq. 2.27) to estimate the integrated autocorrelation times at 17 temperatures in the interval  $T \in [0.26, 4.5]$  for the 30-mer and at 16 temperatures in the interval  $T \in [0.3, 5]$  for the 55-mer. Mean values  $\overline{Q}_O(x)$  (where  $\overline{Q}_O(x)$  stands for  $\overline{A}_O(k)$ ,  $\overline{\tau}_{O,\text{bin}}(N_B)$  or  $\overline{\tau}_{O,\text{int}}(k_{\text{max}})$ ) for a quantity  $O$  were calculated at each temperature in  $N_r$  ( $N_r > 20$ ) independent runs:

$$\overline{Q}_O(x) = \frac{1}{N_r} \sum_{i=1}^{N_r} Q_O^i(x), \quad (4.7)$$

where  $Q_O^i(x)$  is the value calculated in the  $i$ th run. As shown in Fig. 4.5, all estimates of autocorrelation functions and times converge for large values of  $k$ ,  $k_{\text{max}}$ , and  $N_B$ , respectively, as expected. The error of  $\overline{Q}_O(x)$  is estimated by

$$\epsilon_{\overline{Q}_O(x)}^2 = \frac{1}{N_r - 1} \sum_{i=1}^{N_r} \left( Q_O^i(x) - \overline{Q}_O(x) \right)^2, \quad (4.8)$$

because all runs were performed independently of each other. The consistency of the two different methods used for the estimation of autocorrelation times for the investigated quantities becomes apparent from Table 4.1, where we have listed the autocorrelation time estimate for three temperatures below, near, and above the  $\Theta$  point. The results coincide within the numerical error bars.

In order to estimate the integrated autocorrelation time systematically, we performed least-squares fitting for all the curves in both the integration method of the autocorrelation function and binning analysis at each temperature. The empirical fit function for any quantity  $O$  is chosen to be of the form

$$f_O(x) = \tau_O^f (1 - e^{-x/x^f}), \quad (4.9)$$

where  $x$  represents  $k_{\text{max}}$  in the integration of the autocorrelation functions method and  $N_B$

in binning analysis;  $\tau_O^f$  and  $x^f$  are two fit parameters. The fitting curves, also plotted in Fig. 4.5, coincide well with the mean values of the integrated autocorrelation times in the  $N_B/k_{\max}$  region where convergence sets in.

It is necessary to mention that when using the binning method to calculate error bars one needs to ensure that the binning block length is much larger than the autocorrelation time. The reason is obvious from Fig. 4.5. If the autocorrelation time estimated by the binning method has not yet converged, the estimate  $\tilde{\tau}_{O,\text{bin}}$  is less than the integrated autocorrelation time ( $\tilde{\tau}_{O,\text{bin}} < \tau_{O,\text{int}}$ ). Therefore, the estimated standard deviation

$$\epsilon_O^2 = \frac{\tilde{\sigma}_{O^B,c}^2}{K} = \frac{2\tilde{\sigma}_O^2}{N} \tilde{\tau}_{O,\text{bin}} \quad (4.10)$$

underestimates the true value  $\epsilon_O^2 = 2\sigma_O^2\tau_{O,\text{int}}/N$  in this case, yielding a too small error estimate.

After the preliminary considerations, we will now discuss how the dependence of the autocorrelation time on the temperature can be utilized for the identification of structural transitions in the polymer system.

### 4.3.2 Slowing down at the $\Theta$ point

Figure 4.6 shows how the fitted estimated integrated autocorrelation times  $\tau_O^f$  vary with temperature. As the comparison shows, the autocorrelation times estimated by using the binning analysis are in very good agreement with the results obtained by integrating autocorrelation functions.

The integrated autocorrelation time curves of  $R_{\text{ee}}^2$  and  $R_{\text{gyr}}^2$  behave similarly at most of the temperatures except the temperatures close to the freezing transition. This is not surprising as both are structural quantities that are defined to describe the compactness of the polymer. In addition, the integrated autocorrelation time curves of  $E$  and  $N_c$  behave

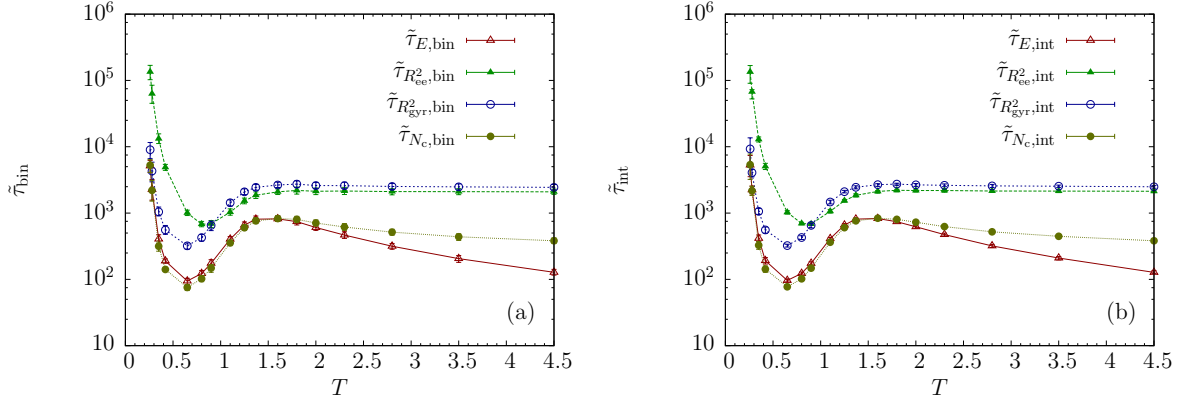


Figure 4.6: Temperature dependence of integrated autocorrelation times (a) estimated with the binning method; (b) obtained by the integration of autocorrelation functions for the 30-mer.

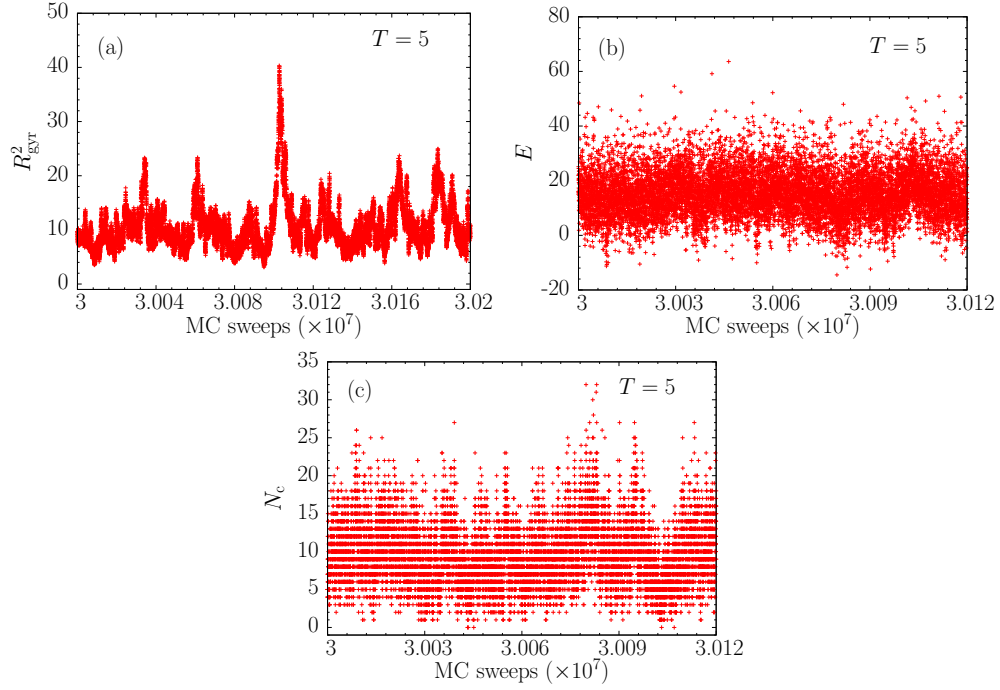


Figure 4.7: (a), (b), and (c) are parts of the time series of  $R_{\text{gyr}}^2$ ,  $E$ , and  $N_c$  at  $T = 5$  in equilibrium for the 30-mer.

similarly. Their relation can be understood as following. The polymer conformation in the solid pseudophase is characterized by locally crystalline or amorphous metastable structures. Therefore, the main contribution of each monomer to the energy in this pseudophase originates from the interaction between this monomer and its non-bonded nearest neighbors. This is also reflected by the number of contacts to the nearest neighbors. Thus,  $E \propto N_c$  in the solid pseudophase. This can be seen in Fig. 4.3(a), in which, for example,  $E \approx -88$  and  $N_c \approx 88$  at  $T = 0.2$ . The autocorrelation times of the two structural quantities are always larger than the ones of  $E$  and  $N_c$ . The reason is that the structural quantities are not particularly sensitive to conformational changes within a single pseudophase. Furthermore, the displacement update used here does not allow for immediate substantial changes. This can be seen in Fig. 4.7(a) where the time series are shown at high temperature. From Fig. 4.7(b) and 4.7(c), one notices that  $E$  and  $N_c$  fluctuate more rapidly than  $R_{\text{gyr}}^2$ .

The most important observation from Fig. 4.6 is that slowing down, which is indicated by the extremal values in the autocorrelation time curves and implies that the Metropolis algorithm “slows down” because of increased correlations in the configurations generated, appears near  $T \approx 1.4$  indicating the occurrence of the collapse transition. This temperature is close to the peak positions of the structural fluctuations shown in Fig. 4.3(d).

Near the freezing transition ( $T \approx 0.3$ ), the autocorrelation times of all four quantities rapidly increase. Since Metropolis simulations with local updates typically get stuck in metastable states of the polymer at low temperatures, we do not estimate autocorrelation times in the  $T < 0.26$  region. The freezing transition is, therefore, virtually inaccessible to any autocorrelation time analysis based on local-update Metropolis simulations. This is amplified by the fact that the autocorrelation time increases naturally at low temperatures, because of the low entropy. That means if there would be a signal of the freezing transition at all in the autocorrelation time curves, it would be difficult to identify it.

The autocorrelation times of  $R_{\text{cc}}^2$ ,  $R_{\text{gyr}}^2$ , and  $N_c$  seem to converge to constant values at high

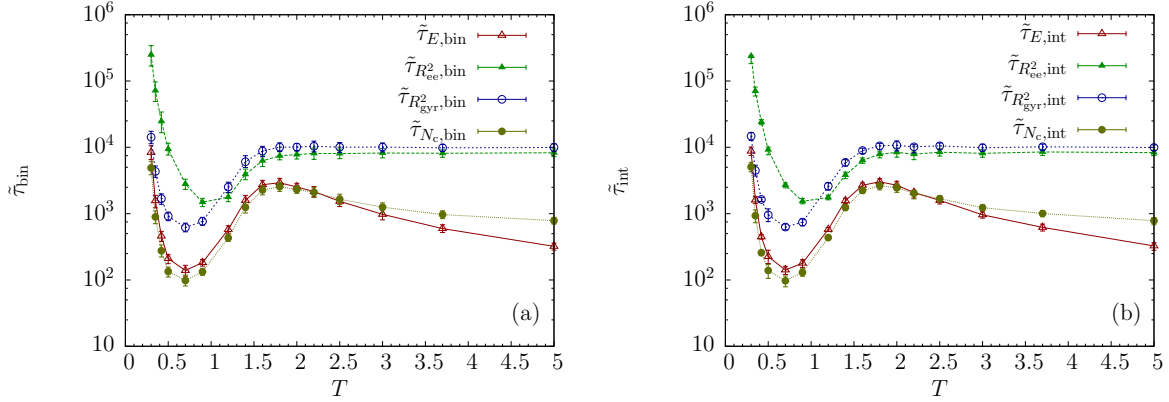


Figure 4.8: Same as Fig. 4.6, but for the 55-mer.

temperatures, whereas the autocorrelation time of  $E$  decays. This is partly due to the fact that the structural quantities and  $N_c$  possess upper limiting values that are reached at high temperatures, thereby reducing the fluctuation width at constant displacement range. This is a particular feature of the results obtained in simulations with fixed maximum displacement and it is different if the acceptance rate is kept constant instead. This will be discussed in Sec. 4.3.3.

The overall behavior is similar to Metropolis dynamics for the two-dimensional Ising model on the square lattice, in which the external field is excluded so that  $E \in [-2JL^2, 2JL^2]$  where  $J > 0$  is the coupling constant and  $L$  is the lattice size and the magnetization  $M \in [-L^2, L^2]$  [30].

In order to verify that the general autocorrelation properties apply also to larger polymers, we repeated the simulations for a 55-mer. From Fig. 4.8, we notice that the behavior is qualitatively the same, but the autocorrelation times of all quantities are larger than the ones for the 30-mer, as expected. This supports our hypothesis that the qualitative behavior of the autocorrelation times of the 30-mer is generic and representative for autocorrelation properties of larger polymers. In particular, this method offers a possible way for the iden-

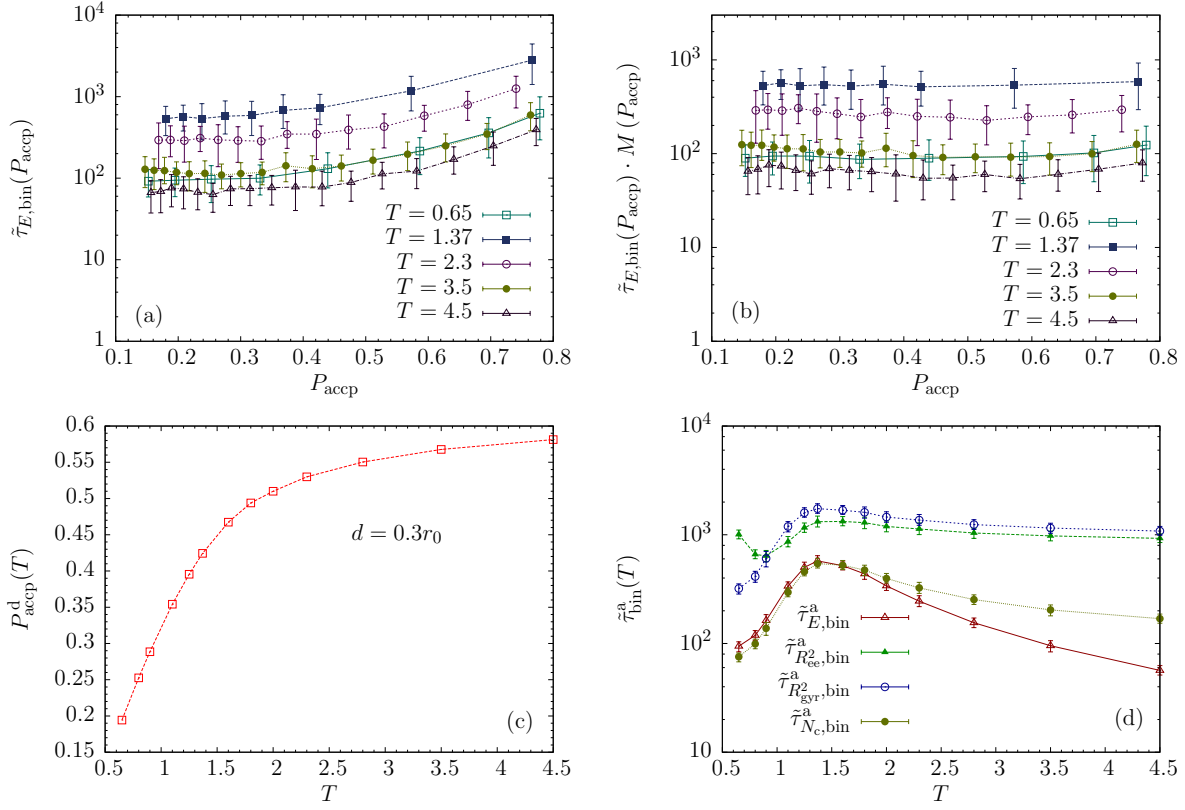


Figure 4.9: (a) Integrated autocorrelation times of the energy  $\tilde{\tau}_{E,\text{bin}}$  at different acceptance rates  $P_{\text{accp}}$  for various temperatures near the collapse transition of the 30-mer; (b) modified autocorrelation times of energy versus acceptance rates; (c) acceptance rates at fixed maximum displacement  $d = 0.3r_0$  for different temperatures; (d) integrated autocorrelation times at fixed acceptance rate  $P_{\text{accp}}^a = 0.2$  as a function of temperature for the 30-mer.

tification of transitions, where standard canonical analysis of quantities such as the specific heat fails.

### 4.3.3 Autocorrelation times at a fixed acceptance rate

In order to find out how the autocorrelation times of different quantities change at a fixed acceptance rate rather than at a fixed maximum displacement range, i.e., the displacement box length, the first step of the intuitive method is to adjust the displacement box length

at each temperature, as discussed in Sec. 3.6, so that the expected acceptance rate can be reached. Then, the simulation can be conducted to calculate the integrated autocorrelation times of different quantities with the adjusted displacement box length yielding the expected acceptance rate at each temperature. However, since autocorrelation time calculation is very time consuming, instead of using the intuitive method, we directly generated the autocorrelation times at a fixed acceptance rate from the ones at a fixed maximum displacement range by employing the following approach. To begin with, we used the binning method to calculate the integrated autocorrelation times at different constant acceptance rates  $P_{\text{accp}}$  for different temperatures near the collapse transition for the 30-mer. The results for the energetic autocorrelation times  $\tilde{\tau}_{E,\text{bin}}(P_{\text{accp}})$  are shown in Fig. 4.9(a), measured for five different temperatures. Autocorrelation times of the other quantities exhibit a similar behavior. Two important conclusions can be drawn: (i) the values of the autocorrelation times depend on acceptance rate and temperature, but (ii) the monotonic behavior of  $\tilde{\tau}_{E,\text{bin}}$  as a function of  $P_{\text{accp}}$  is virtually independent of the temperature. Thus, if multiplied by a temperature-independent empirical modification factor

$$M(P_{\text{accp}}) = e^{-4|P_{\text{accp}}-0.2|^{1.65}}, \quad (4.11)$$

the modified autocorrelation time curves become almost independent of  $P_{\text{accp}}$  at these temperatures (see Fig. 4.9(b)):

$$\tilde{\tau}_{\text{bin}}(P_{\text{accp}}) \cdot M(P_{\text{accp}}) \approx \text{const.} \quad (4.12)$$

in the interval  $P_{\text{accp}} \in (0.14, 0.78)$ . This feature of uniformity in monotonic behavior and the empirical modification factor in Eq. 4.11 can then be used to modify the autocorrelation times at all temperatures. For this purpose one reads the autocorrelation time  $\tilde{\tau}_{\text{bin}}^{\text{d}}(T)$  and the acceptance rate  $P_{\text{accp}}^{\text{d}}(T)$  at fixed maximum displacement at a given temperature  $T$  from

Fig. 4.6(a) and Fig. 4.9(c), respectively, calculates the modification factor  $M(P_{\text{accp}}^{\text{d}}(T))$  from Eq. 4.11, and obtains the modified autocorrelation time  $\tilde{\tau}_{\text{bin}}^{\text{a}}$  at constant acceptance rate  $P_{\text{accp}}^{\text{a}}$  by making use of Eq. 4.12. For simplicity, we choose  $P_{\text{accp}}^{\text{a}} = 0.2$ , which yields

$$\tilde{\tau}_{\text{bin}}^{\text{a}}(T) = \tilde{\tau}_{\text{bin}}^{\text{d}}(T) \cdot M(P_{\text{accp}}^{\text{d}}(T)), \quad (4.13)$$

since  $M(0.2) = 1$ . The temperature dependence of this modified autocorrelation time is shown in Fig. 4.9(d). One notices that the peaks indicating the collapse transition are more pronounced than the ones in the fixed maximum displacement case, but qualitatively (and quantitatively regarding the  $\Theta$  transition point) this modified approach leads to similar results. In the temperature range investigated here, the autocorrelation times of all quantities seem to decrease above the  $\Theta$  point. This is different than the behavior at fixed maximum displacement range (cp. Fig. 4.6(a)).

## 4.4 Conclusions

Employing the Metropolis Monte Carlo algorithm, we have performed computer simulations of a simple coarse-grained model for flexible, elastic polymers to investigate the autocorrelation time properties for different quantities. Two different methods were employed to estimate autocorrelation times as functions of temperatures for polymers with 30 and 55 monomers: by integration of autocorrelation functions and by using the binning method. The results obtained for different energetic and structural quantities by averaging over more than 20 independent simulations are consistent.

The major result of our study is that autocorrelation time changes can be used to locate structural transitions of polymers, because of algorithmic slowing down. We deliberately employed Metropolis sampling and local displacement updates, as slowing down is partic-

ularly apparent in this case. We could clearly identify the collapse transition point for the two chain lengths investigated. Low-temperature transitions are not accessible because of the limitations of Metropolis sampling in low-entropy regions of the state space.

The identification of transitions by means of autocorrelation time analysis is, therefore, an alternative and simple method to more advanced techniques such as microcanonical analysis [7, 8, 10, 20, 23, 153] or by investigating partition function zeros [1–6]. Those methods require the precise estimation of the density of states of the system which can only be achieved in sophisticated generalized-ensemble simulations. The autocorrelation time analysis method is very robust and can be used as an alternative method for the quantitative estimation of transition temperatures, in particular, if the more qualitative standard canonical analysis of “peaks” and “shoulders” in fluctuating quantities remains inconclusive.

# Chapter 5

## Lattice polymer adsorption

### 5.1 Introduction

Interfaces of organic and inorganic matter such as hybrid polymer-substrate systems have been thoroughly investigated in recent years. Models used in computational studies cover all scales and range from coarse-grained to atomistic, depending on the specificity of the questions involved. A major problem is the understanding of structural transitions that accompany a polymer adsorption process at a substrate. There is a variety of structural pseudophases and transition pathways that depend on external and internal system parameters. Internally, competing energy and length scales associated with the interactions of monomers with other elements of the chain and the substrate affect the transition processes. External conditions are governed, e.g., by thermodynamic control parameters such as pressure or temperature, but also the solvent quality. By considering the competition between surface attraction and monomer-monomer attraction through varying the corresponding attractive strengths, computational studies on adsorption of lattice [107–116] and off-lattice [117–119] polymers and proteins at homogeneous, flat substrates have been widely investigated. The influence of different geometric attractive substrates on the formation of polymer structures

has been explored by studying polymer adsorption at cylindrical [120, 121] and fluctuating membrane-like surfaces [122], at nanowires [123–125], and in spherical cavities [126]. How polymers and proteins identify the patterns of surfaces and substrates is also an important subject triggering many computational studies [127–130].

In this chapter, we will investigate the effects of the temperature and a solvent quality parameter on the behaviors of a lattice polymer adsorbed at a solid substrate. The pseudophase diagram of polymer adsorption will be constructed based on the generalized microcanonical inflection-point analysis [8, 20, 23].

## 5.2 Model and simulation method

### 5.2.1 Model

The model we employ here is a grafted simple-cubic (sc) lattice polymer model with one end anchored at a flat adhesive surface. The length of the polymer is  $L = 503$  which is the largest prime number that we can simulate (Fig. 5.1). The energy of the system could be expressed as

$$E(n_s, n_m) = -n_s - sn_m, \quad (5.1)$$

where the number of nearest-neighbor, but nonadjacent monomer-monomer contacts is denoted by  $n_m$  and the number of nearest-neighbor monomer-substrate contacts is signified by  $n_s$ . As shown in Fig. 5.1, if the distance between two nonadjacent monomers is equal to one lattice size, i.e.,  $r_m = 1$ , the two monomers are considered to be in contact with each other. Similarly, monomers located above the substrate with monomer-substrate distances equal to one lattice size, i.e.,  $r_s = 1$ , are defined to be in contact with the substrate.  $n_m$  and  $n_s$  count the numbers of such contacts. By introducing the dimensionless reciprocal solubility  $s$ , the quality of the implicit solvent can be controlled in the simulation [108]. In order to lower the

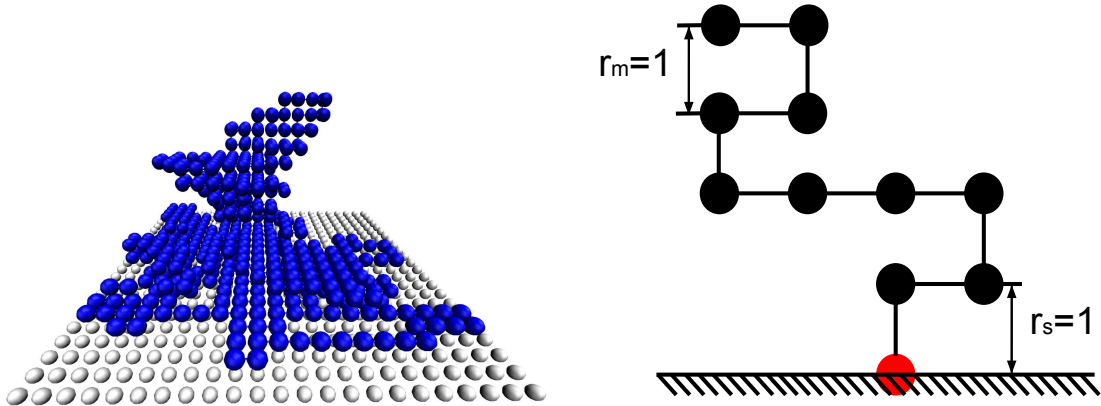


Figure 5.1: A sample conformation of the grafted simple-cubic (sc) lattice homopolymer of length 503 (left). A sketch of this model illustrating the number of nearest-neighbor, but nonadjacent monomer-monomer contacts  $n_m$  and number of nearest-neighbor monomer-substrate contacts  $n_s$  (right).

system energy, the polymer will always judge either to form more surface-monomer contacts or monomer-monomer contacts according to the value of  $s$ . If  $s < 1$ , more surface-monomer contacts will be formed and vice versa.

## 5.2.2 Simulation method

In this chapter, we employ the contact-density chain-growth algorithm [155] which is an improved variant of the recently developed multicanonical chain-growth sampling method [95, 96, 154]. All these methods are based on a variant of the pruned-enriched version [91] of Rosenbluth sampling [90]. With this method, we directly sample the contact density  $g_{n_s n_m}$ . Because this allows us to conveniently calculate the density of states  $g(E, s)$  with Eq. 5.1 after the simulation by using the reciprocal solubility  $s$ . The process to estimate  $g_{n_s n_m}$  is similar to the estimation of density of states introduced in Sec. 3.8 with the only change of

the multicanonical chain-growth weights

$$W_{n,\alpha_j}^{\text{ss,is}} = W_{n-1}^{\text{ss,is}} \frac{m_n}{k \binom{m_n}{k} P_A} \frac{W_n^{\text{flat,(i)}}(n_s^{(n,\alpha_j)}, n_m^{(n,\alpha_j)})}{W_{n-1}^{\text{flat,(i)}}(n_s^{(n-1)}, n_m^{(n-1)})}, \quad (5.2)$$

where the multi-contact weights  $W_n^{\text{flat,(i)}}(n_s^{(n,\alpha_j)}, n_m^{(n,\alpha_j)}) \sim 1/g_{n_m^{(n,\alpha_j)} n_s^{(n,\alpha_j)}}$  need to be determined recursively [7]. In this simulation, we used MARSAGLIA pseudo random number generator.

## 5.3 Results

### 5.3.1 Microcanonical inflection-point analysis

By applying the microcanonical inflection-point analysis to the grafted lattice polymer model, we obtained all the pseudophase transitions for different  $s$  values varying from 0 to 2. Note that, in this simulation, we calculate all the derivatives of entropy directly from  $S(E)$  by utilizing an eleven-points stencil method. In order to reduce the noise due to fluctuation, we employ Bézier smoothing onto every derivative of  $S(E)$  [7, 97, 98]. And then we use the smoothed curves to do microcanonical inflection-point analysis. Fig. 5.2(a) shows examples of the first- and second-order pseudophase transitions. In this graph, a first-order pseudophase transition occurs at  $E \approx -830$  around which the backbending behavior appears in the  $\beta(E)$  curve. And a corresponding positive peak is observed in the  $\gamma(E)$  curve at the same location. In the meantime, a second-order pseudophase transition signal is observed at  $E \approx -767$  where the  $\beta(E)$  curve behaves least sensitively and forms an inflection point. The corresponding negative peak in the  $\gamma(E)$  curve also helps locate the pseudophase transition energy. A third-order pseudophase transition is shown in Fig. 5.2(b). In this graph, a least sensitive inflection point can be recognized at  $E \approx -613$  in the  $\gamma(E)$  curve and a corresponding positive valley, i.e., a local minimum, is found in the  $\delta(E)$  curve. Fig. 5.2(c)

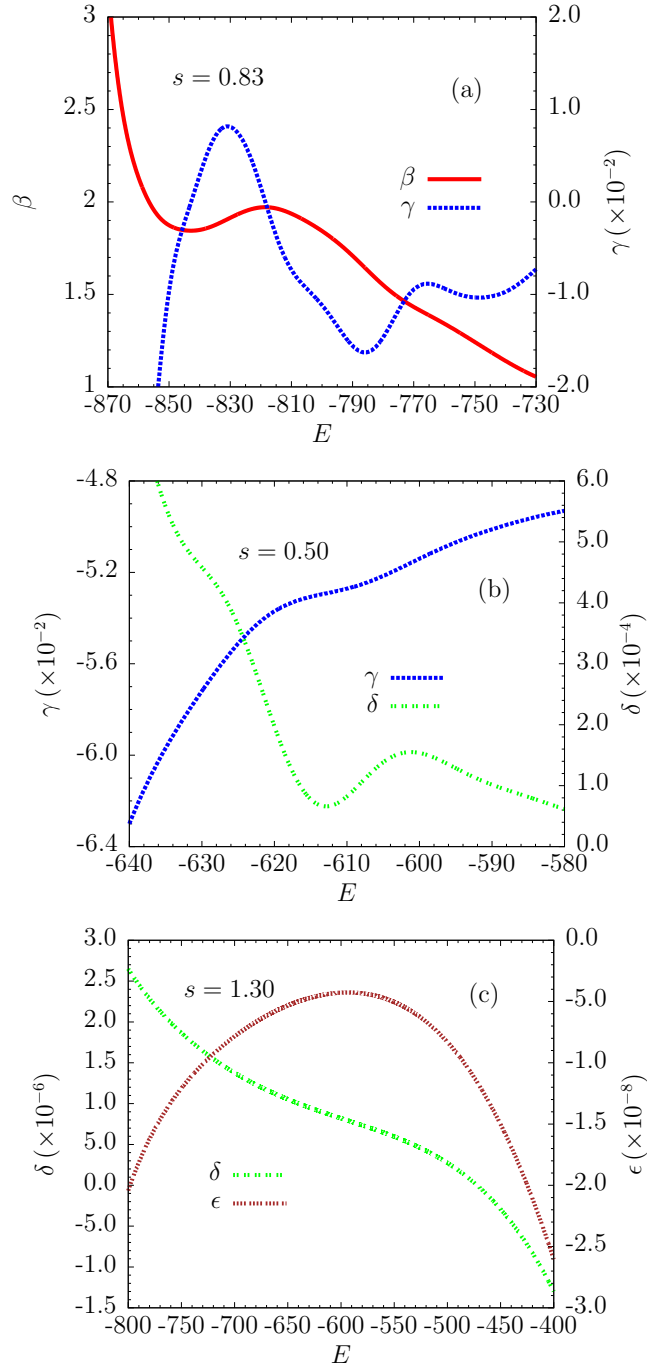


Figure 5.2: Examples of the application of the microcanonical inflection-point analysis method to a grafted lattice polymer model. (a) First- and second-order pseudophase transitions occur at  $E \approx -830$  and  $-767$  for  $s = 0.83$ . (b) A third-order pseudophase transition can be identified at  $E \approx -613$  for  $s = 0.50$ . Signals in (c) indicate the existence of a fourth-order pseudophase transition appearing at  $E \approx -590$  for  $s = 1.30$ .

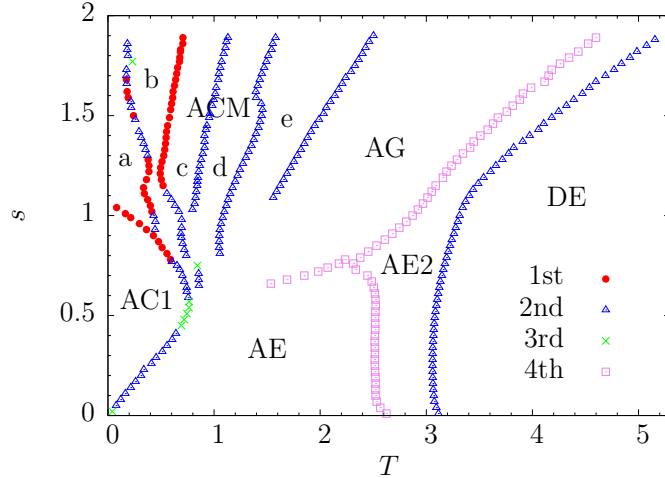


Figure 5.3: Microcanonical pseudophase diagram for the homogeneous lattice polymer grafted to an adhesive surface.

presents an example of the fourth-order pseudophase transition. The pseudophase transition appears at  $E \approx -590$  in the  $\delta(E)$  curve and forms a least sensitive inflection point. A negative peak in the  $\epsilon(E)$  curve at the same location further proves that this pseudophase transition is of fourth order.

### 5.3.2 Structural Pseudophase Diagram

A pseudophase diagram based on microcanonical inflection-point analysis is constructed in Fig. 5.3. Since microcanonical temperature  $T(E) = \beta(E)^{-1}$  has one-to-one correspondence with energy and the information of the system is all contained in the density of states  $g(E)$ , in order to recognize what pseudophase one region belongs to, one can choose several points in this region and find their corresponding energies. After that, one can continue to check numerous configurations of these energies. The type of pseudophase that this region belongs to is determined by the majority of these configurations. Fig. 5.4 lists the typical configuration of each pseudophase.

Since parameter  $s$  controls the competition between monomer-monomer attraction and surface adsorption, a  $s < 1$  value entails the polymer prefer to be adsorbed by the surface. When the temperature is low, polymer is not only fully adsorbed but also well compact due to small thermal fluctuation. The typical conformation of polymer in the pseudophase AC1 is an one layer well compact solid structure as shown in Fig. 5.4.

In the low  $T$  region, as  $s$  increases, more monomer-monomer contacts are preferred. The system will undergo a solid-solid pseudophase transition and more than two layers structures will be formed. This pseudophase transition is of first-order for  $T < 0.6$  and turns into second-order as  $T$  increases (see Fig. 5.3). For example, for  $s = 0.83$ , one can observe the backbending behavior in the  $\beta(E)$  curve around  $E \approx -830$  and a corresponding positive peak in the  $\gamma(E)$  curve in Fig. 5.2(a). These signals indicate a first-order pseudophase transition occurs at  $T = 1/\beta \approx 0.52$ . In the adsorbed, compact, multiple layers pseudophase (ACM), the compactness of the structures will gradually decrease when the system's temperature raises. The label "a" to "e" in the pseudophase diagram shows the change of this trend. Here "a" means the structures are the most compact, whereas "e" means the compactness is the least. The change of this trend could be observed from the structures in Fig. 5.4. The order of the transitions are mostly second. For instance, a second-order pseudophase transition shows up at  $E \approx -767$  for  $s = 0.83$  in the Fig. 5.2(a). A least sensitive inflection point in the  $\beta(E)$  curve and a negative peak in the  $\gamma(E)$  curve indicate that this pseudophase transition occur at  $T \approx 0.71$ . However, some parts of the pseudophase transitions among ACMa, ACMb, and ACMc are of first order.

As temperature continues raising, the system will become less compact. In the small  $s$  value region, the adsorbed one layer polymer will greatly expand but keeps adsorbed on the surface. The adsorbed, expanded pseudophase AE will be formed. The order of the pseudophase transitions between AC1 and AE is either of second order or third order. For example, a third-order pseudophase transition occurring at  $T \approx 0.75$  for  $s = 0.50$  can be

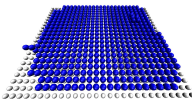
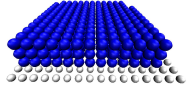
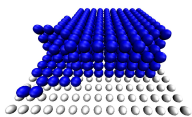
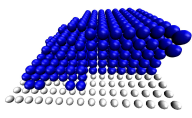
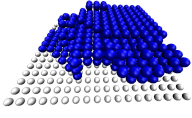
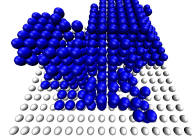
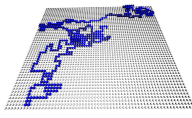
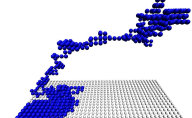
Phase	Configuration	$n_s$	$n_m$
AC1		496	456
ACMa		171	756
ACMb		142	764
ACMc		131	752
ACMd		137	705
ACMe		130	668
AG		226	394
AE		444	217
AE2		89	389
DE		62	147

Figure 5.4: Examples of typical conformations in the different structural pseudophases for homogeneous lattice polymer grafted to an adhesive surface. (see Fig. 5.3)

identified from the least sensitive inflection point in the  $\gamma(E)$  curve and the positive valley in the  $\delta(E)$  curve at  $E \approx -613$  in Fig. 5.2(b). In the mean time, the structures in the large  $s$  value region will undergo a second-order pseudophase transition and turn into globular. The AG pseudophase will be formed. In addition, if one makes the system less dissolvable, the expanded structures in AE pseudophase will form more monomer-monomer contacts and become globular. The pseudophase transition between AE and AG pseudophases is of fourth order as exhibited in Fig. 5.3.

As temperature further increases, the system will enter the partially adsorbed and expanded pseudophase as labeled AE2 in Fig. 5.3. In this pseudophase, the major property of the polymer is partially adsorbed on the surface and partially desorbed forming the fully expanded structure in the free space. The typical configuration is shown in Fig. 5.4. This pseudophase is the prelude of the fully desorbed pseudophase. The pseudophase transition between the fully adsorbed pseudophase (AE or AG) and partially adsorbed pseudophase (AE2) is of fourth order. An example of this transition shows up in Fig. 5.2(c), where a least sensitive inflection point in  $\delta(E)$  curve and a negative peak in  $\epsilon(E)$  curve are observed at  $E \approx -590$  for  $s = 1.30$ . By reading the corresponding  $\beta$  value, one can calculate the transition temperature locating at  $T \approx 3.3$ .

Ultimately, the polymer will become desorbed from the surface and fully expanded in free space if the system is at high temperature. The corresponding pseudophase is desorbed and expanded pseudophase as labeled DE in Fig. 5.3. The pseudophase transition between AE2 and DE is of second order.

### 5.3.3 Bin Size Effect

During data analysis, one has to group the energies into different energy bins. The choice of the bin size will affect the information of the pseudophase diagram. Since the model we investigated is a discrete model, the bin size effect is more substantial. In order to avoid

too much detail of pseudophase diagram information and remove the information due to fluctuations, we constructed the pseudophase diagram Fig. 5.3 by employing the information from different pseudophase diagrams with different bin sizes.

Fig. 5.5(a) demonstrates the pseudophase diagram with bin size  $dE = 0.80$ . Comparing with Fig. 5.3, one can notice that the information in the low temperature region is clear and similar except the noise due to fluctuation. For the adsorption transition (transition between AE2 pseudophase and DE pseudophase), the pseudophase transition line has the same shape and order as the one in Fig. 5.3 but less smooth. In the AE and AG pseudophase, instead of showing clear transition boundary for AE and AG pseudophase as showed in Fig. 5.3, the pseudophase diagram in Fig. 5.5(a) exhibits the process of the changes from AE/AG pseudophase to DE pseudophase. These changes are reflected as the third-order and fourth-order pseudophase transition lines. For example, by checking a tremendous number of configurations in the AE pseudophase with  $s < 1$  in Fig. 5.5(a), one can notice that polymer gradually becomes desorbed from the surface as temperature increases until finally fully desorbed and enters the DE pseudophase. For the AG pseudophase, since the polymer is globular, these third-order and fourth-order pseudophase transition lines reflect how the polymer gradually expands and becomes less adsorbed at the same time. At the end, the globule will finally become a completely expanded structure in free space.

However, as the bin size becomes larger, i.e.,  $dE = 5.00$ , the first- and second-order pseudophase transitions in the low temperature region in Fig. 5.5(a) become third- and fourth-order. At the same time, the fluctuation in Fig. 5.5(a) vanishes in Fig. 5.5(b). These changes are all due to the increase of the bin size. Because the detailed information in the small bin case will be averaged out when bin size becomes larger. This causes the convex intruder in the microcanonical entropy and inflection points in the derivatives of entropy to become less substantial. Ultimately, the previous lower-order pseudophase transitions become higher-order. On the other hand, the adsorption transition is stable and becomes

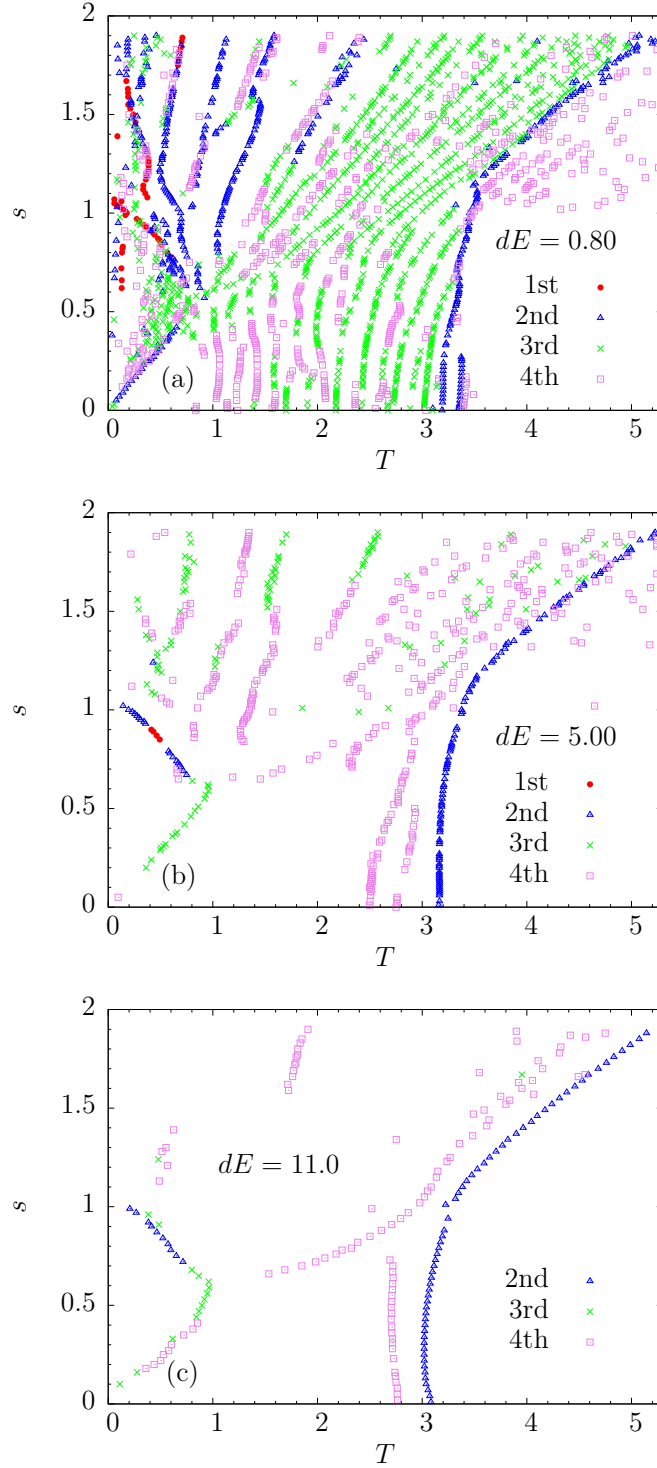


Figure 5.5: (a), (b), and (c) are microcanonical pseudophase diagrams for bin size  $dE = 0.80, 5.00,$  and  $11.0,$  respectively. Note that some of the differences between these pseudophase diagrams and Fig. 5.3 are due to the different plotting scheme.

even more smooth. The pseudophase transition lines in AE and AG pseudophases vanish and a transition boundary separating AE and AG pseudophases gradually appears. In addition, the separating line between AE/AG and AE2 pseudophases begins to form. These changes are all due to the average effects when one increases the bin size. The detailed information about the change from adsorption to desorption has been averaged out and is mainly embodied in the pseudophase transition line between AE/AG and AE2 pseudophases. Whereas, the information about the compactness of the structures becomes more substantial and leads to the formation of the separating boundary between AG and AE pseudophases.

When the bin size becomes very large, i.e.,  $dE = 11.0$ , the information about the pseudophase transition details has disappeared, only pseudophase transition lines separating the major pseudophases remain. Note that the boundary line of the AC1 pseudophase and the adsorption transition line is still stable. This further supports that these transitions are real physical transitions. In the meanwhile, the AE and AG separation line and the AE/AG and AE2 pseudophase transition line all become more substantial and stable.

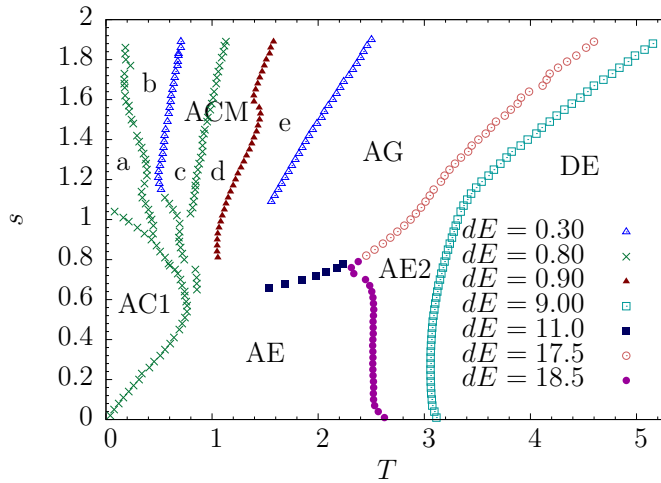


Figure 5.6: Microcanonical pseudophase diagram with the information of the origins of different pseudophase transition lines.

Finally, we construct the pseudophase diagram in Fig. 5.3 by combining the information

from the pseudophase diagrams with different bin sizes. The information about the origin of each pseudophase transition line is summarized in Fig. 5.6. In short, for the pseudophase transitions in low temperatures, we chose the data from small bin sizes like  $dE = 0.30, 0.80,$  and  $0.90$  in order to keep the information about the process of how the compactness gradually changes as temperature increases. For the higher temperature regions, we only chose the large bin size data like  $dE = 9.00, 11.0, 17.5,$  and  $18.5$  to avoid too many redundant details.

## 5.4 Conclusions

In this chapter, for the purpose of testing and exhibiting the power of the microcanonical inflection-point analysis, we simulated a grafted simple-cubic lattice polymer model with one end anchored at a flat adhesive surface by employing a contact-density chain growth algorithm. The pseudophase diagram of adsorption for a polymer with 503 monomers, parameterized by temperature and solvent quality, is constructed solely based on microcanonical inflection-point analysis. The order of the “transition lines” varies from first-order to fourth-order. In addition, the effect of bin size on the determination of structural transitions of the lattice polymer model has also been investigated. We demonstrated that small bin size is needed to be employed in order to distinguish the various solid state structures in the low temperature region. For the pseudophase transitions at high temperatures, it is necessary to utilize large bin size so that the redundant information about the details of transitions and fluctuations can be avoided. This study confirms the general potential of microcanonical statistical analysis for studies of pseudophase transitions for systems of finite size.

# Chapter 6

## Flexible polymer with controlled bonds

### 6.1 Introduction

During the past decades, basic polymer research has focused on the impact of intrinsic parameters on the formation of structural phases. This approach enabled, for example, the study of the conformational behavior of polymer classes from flexible to stiff by varying temperature and bending stiffness [156] and revealed the diversity of structural phases ranging from the well-studied limit of flexible polymers to that of wormlike chains [157]. By changing the interaction range between non-bonded monomers, structural phases of flexible polymers have been investigated as well [15, 16, 69]. It has been found that the liquid phase disappears for shorter interaction ranges and the collapse transition line eventually merges with the freezing transition line. In addition, the influence of bond confinement upon the structural phases and the transition behavior of a flexible chain of bonded beads has also been examined recently [158]. This work shows that the liquid pseudophase disappears with increasing bonded interaction range and finally the gas-liquid and the liquid-solid pseu-

dophase transition lines merge. The systematic investigation of semiflexible elastic polymers with self-interaction under the influence of torsion barriers allowed for the exploration of helical pseudophases and their stability in the presence of bending restraints [159].

However, the influence of properties of the bonded potential between monomers adjacent along the chain on structural phases of the polymer has not yet been thoroughly addressed. In this chapter, we study the effects of bonded interactions on the structural phase properties of a flexible, elastic homopolymer by adjusting the Lennard-Jones interaction strength between bonded monomers through a width and asymmetry parameter in the bonded potential. The state space was sampled by performing parallel tempering simulations [73–76], supported by a parallel version of multicanonical sampling [7, 52, 79, 80, 84]. As the major result, the microcanonical pseudophase diagram parameterized by the microcanonical temperature and the bond potential parameter is constructed. In order to illustrate the diverse structures in the low-temperature region, a systematic structural analysis has also been employed.

## 6.2 Model and simulation methods

### 6.2.1 Model

In this study, we systematically investigate the influence of the shape and effective range of the potential between bonded monomers in a generic model of self-interacting flexible elastic homopolymers of lengths 15 and 55 (Fig. 6.1). The interaction between non-bonded beads of the polymer is based on a standard 12-6 Lennard-Jones (LJ) potential,

$$U_{\text{LJ}}(r) = 4\epsilon \left[ \left( \frac{\sigma}{r} \right)^{12} - \left( \frac{\sigma}{r} \right)^6 \right], \quad (6.1)$$

where  $\sigma$  is the van-der-Waals radius and  $r$  is the monomer-monomer distance. For computational efficiency, the non-bonded potential is truncated at  $r_c = 2.5\sigma$  and shifted by the

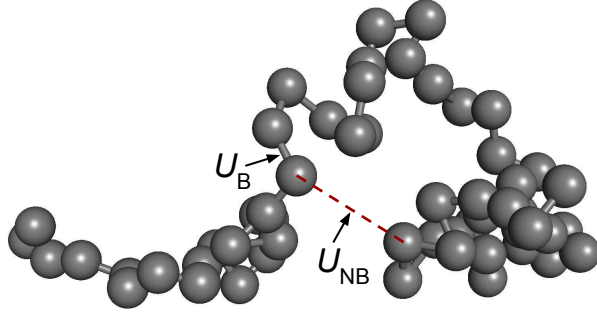


Figure 6.1: A sample conformation of the 55-mer flexible polymer model with modified bonded potential.

constant  $U_{\text{shift}} = U_{\text{LJ}}(r_c)$  to avoid a discontinuity of the potential at  $r = r_c$ ,

$$U_{\text{NB}}(r) = \begin{cases} U_{\text{LJ}}(r) - U_{\text{shift}}, & r < r_c, \\ 0, & \text{otherwise.} \end{cases} \quad (6.2)$$

The minimum of the potential is located at  $r_0 = 2^{1/6}\sigma$ , which fixes the length scale associated with this interaction. In the simulations we chose  $r_0 \equiv 1$ .

The elastic bond between two adjacent monomers is modeled by the finitely extensible nonlinear elastic (FENE) potential [148–150] and a Lennard-Jones potential, controlled by the potential width and asymmetry parameter  $\eta$ ,

$$U_{\text{B}}(r) = -\frac{1}{2}KR^2 \ln \left[ 1 - \left( \frac{r - r_0}{R} \right)^2 \right] + \eta[U_{\text{LJ}}(r) + \epsilon] - (U_{\text{shift}} + \epsilon). \quad (6.3)$$

The maximum bond extension is limited by the FENE potential, which diverges for  $r \rightarrow r_0 \pm R$ . The FENE parameters are set to standard values  $R \equiv 3/7$  and  $K \equiv 98/5$ . The Lennard-Jones potential of the bonded interaction causes an asymmetry for  $\eta > 0$  and

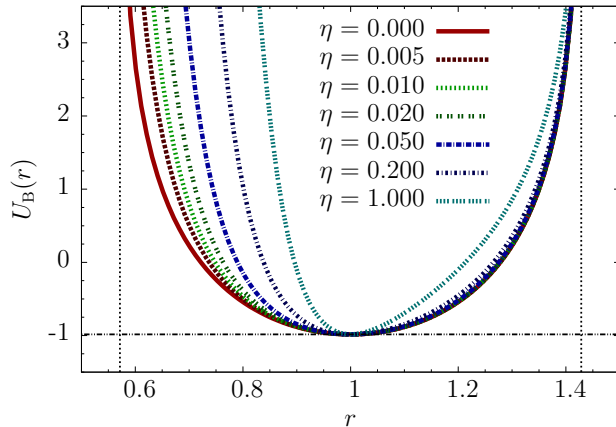


Figure 6.2: Potentials between bonded monomers, modeled by a FENE potential and Lennard-Jones interaction for different values of the parameter  $\eta \in [0, 1]$  that controls the width and asymmetry of the bonded potential.

reduces the potential width, while the location of the minimum  $r_0 = 1$  is unchanged for this choice of parameters. The potential is shifted to have the same minimum value as in the non-bonded case:  $U_B(r_0) = -\epsilon - U_{\text{shift}} = U_{\text{NB}}(r_0)$ . Figure 6.2 shows the bonded potentials for various values of the  $\eta$  parameter. The overall energy scale  $\epsilon$  is set to unity.

In our model, the total energy of a conformation  $\mathbf{X} = (\vec{r}_1, \dots, \vec{r}_L)$  with the monomer-monomer distance  $r_{jk} = |\vec{r}_j - \vec{r}_k|$  is given by

$$E(\mathbf{X}) = \sum_{j=1}^{L-2} \sum_{k=j+2}^L U_{\text{NB}}(r_{jk}) + \sum_{j=1}^{L-1} U_B(r_{j,j+1}), \quad (6.4)$$

where  $L$  represents the number of monomers.

## 6.2.2 Simulation methods

For 21 different values of  $\eta \in [0, 1]$ , thermodynamic and structural quantities were measured in parallel tempering simulations [73–76]. In our implementation of this replica-exchange

Monte Carlo method, Metropolis sampling was performed at  $m = 96$  to 128 different temperatures  $T_i, i = 1, \dots, m$ . At each temperature, displacement updates  $\vec{r} \rightarrow \vec{r} + \vec{d}$  were employed within a cubic box with edge lengths  $l_i > |d_n|, n = 1, 2, 3$ . The size of the box  $l_i$  was adjusted for every temperature thread separately prior to the simulation in order to achieve a Metropolis acceptance rate of approximately 50%. To facilitate the decorrelation of structures, exchanges of replicas between neighboring temperatures are proposed and accepted with the exchange probability in Eq. 3.11. The temperatures  $T_i \in [0.11, 3.00]$  were chosen equally distant in inverse temperature space to guarantee sufficiently high exchange probabilities in the low-temperature regime, where large autocorrelation times are expected. The high exchange probabilities were confirmed by checking if enough round-trip times, which is the number of times that a marked temperature thread walks along the temperature ladder for a round trip, has been achieved in the simulation. Between subsequent exchanges the periods of equilibration and sampling were chosen to be  $5.5 \times 10^4$  MCS each. With  $10^6$  replica exchanges, the total number of MCS in each thread amounted to  $1.1 \times 10^{11}$ .

However, for the structural analysis of the solid pseudophase, parallel tempering is not the optimal method for the sampling of configurations at very low temperatures. Because high density of temperature threads is required in order to keep a reasonable acceptance probability for the swap updates. This is computationally very expensive. In order to compensate for its disadvantage, we utilized a simple parallel version of multicanonical sampling [7, 52, 79, 80, 84] discussed in Sec. 3.5 as a supportive method. This combination of simulation methods not only allows for the verification of the simulation results achieved by parallel tempering, but also enables reweighting to any temperature. For multicanonical sampling, we also used the displacement update. In both the parallel tempering and the parallel version of multicanonical sampling simulations, the MARSAGLIA pseudo random number generator was utilized.

For the 15-mer polymer, we estimated the density of states by using multicanonical

sampling. While for the 55-mer, the final density of states was constructed by combining the estimates obtained from the different temperature threads in parallel tempering simulation with the “weighted histogram analysis method” (WHAM) [77, 78] (see Sec. 3.4). The estimated density of states was utilized to study the structural transitions with microcanonical inflection-point analysis. In the simulation, the derivatives of microcanonical entropy  $S(E)$  were calculated by utilizing eleven-point stencil. But discrete calculation of derivatives quickly amplifies the noise of  $S(E)$  when applied directly. Therefore, it is useful to smooth  $S(E)$  before applying the stencil. We used the Bézier algorithm [7, 97, 98]. The higher derivatives of microcanonical entropies were also smoothed before analyzing the structural transitions.

## 6.3 Results for a 15-mer

### 6.3.1 Canonical and microcanonical statistical analysis

First we discuss the results of canonical statistical analysis applied to our generic model. Heat-capacity curves as functions of temperature (Fig. 6.3(a)) are constructed using the time series of data collected in the multicanonical production run. At  $T \approx 0.34$ , broad prominent peaks, indicating the freezing transition, are identified for all simulated  $\eta$  values. At this transition, globular structures change to more compact crystalline or amorphous structures. For  $\eta = 0$ , an additional peak emerges at  $T = 0.11$ , suggesting the existence of a solid-solid pseudophase transition. With increasing values of  $\eta$  the peak becomes more pronounced as it gradually shifts towards zero temperature and finally disappears when  $\eta \geq 0.1$ . However, the order of the individual pseudophase transitions remains ambiguous and the broad peaks of the freezing transition may envelope several pseudophase transitions which cannot be resolved by the methods of canonical analysis. Therefore we further examine the system using a more systematic and robust approach. One such method that has proven to reliably

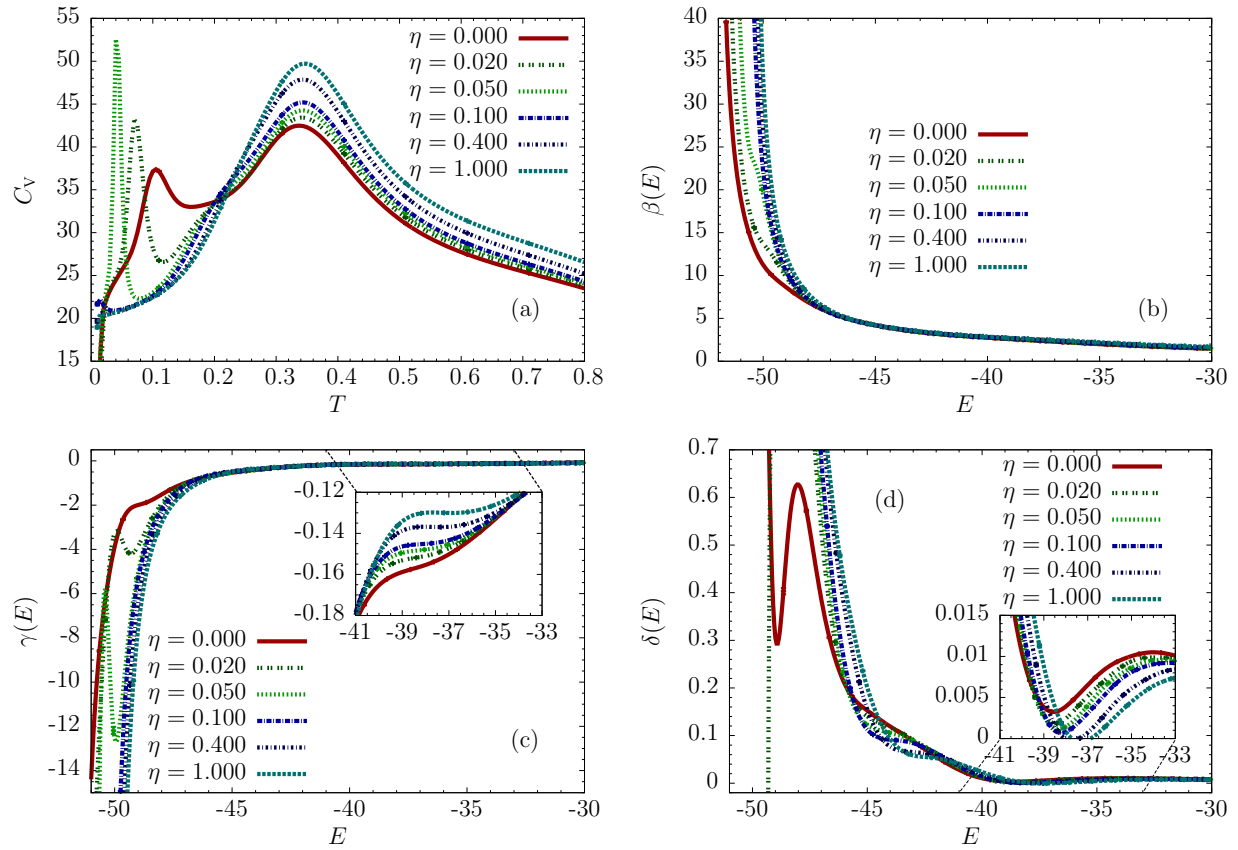


Figure 6.3: (a) Heat capacity  $C_V$ , (b) microcanonical inverse temperature  $\beta(E)$ , and (c,d) its first and second derivatives  $\gamma(E)$  and  $\delta(E)$ , respectively.

signal transitions is the microcanonical inflection-point analysis [20, 23].

The microcanonical results are shown in Fig. 6.3(b-d) for six different values of  $\eta$ . Careful inspection of the first and second derivatives of  $\beta(E)$  in the energy region  $E \in [-45.5, -33]$  reveals that the broad peak in the canonical specific heat encloses two distinct pseudophase transition signals; clear indication that the freezing transition is a two-step process. The first signal located at  $E \approx -44$ , is a fourth-order pseudophase transition indicated by the corresponding least sensitive inflection point in  $\delta(E)$ . The second pseudophase transition, found at  $E \approx -38$ , is of third order for  $\eta \leq 0.2$ , but it is classified as a second-order pseudophase transition for higher values of the potential width and asymmetry parameter. In agreement with the canonical results, we have also identified signals corresponding to a solid-solid pseudophase transition for values of  $\eta \leq 0.1$ . For  $\eta = 0.02$  and  $0.05$ , the negative-valued peaks in  $\gamma(E)$  at energies  $E = -49.7$  and  $-50.4$  respectively, indicate a second-order pseudophase transition. The inflection point in  $\gamma(E)$  and the corresponding positive valley in  $\delta(E) = d\gamma(E)/dE$  at  $E = -48.92$  reveal that for  $\eta = 0.00$  the solid-solid pseudophase transition is of third order.

### 6.3.2 pseudophase diagram

The pseudophase diagram is constructed on the basis of the signals identified in the microcanonical analysis and plotted in Fig. 6.4. In the “gas” pseudophase at high energies, the polymer expands in free space and forms random-coil structures. As the energy decreases, the expanded chain undergoes a second-order collapse transition and enters the “liquid” pseudophase consisting mainly of globular structures. Passing the third/second-order pseudophase transition associated with the nucleation process, the polymer enters the  $S_{ic-core}$  pseudophase in which incomplete icosahedral structures become dominant. Further decrease in energy weakens thermal fluctuations and allows for the formation of a stable surface layer. The pseudophase transition associated with the surface formation process is of fourth order.

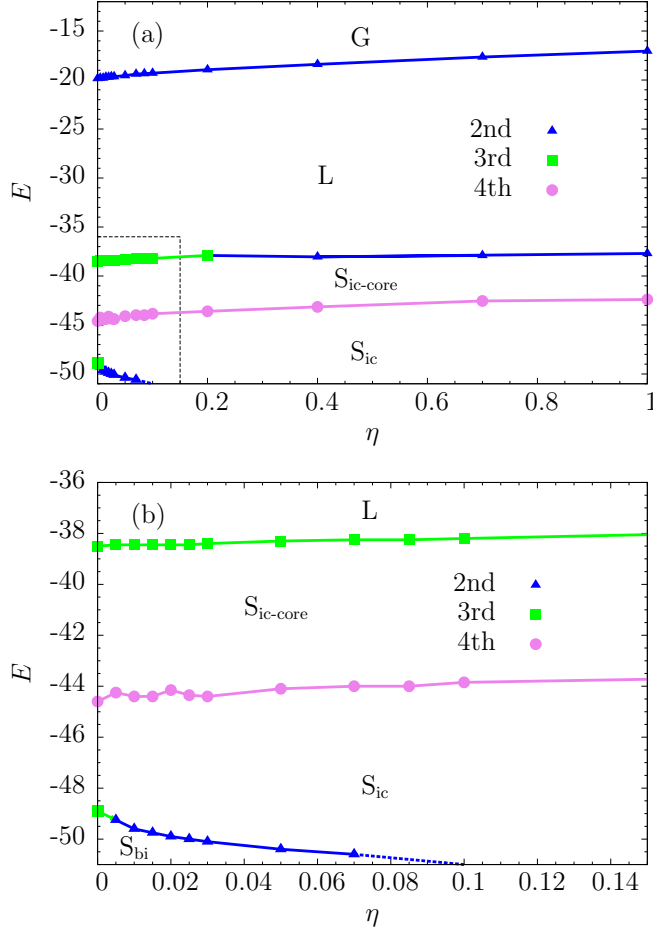


Figure 6.4: (a) Microcanonical pseudophase diagram parameterized by energy and the potential width and asymmetry parameter  $\eta$ . Here, G, L, and S stand for “gas”, “liquid”, and “solid” structural phases, respectively. The  $S_{ic-core}$  pseudophase consists mostly of incomplete icosahedral structures.  $S_{ic}$  and  $S_{bi}$  incorporate compact icosahedral and bihexagonal structures, respectively. (b) Enlarged section detailing the low energy region for  $\eta < 0.15$ . The solid-solid pseudophase transition line is extended by a dashed empirical line constructed based on the data provided by structural analysis.

Visual inspection of low-energy structures reveals that icosahedral geometries are dominant. However, for  $\eta \leq 0.1$ , the additional solid-solid pseudophase transition suggests the existence of low-energy conformations with unexpected geometric properties. In order to examine the low-energy structures systematically, we carry out a careful structural analysis utilizing a suitable set of order parameters.

### 6.3.3 Structural analysis

Various order parameters, such as the number of monomer-monomer contacts, radius of gyration, or radial and angular distributions, have proven to provide valuable insight into the thermodynamic and structural properties of polymer systems. Based on the microcanonical results in Fig. 6.4, we expect the existence of two solid pseudophases when the strength of the potential width and asymmetry parameter is sufficiently small ( $\eta \leq 0.1$ ). We aim to identify the dominant structures in the low-energy pseudophases and to gather additional data supporting the existence of the solid-solid pseudophase transition line. For this purpose, we employ a set of order parameters exploiting the symmetry properties of real spherical harmonics [160].

We define a polymer core to consist of monomers within a distance  $r_{\text{core}} < 1.25\sigma$  of the central monomer, which has been chosen to be nearest to the center of mass. Let  $\mathcal{C} = \{\vec{r}_1, \dots, \vec{r}_M\}$  be the coordinates of a core with  $M$  monomers. Various core geometries can be distinguished using the set of rotationally invariant order parameters

$$Q_l = \left[ \frac{4\pi}{2l+1} \sum_{m=-l}^l |\rho_{l,m}|^2 \right]^{1/2}, \quad (6.5)$$

where

$$\rho_{l,m} = \frac{1}{M} \sum_{i=0}^M Y_{l,m}(\vec{r}_i) \quad (6.6)$$

is the average of the real spherical harmonics evaluated at the locations of the core monomers. The connection between the real and complex spherical harmonics is given by

$$Y_{lm} = \begin{cases} \frac{i}{\sqrt{2}} [Y_l^m - (-1)^m Y_l^{-m}] & \text{if } m < 0, \\ Y_l^m & \text{if } m = 0, \\ \frac{1}{\sqrt{2}} [Y_l^{-m} + (-1)^m Y_l^m] & \text{if } m > 0. \end{cases} \quad (6.7)$$

Using of the order of  $10^6$  polymer structures per value of  $\eta$ , we computed  $Q_l$  up to  $l = 6$  and found that  $Q_6$  can be used most effectively to resolve the geometries of the low-energy conformations. We present the results in the form of intensity plots in Fig. 6.5. The probability of detecting a structure with a specific value of the order parameter at an energy  $E$  is represented by shading; red indicating the maximum probability and black corresponding to zero. In agreement with the microcanonical and canonical results, we detect a single solid pseudophase for  $\eta > 0.1$ , corresponding to the narrow funnel in  $Q_6$  below the pseudophase transition line at  $E \approx -43$ . The dominant structures in this region contain an icosahedral core which is typically found in the ground-state conformations of many short polymer chains. Below  $\eta = 0.1$ , the 15-mer explores an additional solid pseudophase, as indicated by the appearance of a second funnel centered around  $Q_6 \approx 0.41$ . Structures which populate this pseudophase possess an unusual bihexagonal geometry. The energy at which both pseudophases coexist agrees well with the microcanonical estimates for the solid-solid pseudophase transition. Representative structures of both solid pseudophases are shown in Fig. 6.6.

The shape of the bonded potential has undoubtedly a strong effect on the geometry of the ground state. Having identified the two dominant structure types, we may ask why the additional LJ term in the bonded potential eventually precludes the existence of the bihexagonal pseudophase. The answer is readily obtained by comparing the average bond

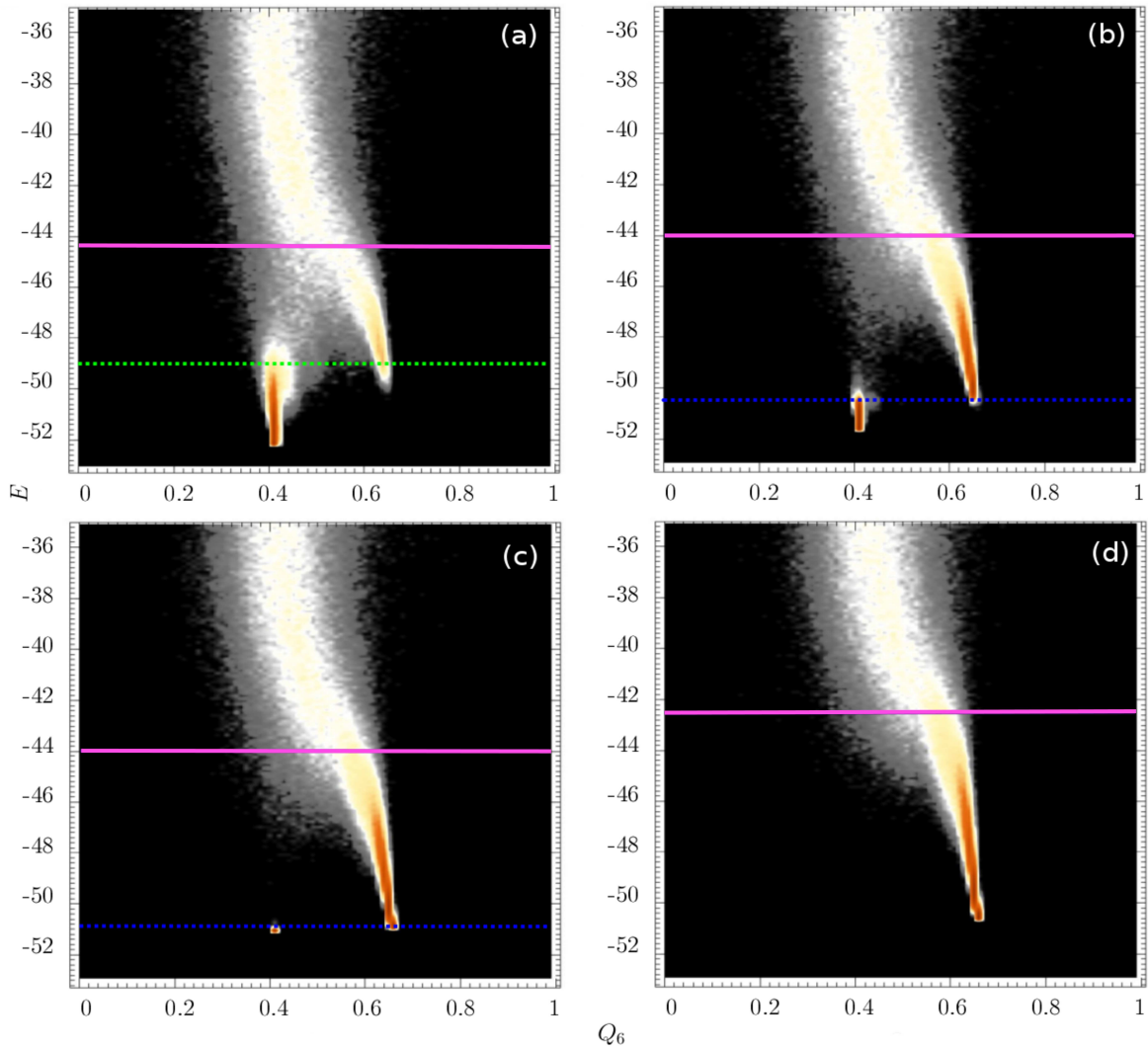


Figure 6.5: (a,b,c,d) Intensity plots of the  $Q_6$  order parameter for a 15-mer with  $\eta = 0.00, 0.05, 0.10, 1.0$ . The shading indicates the probability of detecting a configuration with a given value of the order parameter, red being the maximum probability and black being the lowest. The freezing and the solid-solid pseudophase transitions are indicated by solid and dashed horizontal lines respectively. For  $\eta \leq 0.1$ , the polymer has two distinct solid pseudophases. In addition to the icosahedral pseudophase ( $Q_6 \approx 0.65$ ) the polymer is found in the bihexagonal pseudophase at low energies ( $Q_6 \approx 0.41$ ).

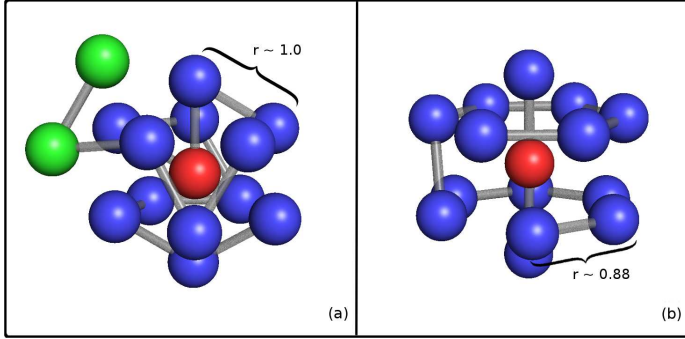


Figure 6.6: Two distinct low-energy structures of the elastic 15-mer. (a) Compact structure with a stable icosahedral core and two monomers displaced onto the incomplete second layer. (b) The bihexagon is the preferred ground-state geometry for  $\eta \leq 0.1$ .

lengths for the icosahedral and bihexagonal structures. The bihexagon accommodates all monomers into a single shell allowing for a larger number of non-bonded interactions and consequently lower energy. However, the two six-monomer rings of the bihexagon contain significantly compressed bonds ( $r_{\text{bond}} \approx 0.88r_0$ ), which become energetically infeasible as  $\eta$  increases. In contrast, we find near-optimal bond lengths in the icosahedron ( $r_{\text{bond}} \approx r_0$ ), hence the “narrowing” of the bonded potential imposes no additional energetic penalty.

## 6.4 Results for a 55-mer

### 6.4.1 Canonical statistical analysis

Figure 6.7 shows the plots of  $C_V$  and  $d\langle R_{\text{gyr}}^2 \rangle / dT$  of the 55-mer as functions of temperature  $T$  for various  $\eta$  values. The clear peaks in the  $d\langle R_{\text{gyr}}^2 \rangle / dT$  curve at  $T \approx 1.6$  in Fig. 6.7(b) indicate the  $\Theta$ -transition, where an extended coil collapses into a globular structure. One can observe that increasing  $\eta$  leads to a shift of the  $\Theta$ -transition to lower temperatures. Reducing temperatures makes globular structures freeze into solid conformations. The corresponding pseudophase transition signals can be observed in the group of peaks in  $C_V$  and  $d\langle R_{\text{gyr}}^2 \rangle / dT$  at temperatures around  $T = 0.3$ . These pseudophase transition signals slightly shift to lower

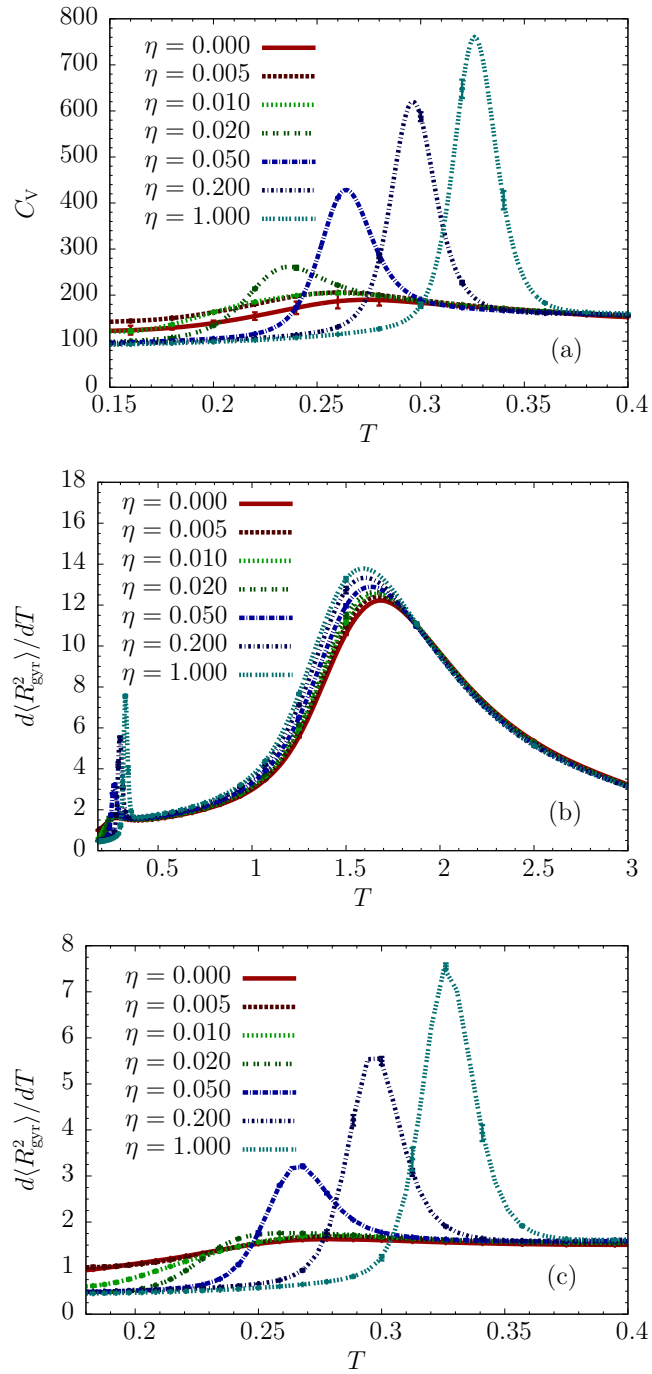


Figure 6.7: (a) Heat capacity  $C_V$ ; (b) and (c) thermal fluctuation of the squared radius of gyration  $d\langle R_{\text{gyr}}^2 \rangle / dT$  of a flexible polymer  $L = 55$  for different values of  $\eta$ . Note the different scales in (c).

temperatures for small  $\eta$  values but start to move to higher temperatures when  $\eta \geq 0.2$ . Among these peaks, the signals with narrow widths and high peak heights at  $\eta \geq 0.2$  indicate the freezing transition. These signals become less pronounced and broader as  $\eta$  decreases. Instead of being the indicators for a specific type of pseudophase transition, these wide and low peaks are envelopes of multiple pseudophase transition signals. This ambiguity in distinguishing and classifying the pseudophase transitions at low  $\eta$  values is caused by finite-size effects which cannot be resolved by means of canonical analysis. It is necessary to employ other systematic and robust methods which can clearly distinguish the sensitive pseudophase transition signals in finite-size systems. Among other approaches, microcanonical inflection-point analysis satisfies these needs.

### 6.4.2 Microcanonical analysis and pseudophase diagram

Applying microcanonical inflection-point analysis [7, 20, 23] for seven exemplary values of  $\eta$  allows for the estimation of the microcanonical entropy and its derivatives. The entropy plots are shown in Fig. 6.8(a). Simulations with  $\eta = 0.05, 0.2$ , and 1 exhibit backbending behaviors in  $\beta(E)$  in Fig. 6.8(b) and corresponding positive peaks in  $\gamma(E)$  in Fig. 6.8(c). These properties imply that the system undergoes first-order pseudophase transitions at temperatures  $T \approx 0.3$ . For  $\eta = 0.02$ , we find a least sensitive inflection point at  $E \approx -241$  in  $\beta(E)$  and a corresponding negative peak within  $\gamma(E)$ . This signal indicates a second-order pseudophase transition that occurs at  $T \approx 0.23$ . At the same time, one can observe the inflection points besides the peaks in the  $\gamma(E)$  curves, located at  $E \approx -247, -242, -235$ , and  $-229$  for  $\eta = 0.02, 0.05, 0.2$ , and 1 respectively. Together with the corresponding positive valleys in the  $\delta(E)$  curves in Fig. 6.8(d), these inflection points help identify third-order pseudophase transitions.

Based on microcanonical inflection-point analysis for 19  $\eta$  values, we constructed a microcanonical pseudophase diagram, which is shown in Fig. 6.9(a). At high temperatures,

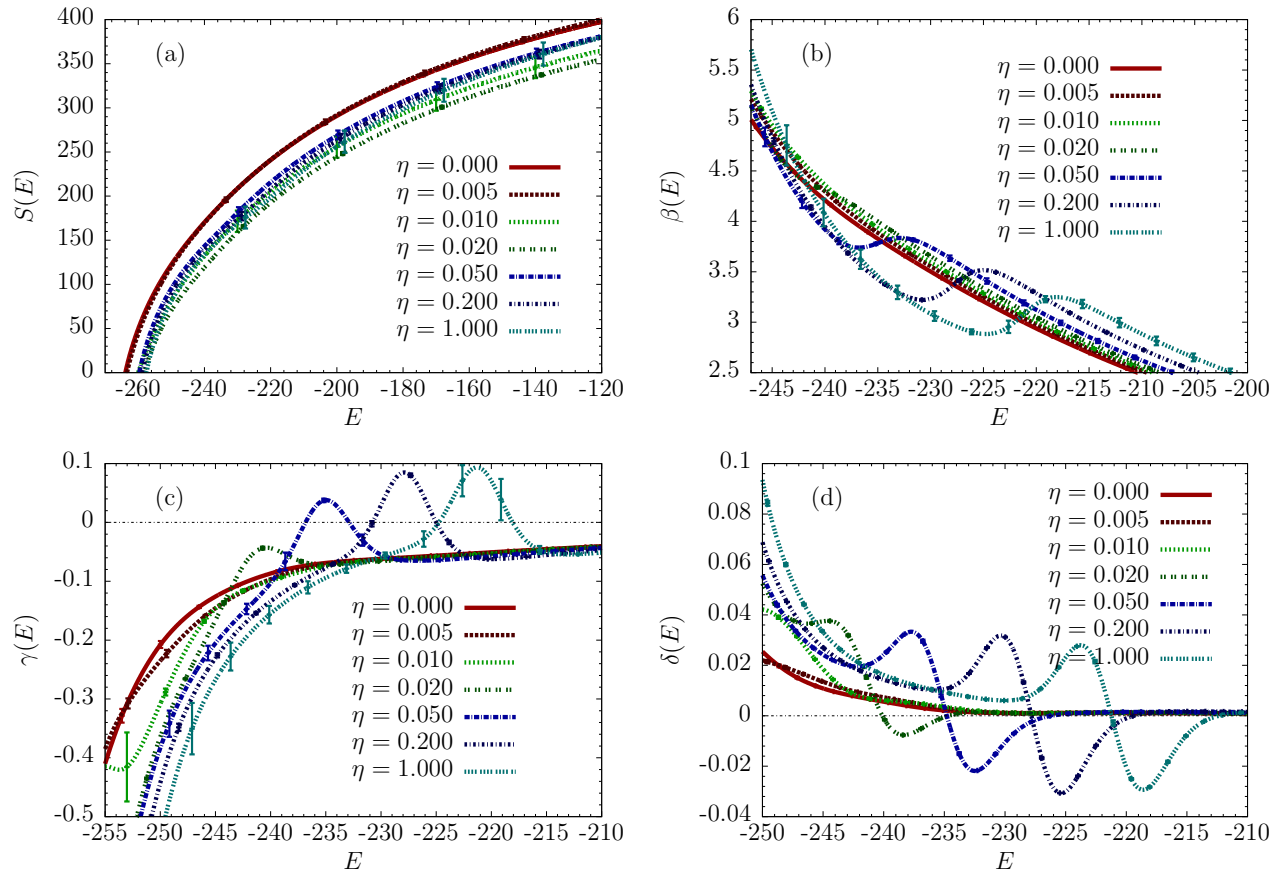


Figure 6.8: (a) Microcanonical entropy  $S(E)$  for an array of  $\eta$  values; (b) microcanonical inverse temperature  $\beta(E)$ ; (c)  $\gamma(E)$ ; (d)  $\delta(E)$ .

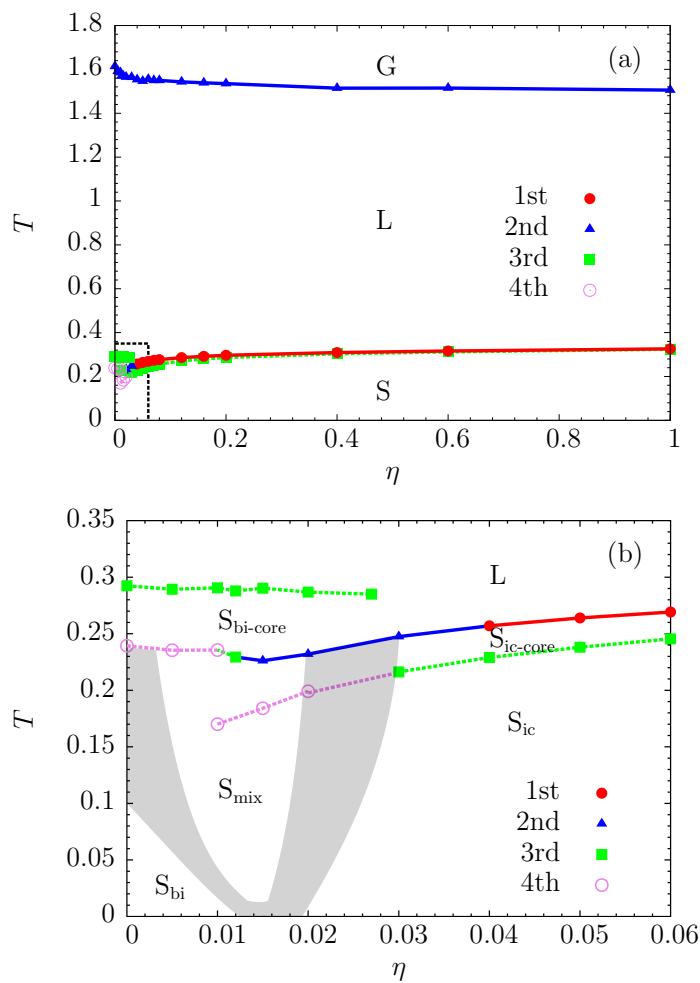


Figure 6.9: (a) Microcanonical pseudophase diagram. Here,  $G$ ,  $L$ , and  $S$  represent “gas”, “liquid”, and “solid” pseudophase, respectively. (b) Low-temperature and small- $\eta$  value region, emphasizing the different solid pseudophases. In  $S_{bi-core}$  structures with bihexagonal cores and liquid-like shells are dominant.  $S_{ic-core}$  represents structures with well-formed icosahedral cores but incomplete surface layer. In the  $S_{ic}$  and  $S_{bi}$  pseudophases, icosahedral and bihexagonal core structures with complete shells dominate. In  $S_{mix}$  icosahedral and bihexagonal core structures coexist. The “solid” subphases are separated by gray empirical transition bands. Dashed lines represent lines of pseudophase transitions higher than second order.

the polymer is in the gas-like pseudophase in which dissolved or random coils can be observed. Decreasing the temperature causes the polymer to collapse and to enter the liquid pseudophase, where compact globular conformations are favorably formed. The corresponding pseudophase transition is the well-known  $\Theta$ -transition (collapse transition). Because of the negative  $\gamma(E)$  peaks for all  $\eta$  values, this pseudophase transition is classified as of second order and it is represented by the blue line in Fig. 6.9(a). As the temperature decreases further, the polymer transfers from the globular pseudophase to the more compact “solid” pseudophase which is characterized by locally crystalline or amorphous metastable structures. A magnification of the low-temperature and small- $\eta$  region of the pseudophase diagram, shown in Fig. 6.9(b), displays multiple pseudophase transition lines. In this graph, the freezing transition is recognized by the microcanonical inflection-point analysis as of first order for  $\eta > 0.04$  and of second order for  $\eta < 0.04$ . This qualitative change is also reflected in Fig. 6.8(b) and (c) where the monotonicity in the backbending region changes and positive gamma peaks gradually turn to negative ones as  $\eta$  becomes smaller. Nevertheless, since the order of the freezing transition extension line in the low- $\eta$  value region is higher than second, it is worth discussing it in more detail. In addition, the pseudophase diagram in Fig. 6.9(b) exhibits various higher-order pseudophase transition lines and diverse structures in the low-temperature regions as  $\eta$  varies. Visual inspection of numerous structures only is not enough to interpret the conformational phases in the complete pseudophase diagram. A more systematic structural analysis is necessary to distinguish the conformational differences among these subphases.

### 6.4.3 Structural analysis

For the purpose of identification of low energy solid-like structures which possess well-defined symmetries, we employed a set of suitable order parameters. As expected, preliminary inspection of structures obtained from simulations of the unmodified, flexible 55-mer ( $\eta \approx 1$ )

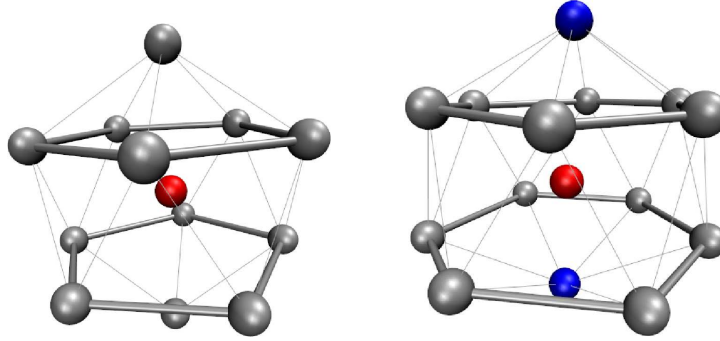


Figure 6.10: Polymer core structures: (left) icosahedral (ic-core); (right) bihexagonal (bi-core); both found in a 55-mer at low energies in the range  $0 < \eta < 0.025$  of the bond potential parameter that controls width and asymmetry.

shows that below the freezing transition virtually all conformations contain an icosahedral core. However, with sufficiently weak bonded Lennard-Jones interactions ( $\eta < 0.03$ ), two distinct core geometries are found. In addition to the standard icosahedral core, which is found in the global minimum structures of most short chains, we have identified a bihexagonal core consisting of 15 monomers (Fig. 6.10). The six-fold dihedral symmetry of the bihexagon and the icosahedral symmetry are best distinguished using the  $Q_6$  order parameter [160]. For a perfect icosahedral core,  $Q_6 \approx 0.65$ , whereas a bihexagonal core corresponds to  $Q_6 \approx 0.41$ .

We present the results in the form of intensity plots in Fig. 6.11. Shades correspond to the probability of finding a structure with a particular value of  $Q_6$  at a given microcanonical temperature  $T(E)$ . Black corresponds to zero probability and red to unity. An interesting feature, found only in systems with  $\eta < 0.027$ , is marked by the green horizontal lines at  $T \approx 0.29$ . It is associated with the apparent shift of the peak of the  $Q_6$  distribution at this temperature towards lower values. This indicates the onset of the formation of bihexagonal cores in the liquid pseudophase and corresponds to the third-order pseudophase transition line in the microcanonical pseudophase diagram (Fig. 6.9(b)). Below this transition, amorphous structures with loose bihexagonal cores and liquid-like surfaces are identified in the

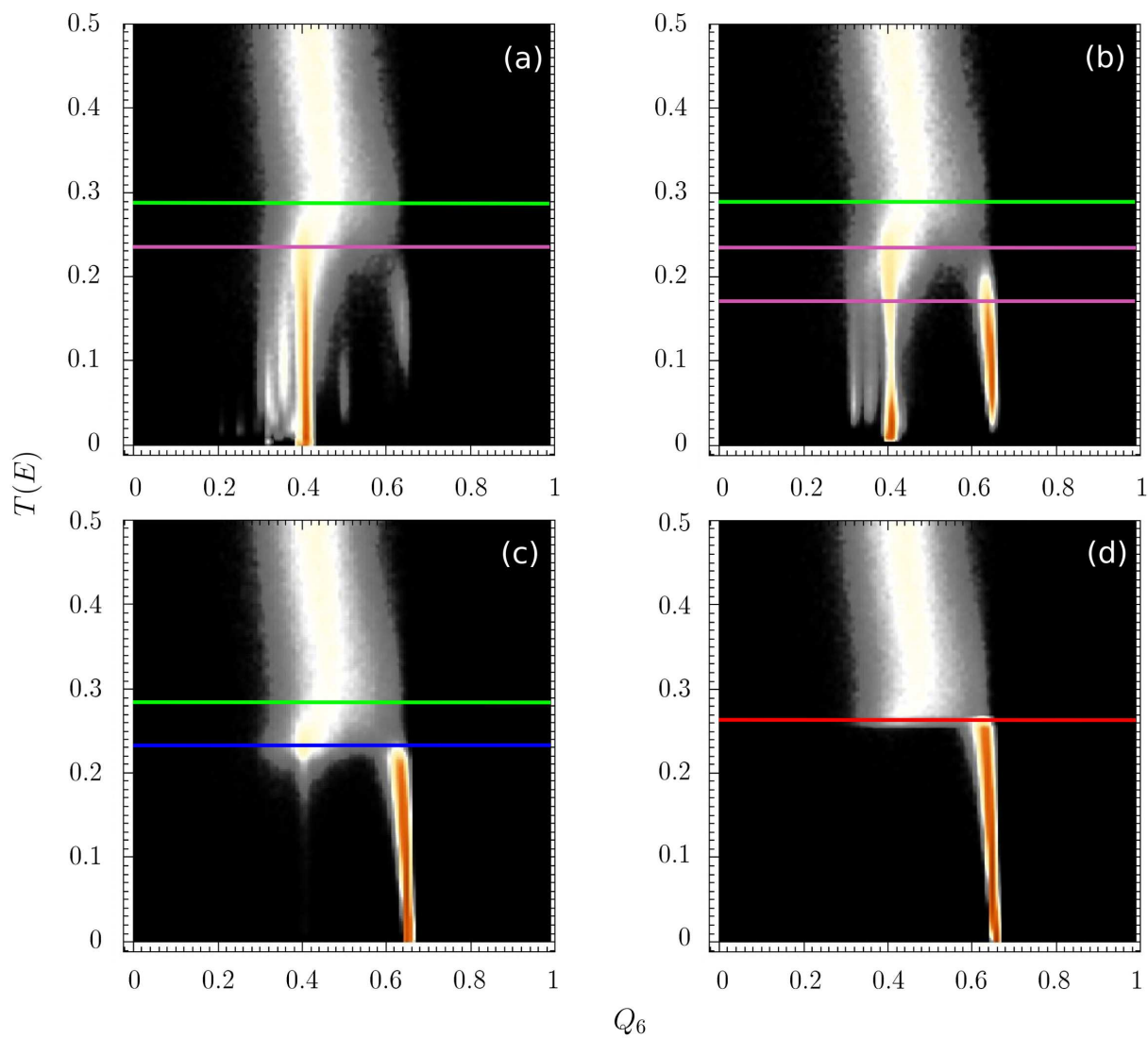


Figure 6.11: (a, b, c, d) Intensity plots of the  $Q_6$  order parameter corresponding to  $\eta = 0.005, 0.010, 0.020, 0.050$ , respectively. The probability of finding polymer structures with a particular value of  $Q_6$  is represented by shading, with black being zero probability and red corresponding to the maximum probability of 1.

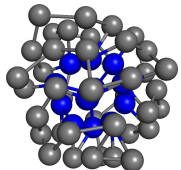
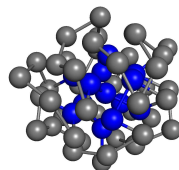
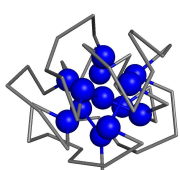
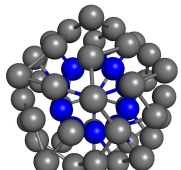
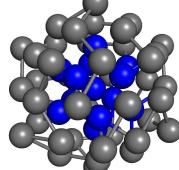
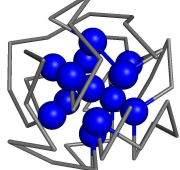
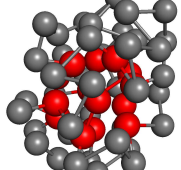
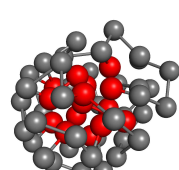
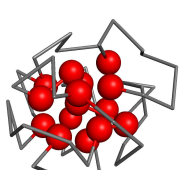
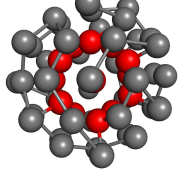
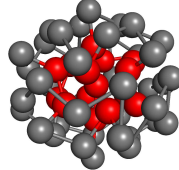
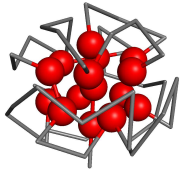
Phase	Conformations		
$S_{ic-core}$			
$S_{ic}$			
$S_{bi-core}$			
$S_{bi}$			

Figure 6.12: Typical structures of “solid” subphases. The figures in the same row are different representatives of the same conformation. Icosahedral and bihexagonal cores are plotted in blue and red respectively. Gray beads represent surface monomers. The structures in the third column shows the explicit cores. The surface monomers are represented by a wireframe.

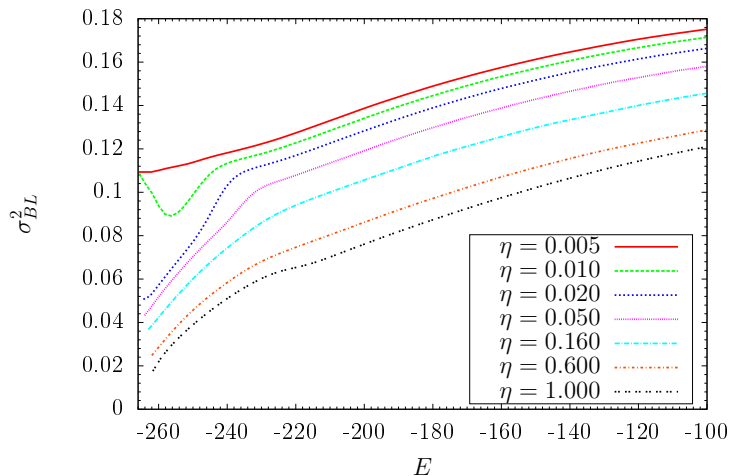


Figure 6.13: The bond-length variance  $\sigma_{BL}^2$  of the 55-mer as a function of energy for different values of the model parameter  $\eta$ .

$S_{\text{bi-core}}$  pseudophase. Typical conformations are plotted in Fig. 6.12.

At low temperatures and  $\eta = 0.005$ , we identify a single dominant funnel centered at  $Q_6 \approx 0.41$ , containing structures with a bihexagonal core. The adjacent secondary funnels all contain bihexagonal cores with slightly modified inter-monomer distances. Structures with an icosahedral core are found in the weakly populated funnel at  $Q_6 \approx 0.65$ . The low-temperature pseudophase transition signal is associated with the increase in the population of structures with bihexagonal cores and is classified as of fourth order. This transition signal is marked by violet pseudophase transition lines in Fig. 6.11(a) and the pseudophase diagram in Fig. 6.9(b). A small increase in the strength of the bonded LJ potential leads to a sharp increase in the population of icosahedral cores. If  $\eta = 0.01$ , the ground state of the polymer is still found in the bihexagonal funnel, however the onset of a significant population of icosahedral cores produces an additional fourth-order pseudophase transition signal at  $T = 0.17$  in both Fig. 6.9(b) and the Fig. 6.11(b). Further increase leads to a sharp decline in the population of the bihexagonal funnel.

This can be seen clearly for  $\eta \geq 0.02$  [see Fig. 6.11(c), (d)] where the energetic penalty for non-optimal bond lengths becomes too large to accommodate structures with bihexagonal cores. Indeed, their formation requires significant variance in bond lengths, whereas icosahedral cores can be formed with near-optimal values. For  $\eta \approx 0$ , the pure FENE potential permits large bond fluctuations. However, with the introduction of the bonded LJ potential these fluctuations cause an energetic penalty. This explains why the bihexagonal funnel exists only when the bonded LJ potential is sufficiently weak. In Fig. 6.13, we show the bond-length variance as a function of energy for different values of the model parameter  $\eta$ . With increasing values of  $\eta$  the variance decreases, most significantly in the low-energy region. Most striking is the difference between the low-energy curves for  $\eta = 0.01$  and  $\eta = 0.02$ , where the former has a bihexagonal ground-state and the latter is icosahedral.

At  $\eta \approx 0.04$ , the signal associated with the onset of the icosahedral funnel becomes first order and can be unambiguously identified as the freezing transition. Beyond  $\eta \approx 0.1$ , the structural and energetic properties of the polymer are virtually identical to the standard model ( $\eta = 1$ ).

To sum up the information provided by the intensity plots in Fig. 6.11, and the plot of the bond-length variances in Fig. 6.13, the low-temperature behavior of this flexible polymer model can be classified into three pseudophases. For sufficiently small  $\eta$  values, bihexagonal core structures with compact hexagonal-like surface layers, shown in Fig. 6.12, can be observed. As  $\eta$  gradually increases, icosahedral structures gradually become more dominant due to the increase of the energy penalty of the non-optimal bond lengths. This results in the appearance of the mixture of these two low-temperature structure types [ $S_{\text{mix}}$  in the Fig. 6.9(b)]. Once the width of the bonded potential is sufficiently narrow, the bihexagonal core structures completely vanish and only the icosahedral structures persist. The corresponding pseudophase is labeled  $S_{\text{ic}}$  in Fig. 6.9 and representative structures are shown in Fig. 6.12.

The third-order pseudophase transition accompanying the freezing transition in Fig. 6.9(b) is associated with the completion of the icosahedral shell. Upon decreasing the temperature, liquid structures begin to nucleate and first form the stable icosahedral cores if  $\eta > 0.03$ . Surfaces of the polymer structures still undergo large fluctuations in order to arrange the surface monomers in optimal locations. The mobility of the monomers is confined to effectively two dimensions on the surface. These structures are formed in the  $S_{\text{ic-core}}$  pseudophase. If the temperature is decreased further, the surface formation finishes and complete icosahedral shell structures appear in the  $S_{\text{ic}}$  pseudophase.

By applying a microcanonical analysis to this elastic flexible polymer model, the hierarchy of the freezing transitions has been illustrated and classified into two processes, i.e., the nucleation process which is identified by the first- or second-order pseudophase transition and the surface layer formation which is related to the third-order pseudophase transition.

## 6.5 Conclusions

Performing parallel tempering simulations, supported by a parallel version of multicanonical sampling, we have investigated the effects of the shape of the potential of bonded monomers on the structure formation of elastic flexible polymers. For this purpose, we introduced the model parameter  $\eta$ , which controls the width and asymmetry of the bond potential. In order to identify and distinguish the various structural phases in this system, we systematically applied the microcanonical inflection-point and conformational analysis to construct the pseudophase diagram.

For the 15-mer, a freezing transition into an icosahedral pseudophase precedes a solid-solid pseudophase transition into low-energy states with bihexagonal geometry for small values of  $\eta$ . The non-optimal bond lengths found in bihexagonal conformations cause a large energy penalty due to the “narrowing” of the bonded potential if  $\eta$  is increased. Hence only

a single solid pseudophase remains for  $\eta > 0.1$ , which is icosahedral. In the 55-mer case, we find similar diverse structure types in the low-temperature region upon varying  $\eta$ . Perturbing the FENE potential allows for larger fluctuations of the bond lengths. Structures with bihexagonal cores are commonly observed for small  $\eta$  values. Increasing  $\eta$  narrows the bond potential width. The energetic penalty for non-optimal bond lengths becomes too large to accommodate structures with bihexagonal cores. Thus, bihexagonal core structures gradually disappear for large  $\eta$  values and icosahedral cores become more dominant. The mixture of these two types of structures finally disappears once the bond potential is dominated by the Lennard-Jones potential. Only polymer conformations with icosahedral core are found if  $\eta$  is sufficiently large. The striking consequences of a relatively small modification to the standard model of elastic, flexible homopolymers illustrate the importance of a careful choice of model parameters.

Another remarkable feature of our study is the observation of a hierarchy of the freezing transition. For the 55-mer, the nucleation process is a first/second-order pseudophase transition but the accompanying shell formation process turns out to be a third-order pseudophase transition. For the 15-mer, these two “transitions” are of second/third and fourth orders, respectively. This feature fully demonstrates the power of the microcanonical inflection-point analysis which not only helps identify the major transitions which are usually first- and second-order but can also distinguish the details of the transition processes which are usually presented as higher than second-order pseudophase transitions in finite systems.

The conclusions for the case studies of 15 and 55-mer are stable and robust. Small variation of the polymer length does not qualitatively change the pseudophase diagram constructed by the combination of microcanonical inflection-point and structural analysis. However, it should be noted that structural properties depend sensitively on the system size and changes of characteristic features are expected. A systematic extension of our study to larger systems is future work.

# Chapter 7

## Summary and outlook

The main work of this thesis is to introduce novel statistical and conformational analysis methods that can be applied to investigate the structural transitions in finite systems in which the structural properties are affected by finite-size or surface effects. The conventional canonical analysis method, which is based on Ehrenfest's scheme defined in the thermodynamic limit, utilizes internal energy, average magnetization, and average radius of gyration and their fluctuations like heat capacity, susceptibility, and thermal fluctuation of radius of gyration to identify and locate phase transitions. The orders of the transitions are classified according to the discontinuities and divergences in the derivatives of the thermodynamic potentials such as the Helmholtz free energy and the Gibbs enthalpy. However, due to finite-size effects, when applied to locate pseudophase transition temperatures, different order parameters and their corresponding fluctuations can cause ambiguities that can only disappear in the thermodynamic limit. In addition, pronounced signals such as peaks may not be observed in the fluctuation quantities so that one cannot employ them to identify pseudophase transitions. Therefore, it is suggested to use the signal of slowing down of autocorrelation times, which is indicated by the extremal values in the autocorrelation time curves and implies that the algorithm becomes "slowing down" to generate uncorrelated configurations, as

an alternative method to locate pseudophase transitions when the fluctuation quantities fail to exhibit pronounced peaks. But since autocorrelation times highly depend on the Monte Carlo algorithms and updates, the same problems contained in canonical analysis when applied to study finite-size systems may also appear when the autocorrelation time method is utilized. Therefore, it is necessary to employ other more systematic and reliable methods to clearly distinguish the sensitive pseudophase transition signals in systems of finite size. One of such approaches is the microcanonical inflection-point analysis, which applies the principle of minimal sensitivity to the derivatives of microcanonical entropy  $S(E)$  in order to systematically and uniquely identify and classify transitions. In this method, the first-order pseudophase transitions can be distinguished from the backbending behaviors in the inverse temperatures  $\beta(E)$  and the positive peaks in  $\gamma(E) = d\beta(E)/dE$ . We generalized this approach to any higher-order pseudophase transitions and claimed the following: the  $2k$ th-order pseudophase transition ( $k$  is a positive integer) can be identified from the least sensitive inflection point in the  $(2k - 1)$ th derivative of  $S(E)$  and the negative peak in the  $2k$ th derivative of  $S(E)$ ; the transition energy of the  $(2k + 1)$ th-order pseudophase transition can be located by employing the least sensitive inflection point in the  $2k$ th derivative of  $S(E)$  and the positive valley in the  $(2k + 1)$ th derivative of  $S(E)$ . Pseudophase Transitions higher than second-order, usually revealing the detailed processes of the first/second-order pseudophase transitions, may only appear in finite size systems, due to the finite-size effects, i.e., surface effects. They may not exist in the thermodynamic limit. However, for the studies of the actual finite systems such as proteins and DNA, in which surface effects may be essential in determining the functions of these molecules, higher than second-order pseudophase transitions can be critical in understanding the structural transitions of these systems. In addition, we also found dependent pseudophase transitions whose occurrences depend on the existence of lower-order “regular” pseudophase transitions. These dependent pseudophase transitions may represent the precursors of “regular” pseudophase transitions.

Microcanonical inflection-point analysis is robust. It can be extended and implemented to study phase transitions of systems in the thermodynamic limit.

The first application of our methods is to distinguish the collapse transitions in a simple coarse-grained flexible polymer model by utilizing autocorrelation time properties for different quantities. In this model, atoms contained in a monomer are grouped and represented by an effective interaction bead. The quantum potentials among all the atoms and the solvent effects are replaced by the effective potentials among the beads. We simulated such a system with the Monte Carlo Metropolis algorithm combined with displacement update and estimated the autocorrelation times for various quantities by integration of autocorrelation functions and by using the binning method. The primary result is that slowing down occurs as expected and is clearly represented by peaks in the autocorrelation time estimators near the collapse transition temperature. By comparing with temperatures of extremal thermal structural fluctuations, we claim that the extremal autocorrelation time can also be considered as an indicator for the collapse transition.

We further applied microcanonical inflection-point analysis to study the adsorption of a grafted simple-cubic (sc) lattice polymer model with one end anchored at a flat adhesive surface. To simulate such a system, we employed the generalized-ensemble contact density chain-growth algorithm. The pseudophase diagram constructed solely by microcanonical inflection-point analysis exhibits various pseudophases separated by first- to fourth-order pseudophase transition boundaries. Furthermore, bin size effect on the formation of structural transitions has also been revealed in this discrete model. Our results show that small bin size is necessary to retain the information of the melting process occurring at low temperature, whereas large bin size is preferred in the high temperature region because redundant information about the details of pseudophase transitions and fluctuations can be filtered.

We also applied microcanonical inflection-point analysis to investigate an off-lattice flexible homopolymer model in which the bond potential is controlled by a potential width and

asymmetry parameter  $\eta$ . For  $\eta = 0$ , bonded monomers only interact via the spring-like FENE potential. The Lennard-Jones interaction is incorporated into the bonds by setting  $\eta = 1$ . The system was simulated by using the combination of parallel tempering and a parallel version of multicanonical sampling. The pseudophase diagram was first constructed by utilizing microcanonical inflection-point analysis. In the low temperature region, various solid state subphases separated by third/fourth-order pseudophase transitions have been found. To reveal the physical meanings of these signals, we introduced a set of suitable order parameters including the rotationally invariant order parameter  $Q_6$  and bond-length variance to do conformational analysis. The probability intensity plots of the order parameter  $Q_6$  were constructed by analyzing the collected huge amounts of conformations generated during simulations. These plots show the existence of icosahedral and bihexagonal structures for the 15-mer. For the 55-mer, structures with icosahedral and bihexagonal cores can be observed. Due to the narrow potential width in the  $\eta > 0.1$  region, the non-optimal bond lengths in the bihexagonal structures can cause a large energy penalty. Thus, only the icosahedral structures with the near-optimal bond lengths are allowed. For  $\eta < 0.1$ , in the case of the 55-mer, the mixture of the structures with icosahedral and bihexagonal cores gradually disappears and only the lower energy structures with bihexagonal cores survive as  $\eta$  decreases, whereas the dominating icosahedral structures directly become bihexagonal for the 15-mer. In addition, the hierarchy of the freezing transition was also observed. For the 15- and 55-mer, the nucleation processes were found to be first/second- and second/third-order pseudophase transitions, and the shell formation processes were classified as third- and fourth-order pseudophase transitions.

From the studies of finite-size polymer systems, we can conclude that locating the slowing down of autocorrelation times can be utilized as an alternative method to identify conformational transitions, whereas microcanonical inflection-point analysis is a systematic and robust approach that can be applied to any system. We expect to implement these methods

to study more realistic systems such as proteins and DNA. Our methods may reveal the intrinsic structural transition properties of systems that can not be identified by using the conventional canonical analysis. Additionally, the dependent transitions are also expected to be found in different systems.

# Bibliography

- [1] C. N. Yang and T. D. Lee, Phys. Rev. **87**, 404 (1952); T. D. Lee and C. N. Yang, Phys. Rev. **87**, 410 (1952).
- [2] M. E. Fisher, in *Lectures in Theoretical Physics vol. 7C*, ed. by W. E. Brittin (University of Colorado Press, Boulder, 1965), Chap. 1.
- [3] W. Janke and R. Kenna, J. Stat. Phys. **102**, 1211 (2001); Comp. Phys. Commun. **147**, 443 (2002); Nucl. Phys. B (Proc. Suppl.) **106-107**, 905 (2002).
- [4] J. C. S. Rocha, S. Schnabel, D. P. Landau, and M. Bachmann, Phys. Rev. E **90**, 022601 (2014).
- [5] P. Borrmann, O. Mülken, and J. Harting, Phys. Rev. Lett. **84**, 3511 (2000).
- [6] O. Mülken, H. Stamerjohanns, and P. Borrmann, Phys. Rev. E **64**, 047105 (2001).
- [7] M. Bachmann, *Thermodynamics and Statistical Mechanics of Macromolecular Systems* (Cambridge University Press, Cambridge, 2014).
- [8] D. H. E. Gross, *Microcanonical Thermodynamics* (World Scientific, Singapore, 2001).
- [9] W. Thirring, Z. Phys. **235**, 339 (1970).
- [10] W. Janke, Nucl. Phys. B (Proc. Suppl.) **63A-C**, 631 (1998).

- [11] M. Kastner, M. Promberger, and A. Hüller, *J. Stat. Phys.* **99**, 1251 (2000).
- [12] C. Junghans, M. Bachmann, and W. Janke, *Phys. Rev. Lett.* **97**, 218103 (2006).
- [13] C. Junghans, M. Bachmann, and W. Janke, *J. Chem. Phys.* **128**, 085103 (2008).
- [14] J. Hernández-Rojas and J. M. Gomez-Llorrente, *Phys. Rev. Lett.* **100**, 258104 (2008).
- [15] M. P. Taylor, W. Paul, and K. Binder, *J. Chem. Phys.* **131**, 114907 (2009).
- [16] M. P. Taylor, W. Paul, and K. Binder, *Phys. Rev. E* **79**, 050801(R) (2009).
- [17] M. Möddel, W. Janke, and M. Bachmann, *Phys. Chem. Chem. Phys.* **12**, 11548 (2010).
- [18] P. M. Stevenson, *Phys. Rev. D* **23**, 2916 (1981).
- [19] P. M. Stevenson, *Phys. Lett. B* **100**, 61 (1981).
- [20] S. Schnabel, D. T. Seaton, D. P. Landau, and M. Bachmann, *Phys. Rev. E* **84**, 011127 (2011).
- [21] K. Qi and M. Bachmann, *J. Chem. Phys.* **141**, 074101 (2014).
- [22] K. Qi and M. Bachmann, *Phys. Proc.* **68**, 110 (2015).
- [23] K. Qi and M. Bachmann, *Unleashing the Power of Microcanonical Inflection-Point Analysis: the Principle of Minimal Sensitivity*, preprint (2016).
- [24] K. Qi and M. Bachmann, *Application of the Generalized Microcanonical Inflection-Point Analysis to Polymer Adsorption Transitions*, preprint (2016).
- [25] K. Qi, B. Liewehr, T. Koci, B. Pattanasiri, M. J. Williams, and M. Bachmann, *Influence of Bonded Interactions on Structural Phase Properties of Flexible Elastic Homopolymers*, preprint (2016).

- [26] T. Koci, K. Qi, and M. Bachmann, *The Impact of Bonded Interactions on the Ground-State Geometries of a Small Flexible Polymer*, submitted to J. Phys.: Conf. Ser. (2016).
- [27] R. K. Pathria and P. D. Beale, *Statistical Mechanics*, 3rd ed. (Academic, Boston, 2011).
- [28] M. E. Fisher, Rev. Mod. Phys. **46**, 597 (1974).
- [29] L. P. Kadanoff, W. Götze, D. Hamblen, R. Hecht, E. A. S. Lewis, V. V. Palciauskas, M. Rayl, J. Swift, D. Aspnes, and J. Kane, Rev. Mod. Phys. **39**, 395 (1967).
- [30] M. E. J. Newman and G. T. Barkema, *Monte Carlo Methods in Statistical Physics* (Oxford University Press, Oxford, 1999).
- [31] H. Müller-Krumbhaar and K. Binder, J. Stat. Phys. **8**, 1 (1973).
- [32] W. Janke, *Statistical Analysis of Simulations: Data Correlations and Error Estimation*, in *Proceedings of the Winter School “Quantum Simulations of Complex Many-Body Systems: From Theory to Algorithms”*, John von Neumann Institute for Computing, Jülich, NIC Series vol. **10**, ed. by J. Grotendorst, D. Marx, and A. Muramatsu (NIC, Jülich, 2002), p. 423.
- [33] W. W. Wood, *Physics of Simple Liquids* (Wiley, New York, 1968).
- [34] D. P. Landau and K. Binder, *A Guide to Monte Carlo Simulations in Statistical Physics* (Cambridge University Press, Cambridge, 2000).
- [35] W. Janke, *Monte Carlo Simulations of Spin Systems*, in: *Computational Physics: Selected Methods – Simple Exercises – Serious Applications*, eds. K. H. Hoffmann and M. Schreiber (Springer, Berlin, 1996), p. 10.
- [36] W. Janke, *Nonlocal Monte Carlo Algorithms for Statistical Physics Applications*, Mathematics and Computers in Simulation **47**, 329 (1998).

- [37] N. Metropolis, A. W. Rosenbluth, M. N. Rosenbluth, A. H. Teller, and E. Teller, J. Chem. Phys. **21**, 1087 (1953).
- [38] M. P. Nightingale and H. W. J. Blöte, Phys. Rev. Lett. **76**, 4548 (1996).
- [39] R. Matz, D. L. Hunter, and N. Jan, J. Stat. Phys. **74**, 903 (1994).
- [40] R. H. Swendsen and J. -S. Wang, Phys. Rev. Lett. **58**, 86 (1987).
- [41] U. Wolff, Phys. Rev. Lett. **62**, 361 (1989).
- [42] D. Kandel, E. Domany, D. Ron, A. Brandt, and E. Loh, Jr. Phys. Rev. Lett. **60**, 1591 (1988).
- [43] D. Kandel, E. Domany, and A. Brandt, Phys. Rev. B **40**, 330 (1989).
- [44] A. D. Sokal, *Monte Carlo Methods in Statistical Mechanics: Foundations and New Algorithms*, lecture notes, Cours de Troisième Cycle de la Physique en Suisse Romande, Lausanne, 1989.
- [45] A. D. Sokal, *Bosonic Algorithms*, in: *Quantum Fields on the Computer*, ed. M. Creutz (World Scientific, Singapore, 1992), p. 211.
- [46] P. D. Coddington and C. F. Baillie, Phys. Rev. Lett. **68**, 962 (1992).
- [47] J. D. Gunton, M. S. Miguel, and P. S. Sahni, *The Dynamics of First Order Phase Transitions* in: *Phase Transitions and Critical Phenomena*, Vol. 8, eds. C. Domb and J. L. Lebowitz (Academic Press, New York, 1983), p. 269.
- [48] K. Binder, Rep. Prog. Phys. **50**, 783 (1987).
- [49] H. J. Herrmann, W. Janke, and F. Karsch (eds.), *Dynamics of First Order Phase Transitions* (World Scientific, Singapore, 1992).

- [50] W. Janke, *Recent Developments in Monte Carlo Simulations of First-Order Phase Transitions*, in: *Computer Simulations in Condensed Matter Physics VII*, eds. D. P. Landau, K. K. Mon and H. -B. Schüttler (Springer, Berlin, 1994), p. 29.
- [51] W. Janke, *First-Order Phase Transitions*, in: *Computer Simulations of Surfaces and Interfaces*, NATO Science Series, II. Mathematics, Physics and Chemistry - Vol. **114**, Proceedings of the NATO Advanced Study Institute, Albena, Bulgaria, 9 - 20 September 2002, edited by B. Dünweg, D. P. Landau, and A. I. Milchev (Kluwer, Dordrecht, 2003); pp. 111 - 135.
- [52] B. A. Berg and T. Neuhaus, Phys. Lett. B **267**, 249 (1991); Phys. Rev. Lett. **68**, 9 (1992).
- [53] W. Janke, B. A. Berg, and M. Katoot, Nucl. Phys. B **382**, 649 (1992).
- [54] B. A. Berg, U. Hansmann, and T. Neuhaus, Phys. Rev. B **47**, 497 (1993); Z. Phys. B **90**, 229 (1993).
- [55] A. Billoire, T. Neuhaus, and B. A. Berg, Nucl. Phys. B **396**, 779 (1993).
- [56] B. Grossmann and M. L. Laursen, Int. J. Mod. Phys. C **3**, 1147 (1992); Nucl. Phys. B **408**, 637 (1993).
- [57] W. Janke and T. Sauer, Phys. Rev. E **49**, 3475 (1994).
- [58] H. Kleinert, *Path Integrals in Quantum Mechanics, Statistics, Polymer Physics, and Financial Markets*, 5th ed. (World Scientific, Singapore, 2009).
- [59] S. K. Kauffmann and S. M. Perez, J. Phys. A: Math. Gen. **17**, 2027 (1984).
- [60] D. W. Duke and J. D. Kimel, Phys. Rev. D **25**, 2960 (1982).
- [61] J. O. Akeyo and H. F. Jones, Phys. Rev. D **47**, 1668 (1993).

- [62] L. Canet, Phys. Rev. B **71**, 012418 (2005).
- [63] J. C. Wrigley, Phys. Rev. D **27**, 1965 (1983).
- [64] P. M. Stevenson, Phys. Rev. D **27**, 1968 (1983).
- [65] M. Inui, A. Niégawa, and H. Ozaki, Prog. Theor. Phys. **115**, 411 (2006).
- [66] I. R. C. Buckley, A. Duncan, and H. F. Jones, Phys. Rev. D **47**, 2554 (1993).
- [67] W. F. Lu, C. K. Kim, and K. Nahm, J. Phys. A: Math. Theor. **40**, 14457 (2007).
- [68] L. Canet, B. Delamotte, D. Mouhanna, and J. Vidal, Phys. Rev. D **67**, 065004 (2003).
- [69] J. Gross, T. Neuhaus, T. Vogel, and M. Bachmann, J. Chem. Phys. **138**, 074905 (2013).
- [70] M. Bachmann, J. Phys: Conf. Ser. **487**, 012013 (2014).
- [71] S. Schnabel, W. Janke, and M. Bachmann, J. Comput. Phys. **230**, 4454 (2011).
- [72] J. Gross, *Parallel Monte Carlo Simulations of Coarse-Grained Flexible Polymers To Obtain Structural Phase Diagrams*, Ph.D. thesis, The University of Georgia (2013).
- [73] R. H. Swendsen and J. S. Wang, Phys. Rev. Lett. **57**, 2607 (1986).
- [74] C. J. Geyer, *Markov Chain Monte Carlo Maximum Likelihood* in: *Computing Science and Statistics: Proceedings of the 23rd Symposium on the Interface*, edited by E. M. Keramidas (Interface Foundation, Fairfax Station VA, 1991), p. 156.
- [75] K. Hukushima, H. Takayama, and K. Nemoto, Int. J. Mod. Phys. C **7**, 337 (1996).
- [76] U. H. E. Hansmann, Chem. Phys. Lett. **281**, 140 (1997)
- [77] A. M. Ferrenberg and R. H. Swendsen, Phys. Rev. Lett. **63**, 1195 (1989).

- [78] S. Kumar, J. M. Rosenberg, D. Bouzida, R. H. Swendsen, and P. A. Kollman, *J. Comput. Chem.* **13**, 1011 (1992).
- [79] W. Janke, *Physica A* **254**, 164 (1998); B. A. Berg, *Fields Inst. Commun.* **26**, 1 (2000); *Comp. Phys. Commun.* **153**, 397 (2003).
- [80] B. A. Berg, *Markov Chain Monte Carlo Simulations* (World Scientific, Singapore, 2004).
- [81] T. Vogel, *Structural Behavior of Polymers from Monte Carlo Studies of Coarse-Grained Models*, Ph.D. thesis, Universität Leipzig (2009).
- [82] B. A. Berg and T. Çelik, *Phys. Rev. Lett.* **69**, 2292 (1992).
- [83] F. Wang and D. P. Landau, *Phys. Rev. Lett.* **86**, 2050 (2001); *Phys. Rev. E* **64**, 056101 (2001).
- [84] J. Zierenberg, M. Marenz, and W. Janke, *Comp. Phys. Commun.* **184**, 1155 (2013).
- [85] F. Seno, M. Vendruscolo, A. Maritan, and J. R. Banavar, *Phys. Rev. Lett.* **77**, 1901 (1996).
- [86] R. Ramakrishnan, B. Ramachandran, and J. F. Pekny, *J. Chem. Phys.* **106**, 2418 (1997).
- [87] A. Irbäck, C. Peterson, F. Potthast, and E. Sandelin, *Phys. Rev. E* **58**, R5249 (1998).
- [88] L. W. Lee and J. -S. Wang, *Phys. Rev. E* **64**, 056112 (2001).
- [89] N. Madras and A. D. Sokal, *J. Stat. Phys.* **50**, 109 (1988).
- [90] M. N. Rosenbluth and A. W. Rosenbluth, *J. Chem. Phys.* **23**, 356 (1955).
- [91] P. Grassberger, *Phys. Rev. E* **56**, 3682 (1997).

- [92] H. Frauenkron, U. Bastolla, E. Gerstner, P. Grassberger, and W. Nadler, *Phys. Rev. Lett.* **80**, 3149 (1998); U. Bastolla, H. Frauenkron, E. Gerstner, P. Grassberger, and W. Nadler, *Proteins* **32**, 52 (1998).
- [93] P. Grassberger and W. Nadler, in *Computational Statistical Physics – From Billiards to Monte Carlo*, ed. by K. H. Hoffmann and M. Schreiber (Springer, Berlin, 2002), p. 169, and references therein.
- [94] H. -P. Hsu, V. Mehra, W. Nadler, and P. Grassberger, *J. Chem. Phys.* **118**, 444 (2003).
- [95] M. Bachmann and W. Janke, *Phys. Rev. Lett.* **91**, 208105 (2003).
- [96] M. Bachmann and W. Janke, *J. Chem. Phys.* **120**, 6779 (2004).
- [97] P. Bézier, *Automatisme* **13**, 391 (1968).
- [98] W. J. Gordon and R. F. Riesenfeld, *J. Assoc. Comput. Machin.* **21**, 293 (1974).
- [99] U. H. E. Hansmann and Y. Okamoto, The Generalized-Ensemble Approach for Protein Folding Simulations, in: *Annual Reviews of Computational Physics VI*, ed. D. Stauffer, World Scientific, Singapore 1999, p. 129.
- [100] J. N. Onuchic, Z. Luthey-Schulten, and P. G. Wolynes, *Annu. Rev. Phys. Chem.* **48**, 545 (1997).
- [101] C. Clementi, A. Maritan, and J. R. Banavar, *Phys. Rev. Lett.* **81**, 3287 (1998).
- [102] J. N. Onuchic and P. G. Wolynes, *Curr. Opin. Struct. Biol.* **14**, 70 (2004).
- [103] R. Du, V. S. Pande, A. Yu. Grosberg, T. Tanaka, and E. S. Shakhnovich, *J. Chem. Phys.* **108**, 334 (1998).
- [104] V. S. Pande and D. S. Rokhsar, *Proc. Natl. Acad. Sci. U.S.A.* **96**, 1273 (1999).

- [105] U. H. E. Hansmann, M. Masuya, and Y. Okamoto, Proc. Natl. Acad. Sci. U.S.A. **94**, 10652 (1997); B. A. Berg, H. Noguchi, and Y. Okamoto, Phys. Rev. E **68**, 036126 (2003).
- [106] K. L. Osborne, M. Bachmann, and B. Strodel, Proteins **81**, 1141 (2013).
- [107] M. Bachmann and W. Janke, Phys. Rev. E **73**, 020901(R) (2006).
- [108] M. Bachmann and W. Janke, Phys. Rev. E **73**, 041802 (2006).
- [109] Y. Singh, D. Giri, and S. Kumar, J. Phys. A **34**, L67 (2001).
- [110] R. Rajesh, D. Dhar, D. Giri, S. Kumar, and Y. Singh, Phys. Rev. E **65**, 056124 (2002).
- [111] M. Bachmann and W. Janke, Phys. Rev. Lett. **95**, 058102 (2005).
- [112] J. Krawczyk, A. L. Owczarek, T. Prellberg, and A. Reznitzer, Europhys. Lett. **70**, 726 (2005).
- [113] J. Luettmer-Strathmann, F. Rampf, W. Paul, and K. Binder, J. Chem. Phys. **128**, 064903 (2008).
- [114] A. D. Swetnam and M. P. Allen, Phys. Chem. Chem. Phys. **11**, 2046 (2009).
- [115] Y. W. Li, T. Wüst, and D. P. Landau, Phys. Rev. E **87**, 012706 (2013).
- [116] B. Pattanasiri, Y. W. Li, D. P. Landau, and T. Wüst, J. Mod. Phys. C **23**, 1240008 (2012).
- [117] M. Möddel, M. Bachmann, and W. Janke, J. Phys. Chem. B **113**, 3314 (2009).
- [118] L. Wang, T. Chen, X. Lin, Y. Liu, and H. Liang, J. Chem. Phys. **131**, 244902 (2009).
- [119] M. Möddel, W. Janke, and M. Bachmann, Macromolecules, **44**, 9013 (2011).

- [120] I. Gurevitch and S. Srebnik, Chem. Phys. Lett. **444**, 96 (2007); J. Chem. Phys. **128**, 144901 (2008).
- [121] J. Gross, T. Vogel, and M. Bachmann, Phys. Chem. Chem. Phys. **17**, 30702 (2015).
- [122] S. Karalus, W. Janke, and M. Bachmann, Phys. Rev. E **84**, 031803 (2011).
- [123] T. Vogel and M. Bachmann, Phys. Rev. Lett. **104**, 198302 (2010).
- [124] T. Vogel, T. Mutat, J. Adler, and M. Bachmann, Commun. Comput. Phys. **13**, 1245 (2013).
- [125] T. Vogel, J. Gross, and M. Bachmann, J. Chem. Phys. **142**, 104901 (2015).
- [126] H. Arkin and W. Janke, Phys. Rev. E **85**, 051802 (2012); J. Phys. Chem. B **116**, 10379 (2012); J. Chem. Phys. **138**, 054904 (2013); Eur. Phys. J. Spec. Top. **216**, 181 (2013).
- [127] J. J. Cerdá and T. Sintes, Biophys. Chem. **115**, 277 (2005).
- [128] K. Sumithra and E. Straube, J. Chem. Phys. **125**, 154701 (2006).
- [129] A. D. Swetnam and M. P. Allen, Phys. Rev. E **85**, 062901 (2012).
- [130] M. Möddel, W. Janke, and M. Bachmann, Phys. Rev. Lett. **112**, 148303 (2014).
- [131] P. H. Verdier and W. H. Stockmayer, J. Chem. Phys. **36**, 227 (1962).
- [132] P. H. Verdier, J. Chem. Phys. **45**, 2122 (1966).
- [133] D. E. Kranbuehl and P. H. Verdier, J. Chem. Phys. **56**, 3145 (1972).
- [134] P. H. Verdier, J. Chem. Phys. **59**, 6119 (1973).
- [135] D. E. Kranbuehl, P. H. Verdier, and J. M. Spencer, J. Chem. Phys. **59**, 3861 (1973).
- [136] D. E. Kranbuehl and P. H. Verdier, J. Chem. Phys. **67**, 361 (1977).

- [137] J. A. McCormick, C. K. Hall, and S. A. Khan, *J. Chem. Phys.* **122**, 114902 (2005).
- [138] E. M. Pestryaev, *J. Phys.: Conf. Ser.* **324**, 012031 (2011).
- [139] T. Aoyagi, J. Takimoto, and M. Doi, *J. Chem. Phys.* **115**, 552 (2001).
- [140] A. Malevanets and J. M. Yeomans, *Europhys. Lett.* **52**, 231 (2000).
- [141] J. M. Polson and J. P. Gallant, *J. Chem. Phys.* **124**, 184905 (2006).
- [142] M. Bishop, M. H. Kalos, and H. L. Frisch, *J. Chem. Phys.* **70**, 1299 (1979).
- [143] D. C. Rapaport, *J. Chem. Phys.* **71**, 3299 (1979).
- [144] W. Bruns and R. Bansal, *J. Chem. Phys.* **74**, 2064 (1981).
- [145] W. Bruns and R. Bansal, *J. Chem. Phys.* **75**, 5149 (1981).
- [146] K. Mussawisade, M. Ripoll, R. G. Winkler, and G. Gompper, *J. Chem. Phys.* **123**, 144905 (2005).
- [147] P. P. Nidras and R. Brak, *J. Phys. A: Math. Gen.* **30**, 1457 (1997).
- [148] R. B. Bird, C. F. Curtiss, R. C. Armstrong, and O. Hassager, *Dynamics of Polymeric Liquids*, 2nd ed. (Wiley, New York, 1987).
- [149] K. Kremer and G. S. Grest, *J. Chem. Phys.* **92**, 5057 (1990).
- [150] A. Milchev, A. Bhattacharya, and K. Binder, *Macromolecules* **34**, 1881 (2001).
- [151] T. Vogel, M. Bachmann, and W. Janke, *Phys. Rev. E* **76**, 061803 (2007).
- [152] D. T. Seaton, T. Wüst, and D. P. Landau, *Phys. Rev. E* **81**, 011802 (2010).
- [153] H. Behringer and M. Pleimling, *Phys. Rev. E* **74**, 011108 (2006).

- [154] A related flat-histogram chain-growth method was introduced in T. Prellberg and J. Krawczyk, Phys. Rev. Lett. **92**, 120602 (2004).
- [155] M. Bachmann and W. Janke, Lect. Notes Phys. **736**, 203 (2008).
- [156] D. T. Seaton, S. Schnabel, D. P. Landau, and M. Bachmann, Phys. Rev. Lett. **110**, 028103 (2013).
- [157] O. Kratky and G. Porod, J. Colloid Sci. **4**, 35 (1949).
- [158] T. Koci and M. Bachmann, Phys. Rev. E **92**, 042142 (2015).
- [159] M. J. Williams and M. Bachmann, Phys. Rev. Lett. **115**, 048301 (2015).
- [160] J. P. Neirotti, F. Calvo, D. L. Freeman, and J. D. Doll, J. Chem. Phys. **112**, 10340 (2000).